MOLECULAR ORGANIZATION OF ACTIVE RAFTS AND PHASE SEGREGATION

BY

ANIRBAN POLLEY

A THESIS SUBMITTED TO THE JAWAHARLAL NEHRU UNIVERSITY
FOR THE DEGREE OF DOCTOR OF PHILOSOPHY

DEPARTMENT OF THEORETICAL PHYSICS
RAMAN RESEARCH INSTITUTE
BANGALORE 560 080

SEPTEMBER 2013

Typeset in LaTeX 2_ε.

Certificate:

This is to certify that the thesis entitled **"Molecular organization of Active Rafts and phase segregation"** submitted by Anirban Polley for the award of the degree of Doctor of Philosophy of Jawaharlal Nehru University is his original work. This has not been published or submitted to any other University for any other Degree or Diploma.

Prof. Ravi Subrahmanyan
(Director)
Raman Research Institute
Bangalore 560 080
India

Prof. Madan Rao
(Thesis Supervisor)

Declaration:

I hereby declare that the work reported in this thesis is entirely original. This thesis is composed independently by me at Raman Research Institute under the supervision of Prof. Madan Rao. I further declare that the subject matter presented in this thesis has not previously formed the basis for the award of any degree, diploma, membership, associateship, fellowship or any other similar title of any university or institution.

Prof. Madan Rao

Anirban Polley

Theoretical Physics
Raman Research Institute
Bangalore 560 080
India

Dedicated to

My Parents, Anil Kumar Polley and Hira Polley

for their love, blessing and sacrifices

My brother and sister-in-law, Dr. Arup Polley and Rita Bhui

for their support and inspiration

Beloved nephew, Amiyo

&

My uncle, Prof. Pranesh Chowdhury

for his advice

Acknowledgements

I am grateful to my supervisor Prof. Madan Rao for his guidance, encouragement and support through out the period. I am fortunate to have a teacher like him.

I express my gratitute to Prof. Satyajit Mayor for introducing me to the kingdom of cell. I would like to thank Prof. V. A. Raghunathan for clarifying the mystery of lipid chemistry. I express my heartfelt gratitude to Prof. Joseph Samuel and Prof. Supurna Sinha for the insightful discussions. My sincere thanks to Prof. Satyavani Vemparala for teaching me molecular dynamics. I would like to acknowledge Prof. Yashodan Hatwalne, Prof. Abhishek Dhar and Prof. Sanjeeb Sabhapandit for immensely helpful discussions. I would like to thank Prof Pramod Pullarkat for giving critical inputs at different stages of my work.

A very special thanks to Prof. Mikko Karttunen and Prof. S. J. Marrink for the crutial comments and suggestions at every stage of my work.

My special thanks to Prof. Sriram Ramaswamy, Prof. Chandan Dasgupta and Prof. Vijay Shenoy for providing wonderful courses in IISc. I would like to extend my sincerest thanks to Prof. P. B. Sunil Kumar who has introduced me to the current field of research.

My special thanks to Ambika, Riya and Suvrajit for wonderful discussions and clarifying doubts about the experiments on cell. I can not forget to acknowledge Samuli Ollila and Anand Srivastava for the insightful discussions. When

I have joined the group, I have interacted with the wonderful lab mates: Abhishek, Kripa, Gayathri and Bhaswati. I would like to acknowledge to Abhishek for several discussions on variety of topics. I am deeply indebted to Pragya, Nitin, Amit, Kabir, Srikrishna, Debshankar, Raj and Debarshini for making the lab-environment soothing and enjoyable.

My heartiest thanks to Tridib and Arijit who make my time in RRI enjoyable. My special thanks to Rajib and Debashis for introducing the art of cooking. I was lucky to have Nandan, Wasim, Arif, Antara, Dipanjan, Brindaban, Alok, Sajal, Abhijit, Radhakrishnan A.V., Joya Kumar and Bibhu as my seniors. I also thank Anjan, Arnab, Prasad, Samim, Rahul, Safi, Jyothi, Deepak, Anupam, Madhukar, Chaitra, Amrita, Anagha, Renu, Chandreyee and Nipanjana.

I would like to thank Krishnamurthy S., Sridhar B. and Jacob Rajan for sorting out any computer issues. I also like to thank Y. M. Patil, Meera B. M. and all the staff members of the library for their assistance. I thank Krishnamaraju, Subramanya P. V., Latha, Harini, Majunatha, Radha and Marisa for making official matters very easy. A very special note of thanks to Shiva and Manju, our colleagues at the LAMP group for extending overwhelming support at any issue.

I am grateful to RRI and RMV Hostel environment, specially Bangalore weather for making my stay enjoyable. I have enjoyed most in playing football at the RRI lawn with my friends. It was a refreshing change from the work.

I am deeply indebted to my brother, Arup Polley for constant support, encouragement and thoughtful ideas at any point of time. A special thanks to my sister-in-law, Rita for her encouragement. A very special note to my uncle, Pranesh Chowdhury for his encouragement and advices.

Last, but not the least, my deepest gratitude and sincerest regards to my parents, Anil Kumar Polley and Hira Polley for their constant support and encouragement throughout this period. Without their support and encouragement, this work would not have been possible.

Synopsis

The cell membrane consists of many different kinds of lipids and proteins and exhibits both lateral heterogeneity (called 'rafts') and transverse bilayer asymmetry. An important quest in the field of cell membrane biophysics is to understand the physical and chemical basis of lipid/protein organization and segregation at different scales. Early studies have shown that a variety of outer leaflet lipid-tethered proteins (such as GPI-anchored proteins, GPI-APs) at the cell surface are organized as monomers and cholesterol/sphingolipid sensitive nanoclusters, which are driven by the active nonequilibrium dynamics of the underlying actin and myosin at the cortex of the cell. In this thesis, we investigate the physical and chemical nature of the coupling between the outer leaflet lipid-tethered proteins and inner leaflet molecules (such as PS lipids) which interact with cortical actin. We address these issues using atomistic MD simulations of multicomponent, asymmetric bilayer membranes.

First, we investigate using atomistic molecular dynamics simulations, the physical properties of a 3-component asymmetric lipid bilayer system comprising of an unsaturated POPC, a saturated PSM and Chol. Our simulations explore both the dynamics of coarsening following a quench from the mixed phase, and the final phase segregated regime obtained by equilibrating a fully segregated configuration. Following a quench, the membrane quickly enters

a coarsening regime, where we observe the initial stages of liquid ordered, l_o, domain formation. These growing domains are found to be highly enriched in cholesterol and PSM. Consistent with this, the final phase-segregated regime contains large l_o domains at equilibrium, enriched in cholesterol and PSM. Our simulations suggest that the cholesterol molecules partition into these PSM-dominated regions in the ratio of $3:1$ when compared to POPC-dominated regions. PSM molecules exhibit a measurable tilt and long range tilt correlations within the l_o domain as a consequence of the asymmetry of the bilayer, with implications to local membrane deformation and budding. We compute the tagged particle diffusion for PSM and cholesterol molecules, which reflects spatial variations in the physical environment encountered by the tagged particle and compare this with recent experimental results obtained from high resolution microscopy.

A question of considerable interest to cell membrane biology is whether phase segregated domains across an asymmetric bilayer are strongly correlated with each other and whether phase segregation in one leaflet can induce phase segregation in the other. Here, we answer both these questions in the affirmative, using an atomistic molecular dynamics simulation to study the equilibrium statistical properties of a 3-component *asymmetric* lipid bilayer comprising of an unsaturated POPC, a saturated SM and Chol with different composition ratios. Our simulations are done by fixing the composition of the upper leaflet to be at the coexistence of the liquid ordered (l_o) - liquid disordered (l_d) phases, while the composition of the lower leaflet is varied from the phase coexistence regime to the mixed l_d phase, across a first-order phase boundary.In the regime of phase coexistence in each leaflet, we find strong transbilayer correlations of the l_o domains across the two leaflets, resulting in *bilayer registry*. This transbilayer correlation depends sensitively upon the chain length of the participating lipids and possibly on other features of lipid chemistry, such as degree of saturation. We find that the l_o domains in the

upper leaflet can induce phase segregation in the lower leaflet, even when the latter is nominally in the mixed (l_d) phase.

Finally, we investigate the physical and chemical nature of the coupling between the outer leaflet lipid-tethered proteins (GPI-APs) and inner leaflet molecules (such as PS lipids) which interact with cortical actin and myosin at the cell cortex. We address these issues using atomistic MD simulations of multicomponent, asymmetric bilayer membranes with these inserted proteins. We make a detailed study of the physical properties and phase behavior of such multicomponent, asymmetric membranes, and the transbilayer coupling between the outer leaflet lipid-tethered proteins (GPI-APs) and inner leaflet PS lipids as a function of relative concentration of the components and lipid chemistry. We find that the strength of the transbilayer coupling between the outer leaflet lipid-tethered proteins and inner leaflet PS lipids is enhanced by *crosslinking PS* in presence of significant amount of cholesterol. This induces local l_o regions in the background of l_d phase which registers the outer leaflet GPI-APs. Together with the earlier studies from our group these results make a case for the existence of 'active rafts' on the surface of living cells.

Prof. Madan Rao

Anirban Polley

Theoretical Physics
Raman Research Institute
Bangalore 560 080
India

Publications

1. Atomistic Simulations of a Multicomponent Asymmetric Lipid Bilayer.
   Anirban Polley, Satyavani Vemparala and Madan Rao. *JPCB* 2012. 116, 13403-13410.

2. Bilayer registry in a multicomponent asymmetric bilayer.
   Anirban Polley, Satyajit Mayor and Madan Rao. *arXiv*: 1309.4853

3. Transbilayer coupling of outer leaflet GPI-APs and inner leaflet lipids across the bilayer membeane.
   (In progress)

4. Active diffusion of lipid-tethered proteins driven by cortical actin.
   Suvrajit Saha, Il-Hyung Lee, **Anirban Polley**, J. T. Groves, Satyajit Mayor and Madan Rao. (In progress)

5. cell plasma membranes do not exhibit a miscibility phase transition over a wide range of temperatures.
   Il-Hyung Lee, Suvrajit Saha, **Anirban Polley**, Hector Huang, Satyajit Mayor, Madan Rao and Jay T. Groves. (In progress)

6. Partitioning of ethanol in multi-component membranes: effects on membrane structure.

Anirban Polley and Satyavani Vemparala. *Chem. and Phys. of Lipids*. 2013. 166, 1-11.

7. Bending elasticity of macromolecules: analytic predictions from the worm-like chain model.
   Anirban Polley, Joseph Samuel and Supurna Sinha. *Phys. Rev. E*. 2013. 87, 012601.

Contents

1

Introduction

1.1. Introduction

The cell is the structural and functional unit of all living organisms. The Eukaryotic cell has evolved to have different membrane bound compartments with specialized functions (Figure 1.1). For example, the endoplasmic reticulum (ER) and Golgi bodies are mainly involved with the synthesis and sorting of proteins whereas, the mitochondria are cellular power plants which supply chemical energy in the form of Adenosine Triphosphate (ATP). Such membrane bound compartments are a convenient and efficient way of sorting and segregating biochemicals within the cell.

The plasma membrane separates the internal material of the cell from its external environment. It is a highly selective semipermeable membrane which enables the cell to perform different functions such as sorting, signaling and endocytosis. It consists of few hundred different types of lipids which are classified according to the structure of the head group and backbone such

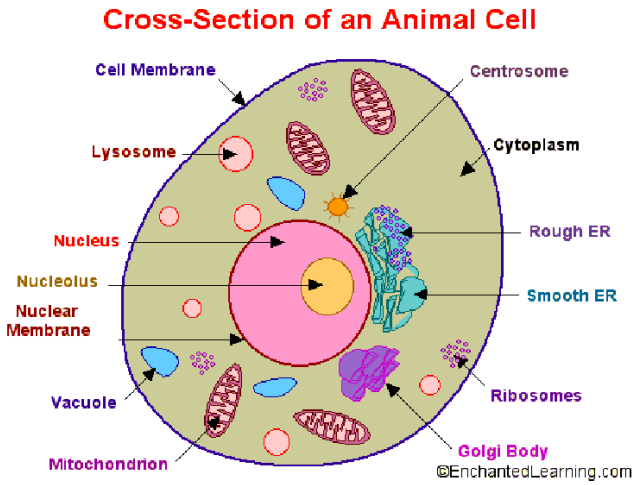

FIGURE 1.1: shows the schematic diagram of a eukaryotic cell, having cytosol with important organelles such as nucleus, endoplasmic reticulum (ER), mitochondria, golgi bodies. The cell is encased in a plasma membrane. (Courtesy [1])

as ceramides, glycerolipids, glycerophospholipids, sphingomyelin, glycosphingomyelins and cholesterol and more than a hundred types of proteins.

The plasma membrane is inherently asymmetric transversely and heterogeneous in its composition as well as number laterally. Transverse composition heterogeneity has many important consequences as seen in apoptosis where the inner-leaflet lipid phosphatidylserine (PS) gets accumulated at the outer leaflet, serving as a signal to cell death [2, 3]. There is a complex regulatory mechanism in place which maintains this heterogeneities at the cell surface.

1.2. Models of the cell membrane

1.2.1. Fluid mosaic model

The first model to describe the organization of lipid and proteins on the plasma membrane was the 'Fluid-Mosaic' model [4] (Figure 1.2). It was observed in

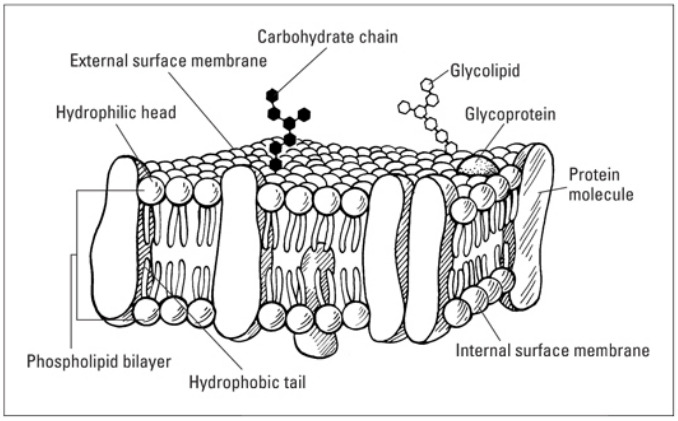

FIGURE 1.2: shows the schematic diagram of the Fluid Mosaic Model of the plasma membrane (Courtesy [5]). Here, proteins are embedded in a equilibrium multicomponent lipid bilayer.

experiments done in fusing cell membranes that translational diffusion coefficient of the lipids and proteins could vary on the basis of lipid mixture. It was found that the mobility of the lipids and proteins of the cell membrane was consistent with simple brownian diffusion. However, the translational diffusion coefficients were found to be different from those of lipids/proteins, measured in artificial fluid membranes approximately by an order of magnitude [6]. This implies that the lipid environment is same as in artificial fluid membranes, but the molecules in fluid membrane having lipids/proteins experience extra drag due to the interaction between the lipid and proteins. Moreover, the cytoskeleton beneath the plasma membrane (cortical actin) could also influence the transbilayer proteins.

According to the Fluid Mosaic model, multicomponent lipid membrane helps to vary the solvation rate of the membrane proteins via specific interactions (e.g. hydrogen bonding, hydrophobic shielding, electrostatic and van der Waals interaction). The Fluid Mosaic model is an equilibrium model of the plasma membrane where the functional proteins are embedded in a 2-dimensional homogeneous, multicomponent lipid bilayer.

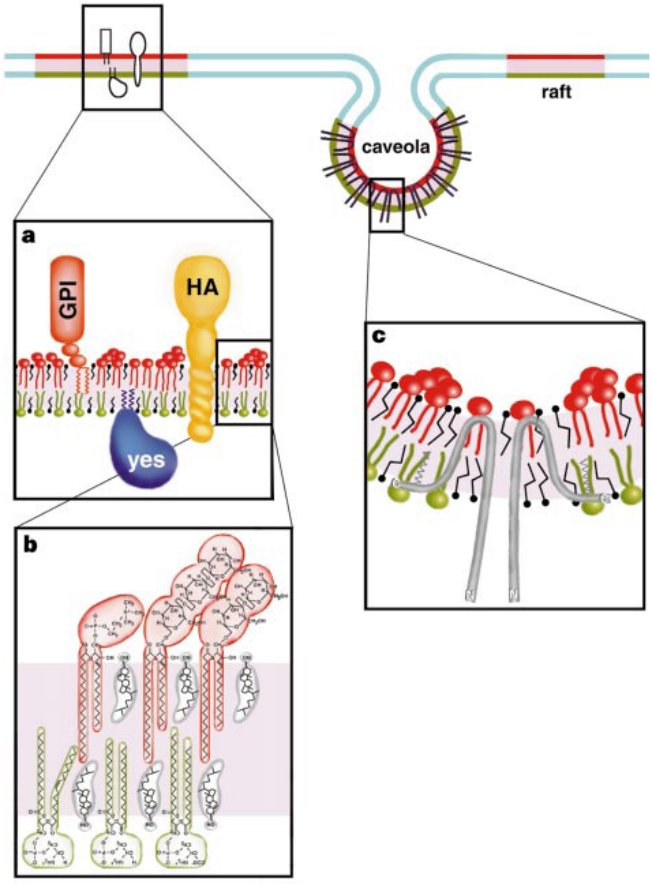

FIGURE 1.3: shows the schematic diagram of raft model, lateral heterogeneities of the specific lipids (e.g., cholestrol and sphingolipid) / proteins (segregated GPI-anchored proteins) (Courtesy [7])

1.2.2. Raft model

A recent proposal suggests that there exist lipid-based heterogeneities in the plasma membrane at different length and time scales with a functional significance [7–10] (Figure 1.3). Membrane rafts, invoked to explain certain features of signaling and sorting in living cells, are believed to be lateral heterogeneities of lipids, such as cholesterol and sphingolipids, and proteins, such as GPI-anchored proteins (GPI-APs), that are enriched in liquid-ordered (l_o) domains of the plasma membrane (PM)[11–13] (Figure 1.4, 1.5). However, the size, dynamics and composition of these membrane rafts have been the subject of

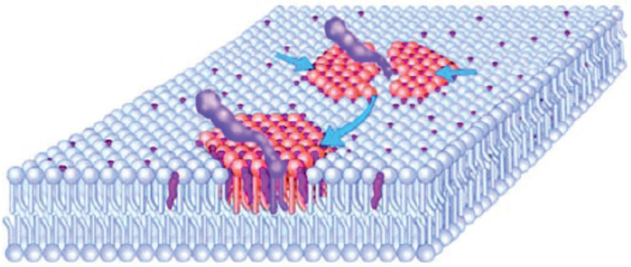

FIGURE 1.4: shows the schematic diagram of 'membrane raft' (Courtesy [11]) defined as small, dynamic lipid shells associated with proteins.

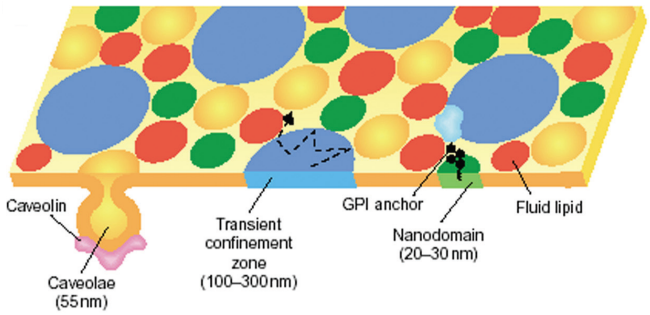

FIGURE 1.5: shows the schematic diagram of 'membrane raft' (Courtesy [12]) defined as 'mosaic of domains' which are regulated via cholesterol-based mechanism.

much debate.

On the basis of lateral functional organization, a specific set of membrane components are found to be insoluble in a solvent containing nonionic detergents (e.g., Triton X-100) at low temperatures (4°C), giving *detergent-resistant membrane (DRM)* [14]. DRM composed of a high proportion of cholesterol, sphingolipids, phosphatidylcholines (PCs) and GPI-anchored proteins have become the definition of membrane rafts [15–18]. Moreover, many specific membrane components are found to be aggregated in a cholesterol sensitive fashion. However, DRM association does not constitute the unambiguous evidence of preexisting lipid-dependent assemblies in the living cell membranes

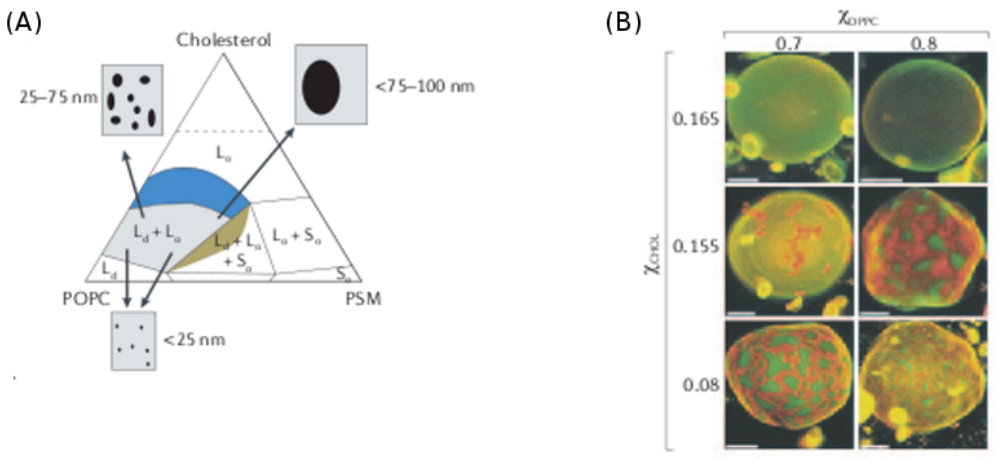

FIGURE 1.6: (A) shows the ternary phase diagram of POPC, palmitoyl sphingomyelin (PSM) and Chol at $23°C$ and (B) shows the macroscopic domains formed in giant unilamellar vesicles (GUVs) composed of cholesterol, 1,2-dipalmitoylphosphatidylcholine (DPPC) and 1,2-dioleoylphosphatidylcholine (DOPC). Here, l_o domains and l_d domains are visualized by orange and green respectively.[19]

[9]. Also, this model can not provide information about the physical organization of the constituents (lipids and proteins).

An artificial multicomponent membrane (for example, artificial membrane composed of palmitoyl oleoyl phosphatidylcholine (POPC) : sphingolipids (SM) : cholesterol (Chol)=1:1:1) has been taken as a model system which can describe the physical properties of rafts on plasma membrane. Giant unilamellar vesicles (GUVs) composed of POPC, SM and Chol, form l_o domains in an liquid disorder (l_d) background in which GPI-APs appear to be uniformly enriched in these l_o domains [19] (Figure 1.6). Here, rafts are found to be spontaneously formed via *equilibrium phase segregation* in multicomponent system.

However, experiments on live cells, using Fluorescence Resonance Energy Transfer (FRET) and detailed theoretical analysis [20–22], show that GPI-APs are organized as monomers and cholesterol-sensitive nanoclusters and the dynamics of nanocluters are regulated by the *active dynamics* of cortical actin (CA) and myosin.

Therefore, *Membrane raft model*, conceptualized earlier as a passive equilibrium phase segregation of multicomponent lipid membrane fails to explain the above assemblies of the specific lipids regulated by *active dynamics* of CA and myosin suggesting a need to improve the model by incorporating *active* properties to the raft model.

1.2.3. Active composite model: active rafts

Membrane rafts, a lipid based compositional heterogeneities of cholesterol, sphingomyelin and GPI-APs, have been invoked to facilitate certain feature of signaling and sorting in living cells. It has been postulated to have a thermodynamic origin in which the spatial heterogeneities of the compositions are the result of being near or at phase coexistence [7].

But the studies on the spatial distribution and steady state dynamics of fluorescently tagged GPI-AP nanoclusters using high-spatial and temporal resolution FRET microscopy reveal :

(i) Nonrandom spatial distribution of nanoclusters [23, 24] (shown in Figure 1.7);

(ii) Over a range of temperature, the dynamics of interconversion between the nanocluters and the monomers is spatially heterogeneous and *non-Arrhenius*; a sharp crossover with a reduction in the *activity of CA*[21];

(iii) The ratio of the nanoclusters of GPI-APs to the monomers is independent of its concentration. This is an important evidence for the violation of mass action relationship [20];

(iv) Direct perturbations of CA activity or indirect perturbation of the same by cholesterol depletion, affect the construction, dynamics and spatial organization of GPI-AP nanoclusters. [20];

(v) For a system of size L with N number of molecules, the number fluctuation, $\Delta N(\equiv \sqrt{\delta N^2}) \propto \sqrt{\overline{N}}$. However, in experiments on GPI-APs in the cell surface

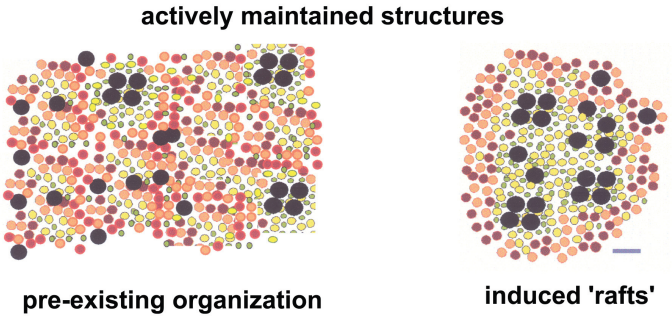

FIGURE 1.7: shows the schematic diagram of raft.[24]. Here, GPI-APs studies in living cell show preexisting small and dynamic lipid assemblies which are actively driven to form large scale 'raft'.

which are regulated by actin, $\Delta N \propto N^{4/5} \gg N^{1/2}$ with a crossover to $\sqrt{N}$ at small N indicating that the cell surface molecules, GPI-APs, are subject to both active and thermal noise [21].

(vi) Moreover, nanoclusters fragment into monomers when the cell membrane has detached from the CA, as seen in spontaneously formed blebs and are reformed when the blebs retract due to the repolymerization of actin [20].

Furthermore, electron microscopy (EM) studies of the steady state distributions of the Ras-signaling proteins [25, 26] and glycolipids [27] have also suggested the CA dependent, nonrandom mixtures of nanoclusters and the monomers.

These evidences suggest that the nanocluster distribution of GPI-APs on the living cell surface is maintained away from thermal and chemical equilibrium and is controlled by the *active* remodeling of the underlying CA and myosin (shown in Figure1.8).

1.3. Thesis outline

Since GPI-APs are lipid tethered proteins which reside on the outer leaflet of the PM, it is natural to ask what are the molecular linkages and interactions

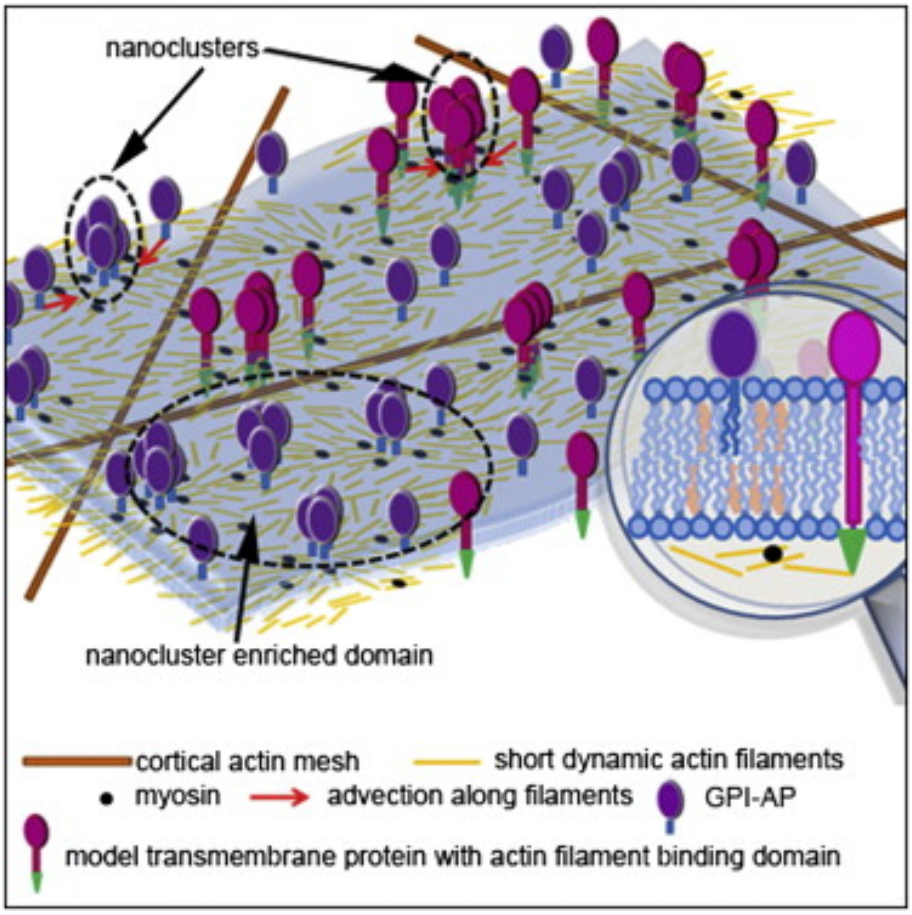

FIGURE 1.8: shows the schematic diagram of the nanoscale organization of GPI-APs which are regulated by the active dynamics of acto-myosin of the CA. (Courtesy [21])

between GPI-APs and CA. We have addressed this question using an atomistic molecular dynamics simulation of an asymmetric bilayer membrane comprising of POPC, PSM and Chol, to which we have added GPI-APs on the upper leaflet and phosphatidylserine (PS) lipids on the inner leaflet. Earlier studies [28] have shown that PS binds with CA via binding proteins such as spectrin [29], talin [30], caldesmon [31] and its organization can be changed by the perturbation of CA [32]. Therefore, PS might be the possible candidate in the lower leaflet of the bilayer membrane for this linkage.

This thesis is organized as follows.

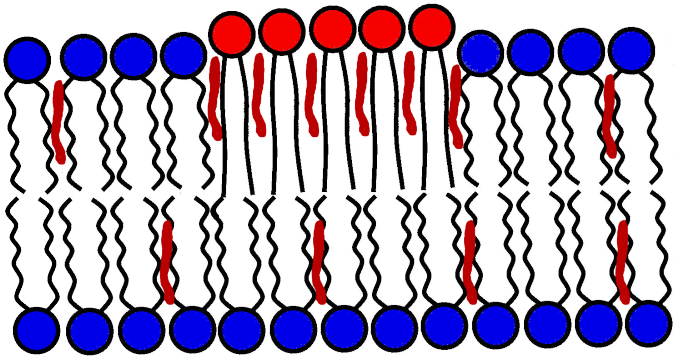

FIGURE 1.9: shows the schematic diagram of the asymmetric multicomponent bilayer. Here, Red-head, blue-head lipids denote as PSM and POPC respectively whereas, brown colored lipid denotes cholesterol.

Chapter 2 deals with the numerical techniques where the details of the atomistic molecular dynamics (MD) simulations of the multicomponent bilayer membrane are given. In this Chapter, we describe the protocols that we have followed to perform the MD studies to tackle the problem.

In the Chapter 3, using atomistic molecular dynamics simulations, the physical properties of a 3-component asymmetric mixed lipid bilayer system comprising of an unsaturated POPC, a saturated PSM and Chol are investigated (as shown in Figure 1.9). Our simulations explore both the dynamics of coarsening following a quench from the mixed phase, and the final phase segregated regime obtained by equilibrating a fully segregated configuration. Following a quench, the membrane quickly enters a coarsening regime, where the initial stages of liquid ordered, l_o, domain formation are observed. These growing domains are found to be highly enriched in cholesterol and PSM. Consistent with this, the final phase-segregated regime contains large l_o domains at equilibrium, enriched in cholesterol and PSM. Our simulations suggest that the cholesterol molecules may partition into these PSM-dominated regions in the ratio of $3:1$ when compared to POPC-dominated regions. PSM molecules exhibit a measurable tilt and long range tilt correlations within the l_o domain

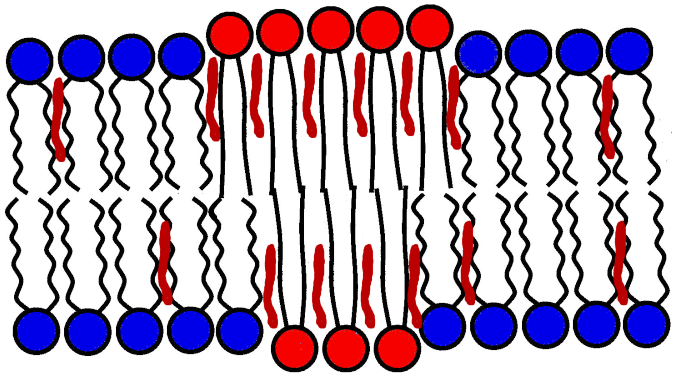

FIGURE 1.10: shows the schematic diagram of the asymmetric multicomponent bilayer. Here, Red-head, blue-head lipids denote as PSM and POPC respectively whereas, brown colored lipid denotes cholesterol.

as a consequence of the asymmetry of the bilayer, with implications to local membrane deformation and budding. Tagged particle diffusion for PSM and cholesterol molecules, which reflects spatial variations in the physical environment encountered by the tagged particle, is computed and compared with recent experimental results obtained from high resolution microscopy.

A question of considerable interest to cell membrane biology is whether phase segregated domains across an asymmetric bilayer are strongly correlated with each other and whether phase segregation in one leaflet can induce phase segregation in the other. In Chapter 4, we answer both these questions in the affirmative, using an atomistic molecular dynamics simulation to study the equilibrium statistical properties of a 3-component *asymmetric* lipid bilayer comprising of an unsaturated POPC, a saturated SM and Chol with different composition ratios. Our simulations are done by fixing the composition of the upper leaflet to be at the coexistence of the liquid ordered (l_o) - liquid disordered (l_d) phases, while the composition of the lower leaflet is varied from the phase coexistence regime to the mixed l_d phase, across a first-order phase boundary as shown in Figure 1.10. In the regime of phase coexistence in each leaflet, we find strong transbilayer correlations of the l_o domains across the two

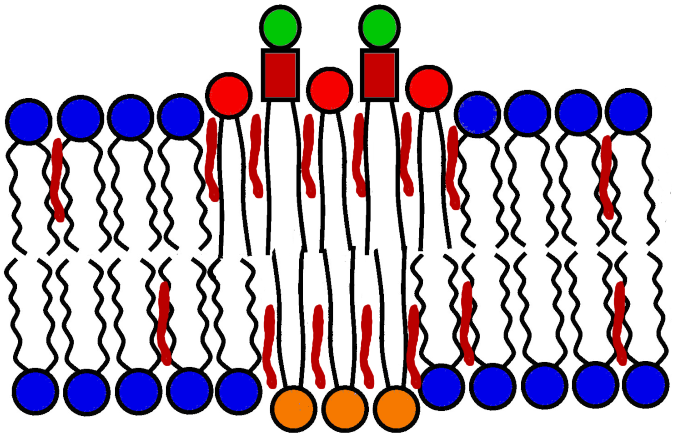

FIGURE 1.11: shows the schematic diagram of the asymmetric multicomponent bilayer. Here, Red-head, blue-head lipids denote as PSM and POPC respectively whereas, brown colored lipid denotes cholesterol. Green-Brown-head lipid and orange-head lipid are GPI-AP and PS lipids respectively.

leaflets, resulting in *bilayer registry*. This transbilayer correlation depends sensitively upon the chain length of the participating lipids and possibly on other features of lipid chemistry, such as degree of saturation. We find that the l_o domains in the upper leaflet can induce phase segregation in the lower leaflet, even when the latter is nominally in the mixed (l_d) phase.

Finally, in Chapter 5, we investigate the physical and chemical nature of the coupling between the outer leaflet lipid-tethered proteins (GPI-APs) and inner leaflet molecules (such as PS lipids) which interact with CA. We address these issues using atomistic MD simulations of multicomponent, asymmetric bilayer membranes. We make a detailed study of the physical properties and phase behavior of such multicomponent, asymmetric membranes, and the transbilayer coupling between the outer leaflet lipid-tethered proteins (GPI-APs) and inner leaflet PS lipids as a function of relative concentration of the components and lipid chemistry (as shown in Figure 1.11). We find that the strength of the transbilayer coupling between the outer leaflet lipid-tethered proteins and inner leaflet PS lipids is enhanced by *crosslinking PS* in presence of significant amount of cholesterol. This induces local l_o regions in the background of

l_d phase which registers the outer leaflet GPI-APs. Together with the earlier studies from our group these results make a case for the existence of 'active rafts' on the surface of living cells.

References

[1] Animal cell. http://www.enchantedlearning.com/subjects/animals/cell/.

[2] RA Schlegel and P Williamson. Phosphatidylserine, a death knell. *Cell Death Differ.*, 8(6):551–63, 2001.

[3] P Williamson and RA Schlegel. Transbilayer phospholipid movement and the clearance of apoptotic cells. *Biochim Biophys Acta.*, 1585(2-3):53–10, 2002.

[4] S.J Singer and Garth L. Nicolson. The fluid mosaic model of the structure of cell membranes. *Science*, 175:175:720–11, 1972.

[5] Fluid mosaic model. http://biology-10.wikispaces.com/file/view/

[6] LD Frye and M Edidin. The rapid intermixing of cell surface antigens after formation of mouse-human heterokaryons. *J Cell Sci.*, 7:319–35, 1970.

[7] K Simons and E Ikonen. Functional rafts in cell membranes. *Nature*, 387:569–72, 1997.

[8] M Bagnat, S Keränen, A Shevchenko, A Shevchenko, and K. Simons. Lipid rafts function in biosynthetic delivery of proteins to the cell surface in yeast. *Proc Natl Acad Sci U S A.*, 97:3254–9, 2000.

[9] S Mayor and M Rao. Rafts: scale-dependent, active lipid organization at the cell surface. *Traffic*, 5(4):231–40, 2004.

[10] M Muñiz, P Morsomme, and H. Riezman. Protein sorting upon exit from the endoplasmic reticulum. *Cell.*, 104:313–20, 2001.

[11] R G Anderson and K Jacobson. A role for lipid shells in targeting proteins to caveolae, rafts, and other lipid domains. *Science*, 296:1821–5, 2002.

[12] FR Maxfield. Plasma membrane microdomains. *Curr Opin Cell Biol.*, 483–7:2002, 14.

[13] K Simons and D Toomre. Lipid rafts and signal transduction. *Nat Rev Mol Cell Biol*, 1:31–9, 2000.

[14] DA Brown and JK Rose. Sorting of gpi-anchored proteins to glycolipid-enriched membrane subdomains during transport to the apical cell surface. *Cell*, 68:533–44, 1992.

[15] V Horejsí, K Drbal, M Cebecauer, J Cerný, T Brdicka, P Angelisová, and H. Stockinger. Gpi-microdomains: a role in signalling via immunoreceptors. *Immunol Today.*, 20:356–61., 1999.

[16] TJ Proszynski, R Klemm, M Bagnat, K Gaus, and K Simons. Plasma membrane polarization during mating in yeast cells. *J Cell Biol.*, 173:861–6, 2006.

[17] I Stefanová, V Horejsí, IJ Ansotegui, W Knapp, and H. Stockinger. Gpi-anchored cell-surface molecules complexed to protein tyrosine kinases. *Science*, 254:1016–9, 1991.

[18] TM Stulnig, M Berger, T Sigmund, H Stockinger, V Horejsí, and W. Waldhäusl. Signal transduction via glycosyl phosphatidylinositol-anchored proteins in t cells is inhibited by lowering cellular cholesterol. *J Biol Chem.*, 272:19242–7, 1997.

[19] JF Hancock. Lipid rafts: contentious only from simplistic standpoints. *Nat Rev Mol Cell Biol.*, 7:456–62, 2006.

[20] Debanjan Goswami, Kripa Gowrishankar, Sameera Bilgrami, Subhasri Ghosh, Riya Raghupathy, Rahul Chadda, Ram Vishwakarma, Madan Rao, and Satyajit Mayor. Nanoclusters of gpi-anchored proteins are formed by cortical actin-driven activity. *Cell*, 135:1085–97, 2008.

[21] Kripa Gowrishankar, Subhasri Ghosh, Suvrajit Saha, C Rumamol, Satyajit Mayor, and Madan Rao. Active remodeling of cortical actin regulates spatiotemporal organization of cell surface molecules. *Cell*, 149:1353–67, 2012.

[22] RC Sarasij, S Mayor, and M Rao. Chirality-induced budding: a raft-mediated mechanism for endocytosis and morphology of caveolae? *Biophys J.*, 92(9):3140–58, 2007.

[23] P Sharma, R Varma, RC Sarasij, Ira, K Gousset, G Krishnamoorthy, M Rao, and S Mayor. Nanoscale organization of multiple gpi-anchored proteins in living cell membranes. *Cell*, 116(4):577–89, 2004.

[24] R Varma and S Mayor. Gpi-anchored proteins are organized in submicron domains at the cell surface. *Nature*, 394:798–3, 1998.

[25] BN Kholodenko, JF Hancock, and W Kolch. Signalling ballet in space and time. *Nat Rev Mol Cell Biol*, 11:414–26, 2010.

[26] SJ Plowman, C Muncke, RG Parton, and JF Hancock. H-ras, k-ras, and inner plasma membrane raft proteins operate in nanoclusters with differential dependence on the actin cytoskeleton. *Proc Natl Acad Sci U S A.*, 102:15500–5, 2005.

[27] Akikazu Fujita, Jinglei Cheng, Minako Hirakawa, Koichi Furukawa, Susumu Kusunoki, and Toyoshi Fujimoto. Gangliosides gm1 and gm3 in

the living cell membrane form clusters susceptible to cholesterol depletion and chilling. *Mol Biol Cell*, 18:2112–10, 2007.

[28] Leventis. Peter A. and Sergio Grinstein. The distribution and function of phosphatidylserine in cellular membranes. *Annu. Rev. Biophys.*, 39:407–20, 2010.

[29] X An, X Guo, H Sum, J Morrow, W Gratzer, and N Mohandas. Phosphatidylserine binding sites in erythroid spectrin: location and implications for membrane stability. *Biochemistry.*, 43:310–5, 2004.

[30] M Muguruma, S Nishimuta, Y Tomisaka, T Ito, and S Matsumura. Organization of the functional domains in membrane cytoskeletal protein talin. *J Biochem.*, 117:1036–42, 1995.

[31] R Makuch, A Zasada, K Mabuchi, K Krauze, CL Wang, and R Dabrowska. Phosphatidylserine liposomes can be tethered by caldesmon to actin filaments. *Biophys J.*, 73:1607–1616, 1997.

[32] S Garg, JX Tang, J Rühe, and CA Naumann. Actin-induced perturbation of ps lipid-cholesterol interaction: A possible mechanism of cytoskeleton-based regulation of membrane organization. *J Struct Biol.*, 168:11–20, 2009.

2

Atomistic Molecular Dynamics Simulation of a Bilayer Membrane

2.1. Introduction

Molecular dynamics (MD) simulation involves solving the classical many body dynamics (Newton's law) relevant to the study of matter consisting of interesting atoms/molecules. This chapter dicusses the theory of modeling of the multicomponent membrane system and the techniques that have been implemented.

2.2. Brief Description of Atomistic Molecular Dynamics Simulations

Molecular dynamics simulations are a numerical interpretation of Newton's law for N-interacting particles, either in the microcanonical ensemble (energy conserved) or the canonical ensemble (including a heat bath with temperature, T) or a constant pressure ensemble (including a pressure barostat).

Thus, in general, we solve Newton's equation of motion for all particles in the simulation box,

$$F_i = m_i a_i \tag{2.1}$$

Here, force, F_i is acting on the i^{th} particle of mass m_i moving with an acceleration a_i.

Let us assume that there are N number of particles in a system and the net potential on the i^{th} particle is V_i, then the force acting on the i^{th} particle is

$$F_i = -\nabla V_i \tag{2.2}$$

In the atomistic molecular dynamics [1–3], the potential on a particle with many short range and long range components, is mainly divided into two interactions: 1. Bonded-Interactions and 2. Nonbonded-Interactions.

1. **Bonded-Interaction**

   a) **Bond Stretching Interaction**

   In a molecule consisting of several atoms, the bond stretching interaction is the interaction between two atoms joined by a covalent bond. This is a 2-body short ranged interaction between the neighbors [1, 2, 4] (shown in Figures 2.1,2.2).

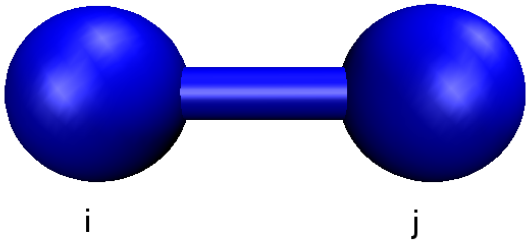

FIGURE 2.1: shows the potential between the i^{th} and j^{th} atoms due to the stretching of bond between them.

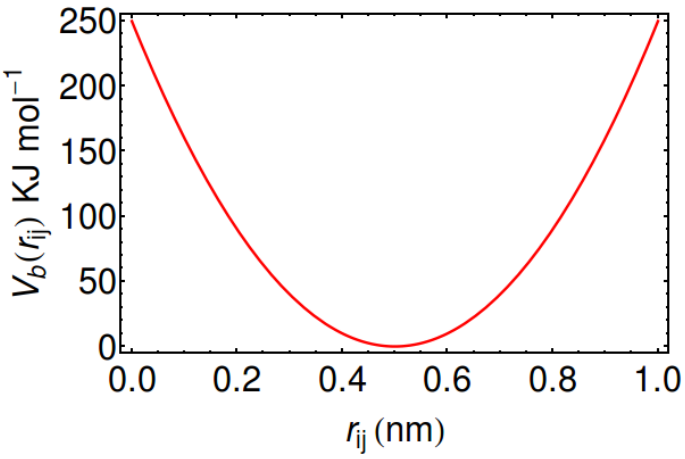

FIGURE 2.2: shows the bond potential between the i^{th} and j^{th} atoms. Here. we put $K^b_{ij} = 2000 KJ mol^{-1} nm^{-2}$ and $r_{0ij} = 0.5\, nm$ to generate the figure.

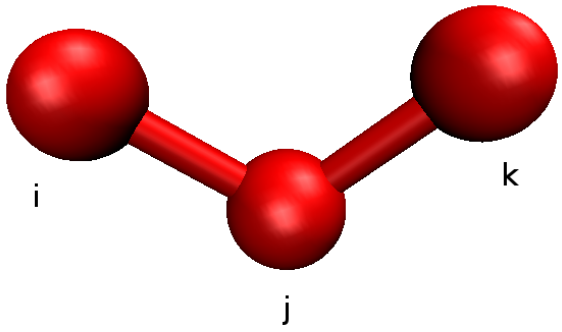

FIGURE 2.3: shows the potential between the i^{th} and k^{th} atoms due to the vibration of the angle, θ_{ijk}.

If i^{th} atom and j^{th} atom in a molecule are joined with covalent bond, then the bond stretching interaction potential, $V_b(r_{ij})$ on the i^{th} atom would be

$$V_b(r_{ij}) = \frac{1}{2} K^b_{ij}(r_{ij} - r_{0ij})^2 \tag{2.3}$$

Here, K^b_{ij} and r_{0ij} are the bond constant and average distance between the two successive atoms, respectively.

b) **Angular Stretching Interaction**

When three successive atoms (i, j and k) are connected with covalent bonds, the interaction between i^{th} and k^{th} atoms due to vibration of the angle, θ_{ijk}, between $i-j$ and $j-k$ bonds is known as angular stretching interaction. It is a 3-body short ranged interaction [1, 5] (Figures 2.3,2.4).

The angular stretching interaction $V_a(\theta_{ijk})$ between the atom i and

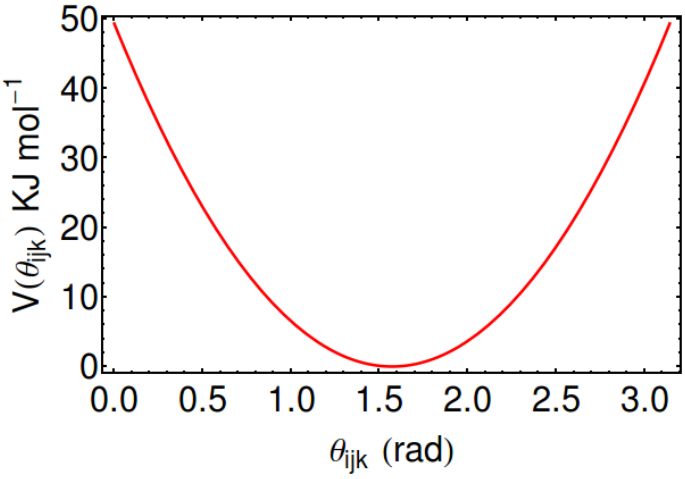

FIGURE 2.4: shows the angular potential between the i^{th} and k^{th} atoms. Here, we put $K^{\theta}_{ijk} = 40KJmol^{-1}rad^{-2}$ and $\Theta_{ijk} = \frac{\pi}{2}\,rad$ to generate the figure.

atom k would be

$$V_a(\theta_{ijk}) = \frac{1}{2}K^{\theta}_{ijk}(\theta_{ijk} - \Theta_{ijk})^2 \tag{2.4}$$

Here, K^{θ}_{ijk} and Θ_{ijk} are angular constant and average angle between the three atoms, respectively.

c) **Dihedral Interaction**

When four successive atoms (i, j, k and l) in a molecule are connected with covalent bonds, the interaction between i^{th} and l^{th} atoms due to the fluctuation of the angle, ζ_{ijkl}, between the two planes made up of $i-j-k$ and $j-k-l$ atoms, is known as dihedral interaction. It is a short ranged 4-body interaction [6–10].

Depending upon the structure, dihedral interactions can be divided into two: improper dihedral interaction and proper dihedral interaction.

i. **Improper Dihedral Interaction**

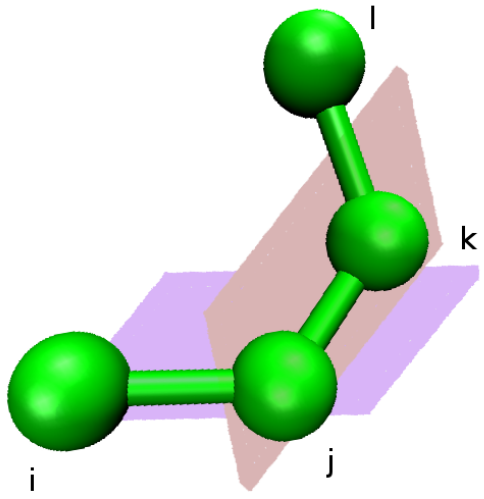

FIGURE 2.5: shows the improper dihedral interaction between the i^{th} and l^{th} atoms due to the vibration of the angle, ζ_{ijkl} between the planes made up of $i-j-k$ atoms and $j-k-l$ atoms.

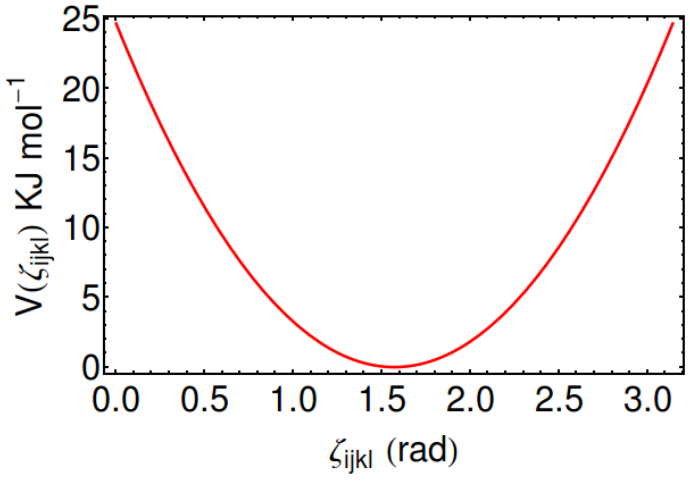

FIGURE 2.6: shows the improper dihedral potential potential between the i^{th} and l^{th} atoms. Here, we choose $K_{id}^{\zeta_{ijkl}} = 20KJmol^{-1}rad^{-2}$ and $\zeta_{0ijkl} = \frac{\pi}{2}\,rad$ to generate the figure.

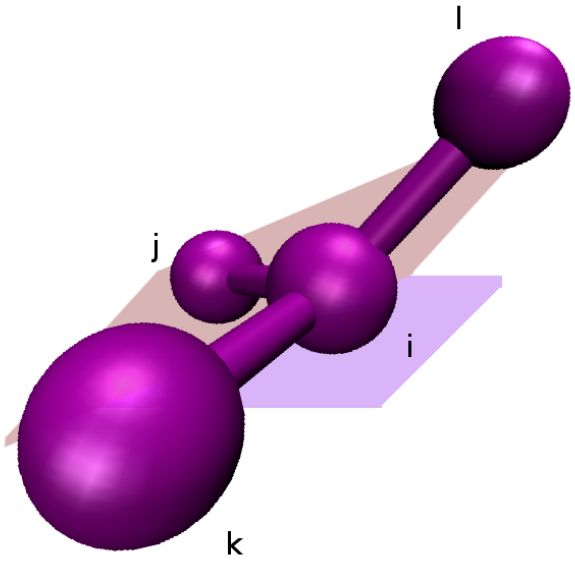

FIGURE 2.7: shows the proper dihedral interaction between the i^{th} and l^{th} atoms due to the vibration of the angle, ζ_{ijkl} between the planes made up of $i-j-k$ atoms and $j-k-l$ atoms.

Improper dihedral interaction, $V_d^i(\zeta_{ijkl})$ (shown in Figure 2.5) helps to maintain the planner structured group in plane; for example in an Aromatic ring, defined as

$$V_d^i(\zeta_{ijkl}) = \frac{1}{2}K_{id}^{\zeta_{ijkl}}(\zeta_{ijkl} - \zeta_{0ijkl})^2 \tag{2.5}$$

It has two constant parameters, namely $K_{id}^{\zeta_{ijkl}}$ and ζ_{0ijkl}. The improper dihedral interaction (Figure 2.6) helps to prevent an aromatic group in a molecule to flip its mirror image [9, 10].

ii. **Proper Dihedral Interaction**

Proper dihedral interaction, $V_d^p(\zeta_{ijkl})$ (shown in Figure 2.7), helps

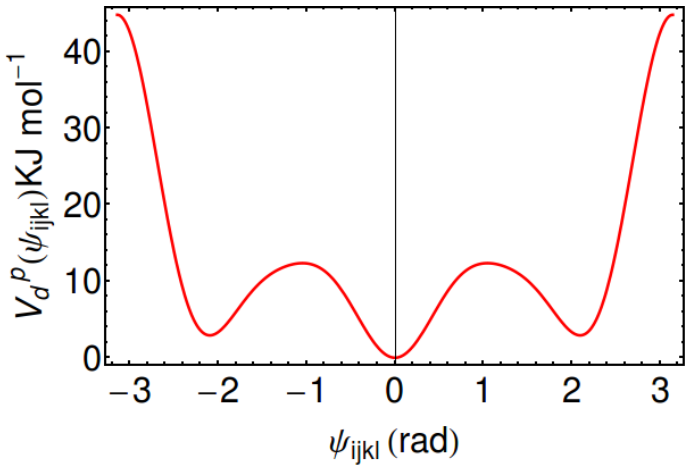

FIGURE 2.8: shows the proper dihedral potential between the i^{th} and l^{th} atoms. Here, we have put $C0 = 9.28$, $C1 = 12.16$, $C2 = -13.12$, $C3 = -3.06$, $C4 = 26.24$ and $C5 = -31.5$ to generate the figure.

in maintaining the cis/trans structure, for example, alkanes. It is defined as

$$V_d^p(\zeta_{ijkl}) = K_{pd}^{\zeta_{ijkl}}(1 + cos(n\zeta_{ijkl} - \zeta_s)) \tag{2.6}$$

Here, $K_{pd}^{\zeta_{ijkl}}$, ζ_s are the relevant parameters to define the proper dihedral interaction.

Indeed, the expression for the proper dihedral interaction, V_d^p for the alkanes is also popular as $V_d^p = \sum_{n=0}^{5} C_n(cos(\psi_{ijkl}))^n$ where $\psi_{ijkl} = \zeta_{ijkl} - 180°$ [9, 10] (Figure 2.8).

2. **Non-bonded-Interaction**

   The interaction between an atom to the 5^{th} atom or far in a same molecule or any other atom of another molecule is considered as non-bonded-interaction which is a long ranged interaction.

   It has mainly the following components:

   a) **Lennard-Jones Interaction**

      Lennard Jones interaction, $V_{LJ}(r_{ij})$ (Figure 2.9), has two parts: one

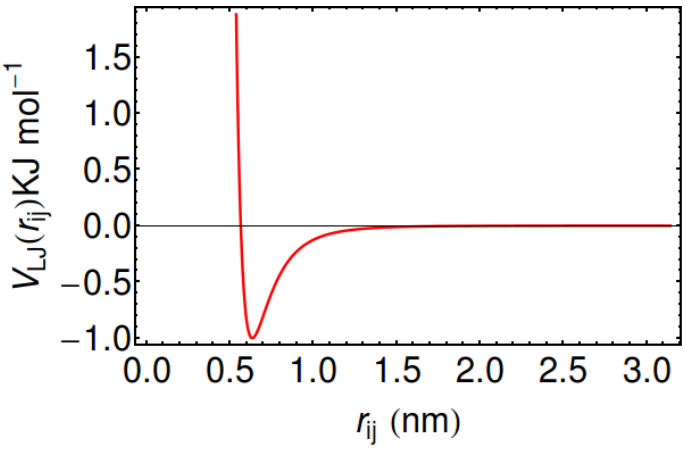

FIGURE 2.9: shows the Lennard Jones potential $V_{LJ}(r_{ij})$ between the i^{th} and j^{th} atoms. Here, we have put $\epsilon = 1.0$ and $\sigma = 0.565$ to generate the figure.

attractive and one repulsive part, commonly used in representing long ranged interaction, defined [11] as

$$V_{LJ}(r_{ij}) = 4\epsilon_{ij}\left(\frac{\sigma^{12}}{r_{ij}^{12}} - \frac{\sigma^{6}}{r_{ij}^{6}}\right) \tag{2.7}$$

Here, ϵ_{ij} and σ are the relevant parameters in Lennard-Jones interaction.

b) **Coulombic Interaction**

Coulombic interaction, $V_c(r_{ij})$ (Figure 2.10), between any two charged atoms having charge q_i and q_j with position r_i and r_j, respectively, is defined [12, 13] as

$$V_c(r_{ij}) = \frac{1}{4\pi\epsilon_0}\frac{q_i q_j}{r_{ij}} \tag{2.8}$$

where $r_{ij} = r_i - r_j$. Here, ϵ_0 is the dielectric constant of the medium.

Therefore, sum of all short ranged and long ranged interactions gives rise to the net potential V_i on the i^{th} particle as,

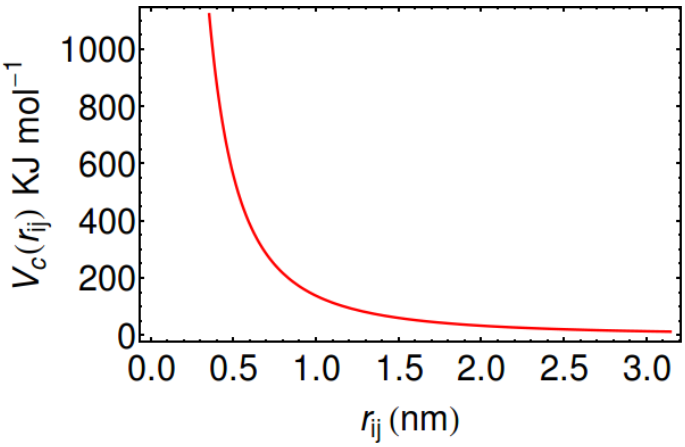

FIGURE 2.10: shows the Coulombic potential, $V_c(r_{ij})$, between the i^{th} and j^{th} atoms. Here, we have put $\frac{1}{4\pi\epsilon_0} = 138.935485 kJ\, mol^{-1}\, nm\, e^{-2}$ and $q_{i,j} = 1.0\, e$ to generate the figure.

$$
\begin{aligned}
V_i &= V_b(r_{ij}) + V_a(\theta_{ijk}) + V_d(\zeta_{ijkl}) + V_{LJ}(r_{ij}) + V_c(r_{ij}) \\
&= \frac{1}{2}K^b_{ij}(r_{ij} - r_{0ij})^2 + \frac{1}{2}K^\theta_{ijk}(\theta_{ijk} - \Theta_{ijk})^2 + \frac{1}{2}Kid^\zeta_{ijkl}(\zeta_{ijkl} - \zeta_{0ijkl})^2 \\
&\quad + Kpd^\zeta_{ijkl}(1 + cos(n\zeta_{ijkl} - \zeta_s)) + 4\epsilon_{ij}\left(\frac{\sigma^{12}}{r^{12}_{ij}} - \frac{\sigma^6}{r^6_{ij}}\right) + \frac{1}{4\pi\epsilon_0}\frac{q_i q_j}{r_{ij}} \qquad (2.9)
\end{aligned}
$$

Apart from these, due to restrain of position, angle, distance, orientation and dihedral angle, we have to incorporate the restrain interactions [8, 14–16].

Moreover, we need to introduce appropriate reservoirs and boundary conditions to ensure the conservation of the energy of the system. We add heat bath such as Berendsen [17] or Nose-Hoover thermostat [18, 19] to get constant temperature and Barostat to attain constant pressure ensemble [20, 21].

2.3. Steps to execute MD simulation of Bilayer Membrane

We use GROMACS (http://www.gromacs.org) [8] to integrate the Newton's equation of motion (Eq. 2.2) using Leap-frog algorithm in the atomistic MD simulation.

The step size of time integration in the MD simulation is set by the accuracy needed to model a system. Here, in the atomistic MD simulation, we want to mimic the system at atomic level where the smallest quantity is the bond stretching vibration of the hydrogen atoms in which shortest oscillation period is approximately $13\,fs$. Therefore, we set our simulation time step as $2\,fs$ so that we get $5-6$ integration time steps to get enough data for measuring the smallest quantity of the system.

2.3.1. Force fields

The force field parameters for POPC, PSM, PS and Chol have been taken from the previous validated united-atom description [22–25]. The parameters of GPI have been constructed from the previous validated description of glycolipid [26, 27]. We have used improved extended simple point charge (SPC/E) model to simulate water molecules, having an extra average polarization correction to the potential energy function.

The long range electrostatic interactions are incorporated by the reaction-field method with cut-off $r_c = 2\,$nm, while for the Lennard-Jones interactions we use a cut-off of $1\,$nm [23, 24, 28].

2.3.2. Initial configurations

We study single to multicomponent, symmetric to asymmetric bilayer membranes. All multicomponent bilayer membranes have 512 lipids in each leaflet (with a total 1024 lipids) and 32768 water molecules (such that the ratio of water to lipid is $32 : 1$) so as to completely hydrate the simulated lipid bilayer. We have generated the initial configurations of all the asymmetric multicomponent bilayer membrane using *PACKMOL* [29]. For all simulations of ternary bilayer membranes, we choose two sets of initial conditions : (i) where the components in each leaflet are homogeneously mixed and (ii) where the ternary components are completely phase-segregated in l_o-l_d domains [24].

2.3.3. Choice of ensembles and equilibration

The asymmetric bilayers are equilibrated for 50 ps in the NVT ensemble using a Langevin thermostat to avoid bad contacts arising from steric constraints and then for 160 ns in the NPT ensemble ($T = 296$ K (23°C), $P = 1$ atm). The simulations are carried out in the NPT ensemble for the first 20 ns using Berendsen thermostat and barostat, then for 20 ns using Nose-Hoover thermostat and the Parrinello-Rahman barostat to produce the correct ensemble. Rest of the simulations are performed in the NPT ensemble using Berendsen thermostat. We use a semi-isotropic pressure coupling with compressibility 4.5×10^{-5} bar^{-1} for the simulations in the NPT ensemble.

For each initial configuration, we run the simulations for 200 ns. We compute the desired physical quantities from the last 20 ns of the trajectories.

2.4. Equilibration and Stability of Bilayer Membrane

To make sure that a stable, surface-tensionless equilibrated bilayer is being simulated, we check the thermal and mechanical equilibration of the system.

2.4.1. Thermal Equilibration

Area per Lipid

We have used the time dependence of the area per lipid (Figure A.3, A.5 and A.6) to test for equilibration (≈ 20 ns) and have run the simulation for times longer than that.

2.4.2. Mechanical Equilibration

Stress Profile Calculation

The stress profiles in the bilayer are measured using Irving-Kirkwood contour dividing the bilayer in 0.1 nm thick slabs. Pairwise forces are calculated by rerunning the trajectory with cut-off $2\,nm$ for electrostatic interactions. We employ the LINCS algorithm to constrain the bond lengths [14] and the SETTLE algorithm to keep the water molecules rigid [15] so that integrator time step of $2\,fs$ could be used. The pressure profiles are generated from trajectories over $20\,ns$ using SHAKE algorithm [16] to constrain bond lengths.

To make sure that a stable, surface tension-less asymmetric bilayer is being simulated, the forces, torques and surface tension of the bilayer are computed from the local stress tensor $\sigma_{ij}(x, y, z)$

$$\sigma_{ij}(x, y, z) = \frac{1}{v} \sum_{\alpha} f_i^{\alpha} r_j^{\alpha} \tag{2.10}$$

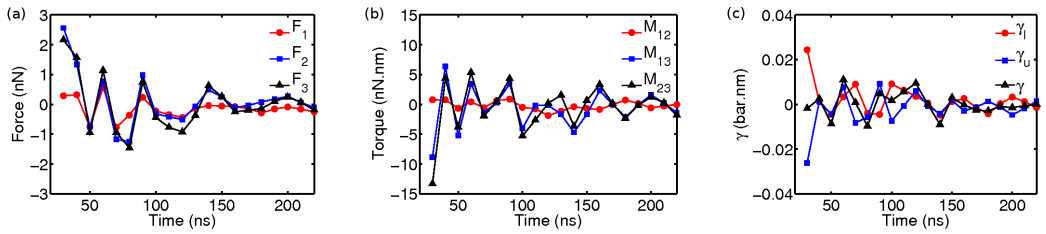

FIGURE 2.11: shows the time variation of net force, toque and surface tension of the asymmetric ternary (POPC+PSM+Chol) bilayer membrane.

where f_i^{α} is the i^{th} component of the force on the α^{th}-particle due to all other particles within a coarse-grained volume $v = [0.1\,nm]^3$.

Force and Torque Calculation

From the MD simulation runs over the last 20 ns, we use the virial to calculate the net force $F_i = \int \partial_k \sigma_{ik}\, dv$ and torque $M_{ik} = \int (\partial_l \sigma_{il} x_k - \partial_l \sigma_{kl} x_i)\, dv$ where i, j, k runs from $1, 2, 3$ (corresponding to the x, y and z components) (shown in Figure 2.11 (a) and (b)). This is to ensure that the model membrane is both force and torque balanced. In addition, to ensure that the membrane is tensionless, we compute the surface tension as $\gamma = \int \pi(z) dz$ where $\pi(z) = \frac{1}{2}\left(\overline{\sigma}_{xx}(z) + \overline{\sigma}_{yy}(z)\right) - \overline{\sigma}_{zz}(z)$, the lateral pressure, is integrated over the width of the bilayer (shown in Figure A.11, A.13, A.14) [23, 24].

It is important to note that stress is a tensor of rank 2 having 9 $(= 3 \times 3)$ components whereas force is tensor of rank 1 having 3 components for a 3 dimensional system. (N.B. Scalar is a tensor of rank 0). For $d = N$, such that N is a real number, stress tensor would have $N \times N$ components.

Moreover, we neglect the local protrusion and undulation and assume our bilayer (system) as flat membrane. For arbitrary system shape, one should be careful with the topology of the system and redefine the Cartesian coordinate system of d dimension to the corresponding curvilinear coordinate system with same dimensions.

Now, some important things should be noted before calculating the M_{ik}. The torque is a tensor rank 2 having 9 components. But, from the expression of

the torque, M_{ik}, we notice that diagonal terms, $M_{ii} = 0$. Again, an important property is that it is a symmetric matrix i.e., $M_{ij} = M_{ji}$ while $i \neq j$. Therefore, only 3 unknown components remain to be computed instead of 9 i.e., M_{12}, M_{13} and M_{23}.

Surface Tension Calculation

The lateral pressure $\pi(z)$, (shown in Figure 2.11 (c)) is given by [30, 31]

$$\pi(z) = \frac{1}{2}\left(\overline{\sigma}_{xx}(z) + \overline{\sigma}_{yy}(z)\right) - \overline{\sigma}_{zz}(z), \tag{2.11}$$

The membrane surface tension γ is calculated as

$$\gamma = \int \pi(z) dz \tag{2.12}$$

in which $\pi(z)$ is integrated over the width of the bilayer.

In Figure A.11, the pressure profiles of symmetric and asymmetric bilayers are shown for comparison. In contrast to the asymmetric bilayer, the symmetric bilayer exhibits a symmetric pressure profile about the midplane. On the other hand the pressure profile of the asymmetric bilayer shows larger spatial oscillations.

2.5. Analysis of Physical Quantities of the bilayer membrane

2.5.1. Local concentration of the components

The local concentration of the components (say POPC) of each leaflet of the bilayer membrane have been calculated from the 2d-histogram of the coordinate of the head-group (P-atom). Here, we have collected the $x-y$ components of the coordinates of the head-group of the lipid and the data are binned with a grid size $= 1.5\,nm$. Finally, we get the local concentration of the POPC by averaging the data over 20 ns. Note that we ignore the size and shape of the lipid. This calculation is important to get the information about the lateral heterogeneity of the components of bilayer membrane where all the lipids of the membrane are distributed in $x-y$ plane and are aligned along z-axis.

2.5.2. Local Thickness of the bilayer membrane

The thickness of the bilayer membrane, (shown in Figure 2.12) is calculated from the head-to-head (P-atoms of POPC and PSM) distance of the lipids in the upper and lower leaflets of the bilayer. To avoid errors coming from the possible mis-alignment of the lipids in two leaflets, the positions of the head group (P-atom) of the lipids in the two leaflets are binned in xy-plane separately. Thus, the local bilayer thickness is constructed using x-y grids for the upper and lower leaflet of the bilayer, with grid size $= 1.95$ nm. An average over the z-coordinates of the phosphorus atom in the head groups of POPC and PSM within each $x-y$ grid is then performed. The difference between the z-coordinates corresponding to the same $x-y$ grid of the two leaflets gives the local bilayer thickness [23, 24].

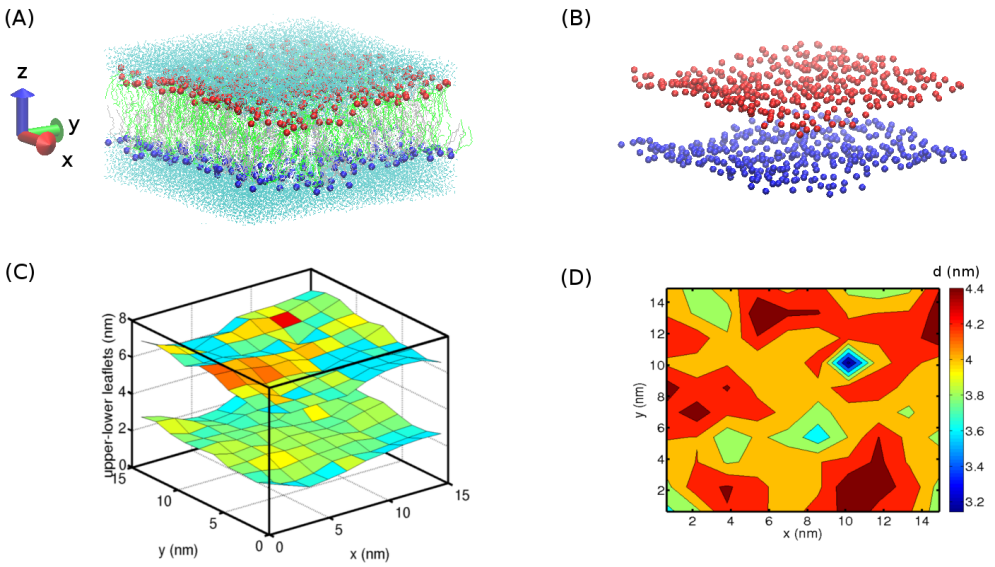

FIGURE 2.12: shows the protocol to calculate spatial variation of the thickness (d) of the bilayer membrane. To calculate the spatial varaition of the thickness of the ternary (POPC + PSM + Chol) symmetric bilayer membrane Figure 2.12 (A), we have collected the coordinates of the atom 'P' of the lipids as a representation of the head groups of the lipid bilayer membrane Figure 2.12 (B). From the data, we construct the surfaces both for upper and lower leaflets separately using x-y grids with grid size $= 1.95$ nm Figure 2.12 (C). The differences beteen the z-coordinates corresponding to the upper and lower leaflets with same $x - y$ coordinates, gives us the spatial varaiation of the thickness of the bilayer membrane Figure 2.12 (D).

2.5.3. Local Deuterium Order Parameter of the bilayer membrane

The deuterium order parameter (S) values are calculated from the position of selected carbon atoms of the PSM and POPC lipid chains. In our atomistic MD simulations, S is defined for every selected CH_2 group in the chains as, $S \equiv \frac{1}{2}\langle 3\cos^2\theta - 1\rangle$ where θ is the angle between a CH-bond and the normal to the plane of the membrane (z-axis). Since we have used a united atom model description in our simulation, we have to reconstruct the CH-bond from the positions of successive CH_2-groups, assuming tetrahedral geometry of the CH_2-groups. For each molecule, an averaging is done over the two bonds in

each CH_2-group. This is then coarse-grained (binned) over a spatial scale of 1.56 nm and time scale of 20 ns. For the present purposes, carbon atoms $5-7$ were selected from each acyl chains (corresponding to palmitoyl-oleoyl chains of POPC, and palmitoyl-sphingosine of PSM). This choice of carbon atoms best characterizes the acyl chain rigidity induced by the proximal cholesterol [23, 24].

References

[1] Michael P. Allen and Dominic J. Tildesley. *Computer Simulation of Liquids*. Oxford University Press, 1989.

[2] Daan Frenkel and Berend Smit. *Understanding Molecular Simulation, Second Edition: From Algorithms to Applications*. Academic Press, 2001.

[3] D. C. Rapaport. *The Art of Molecular Dynamics Simulation*. Cambridge University Press, 2004.

[4] Martin J. Field. *A practical introduction to the simulation of molecular systems*. Cambridge University Press, 2007.

[5] Alan Hinchliffe. *Molecular Modeling for beginners*. Wiley, 2003.

[6] H Bekker, H. J. C. Berendsen, E. J. Dijkstra, S. Achterop, R. van Drunen, D. van der Spoel, A. Sijbers, H. Keegstra, B. Reitsma, and M. K. R. Renardus. *Gromacs: A parallel computer for molecular dynamics simulations.* World Scientific, 92.

[7] H. J. C. Berendsen, D. van der Spoel, van Drunen, and R. Gromacs: A message-passing parallel molecular dynamics implementation. *Comp. Phys. Comm.*, 91:43–56, 1995.

[8] E. Lindahl, B. Hess, and D van der Spoel. Gromacs 3.0: A package for molecular simulation and trajectory analysis. *J. Mol. Mod*, 7:306–317, 2001.

[9] D. van der Spoel, E. Lindahl, B. Hess, G. Groenhof, A. E. Mark, and H. J. C Berendsen. Gromacs: Fast, flexible and free. *J. Comp. Chem.*, 26:701–1718, 2005.

[10] B. Hess, C. Kutzner, D. van der Spoel, and E. Lindahl. Gromacs 4: Algorithms for highly efficient, load-balanced, and scalable molecular simulation. *J. Chem. Theory Comp.*, 4:435–447, 2008.

[11] Peter Atkins and Julio de Paula. *Physical Chemistry*. W. H. Freeman and Company.

[12] David J. Griffiths. *Introduction to Electrodynamics*. Prentice Hall.

[13] John David Jackson. *Classical Electrodynamics*. Wiley.

[14] Berk Hess, Henk Bekker, Herman J. C. Berendsen, and Johannes G. E. M. Fraaije. Lincs: A linear constraint solver for molecular simulations. *J Comput Chem.*, 18:1463–1472, 1997.

[15] Shuichi Miyamoto and Peter A. Kollman. Settle: An analytical version of the shake and rattle algorithm for rigid water models. *J. Comput. Chem.*, 13:952–962, 1992.

[16] Jean-Paul Ryckaert, Giovanni Ciccotti, and Herman J.C Berendsen. Numerical integration of the cartesian equations of motion of a system with constraints: molecular dynamics of n-alkanes. *J. Comput. Phys.*, 23:327–341, 1977.

[17] H. J. C. Berendsen. Transport properties computed by linear response through weak coupling to a bath. *Computer Simulation in Materials Science*, 205:139–155, 1991.

[18] William G. Hoover. Canonical dynamics: Equilibrium phase-space distributions. *Phys. Rev. A*, 31:1695–1697, Mar 1985.

[19] S Nosé. A molecular dynamics method for simulations in the canonical ensemble. *Molecular Physics*, 100:191–198, 1984.

[20] S Nosé and M. L. Klein. Constant pressure molecular dynamics for molecular systems. *Molecular Physics*, 50:1055–1076, 1983.

[21] M. Parrinello and A. Rahman. Polymorphic transitions in single crystals: A new molecular dynamics method. *J. Appl. Phys.*, 52:7182, 1981.

[22] Parag Mukhopadhyay, Luca Monticelli, and D. Peter Tieleman. Molecular dynamics simulation of a palmitoyl-oleoyl phosphatidylserine bilayer with na+ counterions and nacl. *Biophys J.*, 86(3):1601–1609, 2004.

[23] Perttu S Niemelä, Samuli Ollila, Marja T Hyvönen, Mikko Karttunen, and Ilpo Vattulainen. Assessing the nature of lipid raft membranes. *PLoS Comput Biol.*, 3(2):e34, 2007.

[24] A Polley, S Vemparala, and M Rao. Atomistic simulations of a multicomponent asymmetric lipid bilayer. *J Phys Chem B.*, 116(45):13403–10, 2012.

[25] D P Tieleman and H J Berendsen. A molecular dynamics study of the pores formed by escherichia coli ompf porin in a fully hydrated palmitoyloleoylphosphatidylcholine bilayer. *Biophys J.*, 74(6):2786–2801, 1998.

[26] A Hall, T Róg, M Karttunen, and I Vattulainen. Role of glycolipids in lipid rafts: a view through atomistic molecular dynamics simulations with galactosylceramide. *J. Phys. Chem. B*, 114:7797–7807, 2010.

[27] Tomasz Róg, Ilpo Vattulainen, Alex Bunker, and Mikko Karttunen. Glycolipid membranes through atomistic simulations: Effect of glucose and galactose head groups on lipid bilayer properties. *J. Phys. Chem. B*, 111 (34):10146–10154, 2007.

[28] Michael Patra and Mikko Karttunen. Lipid bilayers driven to a wrong lane in molecular dynamics simulations by subtle changes in long-range electrostatic interactions. *J. Phys. Chem. B*, 108 (14):4485–4494, 2004.

[29] L Martínez, R Andrade, EG Birgin, and JM Martínez. Packmol: a package for building initial configurations for molecular dynamics simulations. *J Comput Chem.*, 30(13):2157–64, 2009.

[30] Michael Patra. Lateral pressure profiles in cholesteroldppc bilayers. *Eur. Biophys. J.*, 35:79–88, 2005.

[31] Samuel A. Safran. *Statistical Thermodynamics of Surfaces, Interfaces, and Membranes*. Addison-Wesley, 1994.

3

Atomistic Simulations of a Multicomponent Asymmetric Lipid Bilayer

3.1. Introduction

The cell membrane is characterized by both lateral and transverse lipid heterogeneity, an aspect of significant functional consequence [1]. Transverse lipid heterogeneity is maintained actively by the cell, making the cell bilayer intrinsically asymmetric. Lateral lipid heterogeneities [2, 3] such as those observed in ternary mixtures of sphingomyelin (PSM), phosphatidyl Choline (PC) and cholesterol (Chol) molecules have been implicated in a variety of cellular processes including signaling and endocytosis. Asymmetry in bilayers can arise both in terms of difference in constituent lipids or in number of lipid molecules

in both leaflets. In spite of this obvious lateral/transverse compositional heterogeneity, except for a few seminal studies[4], most in-vitro investigations of multicomponent artificial membranes [5–7] have been done on symmetric bilayers. Further, most of the atomistic simulations of model cell membrane mimics, have been carried out on systems which either have lateral heterogeneity [8, 9] or transverse asymmetry [10–12] but rarely both. There have however been a few studies using coarse-grained simulations [13–15] and continuum Landau theories [16, 18, 19] that address the role of inter-bilayer coupling in equilibrium physical properties and domain growth.

While early simulations of model membranes consisted only of a single-component PC bilayers [20–22], later simulations have incorporated more than one lipid component, in particular cholesterol [23]. Following the 'raft proposal' of the importance of PSM molecules in raft formation, an increasing number of simulations with PSM molecules [24] have been carried out. These simulations include detailed comparisons between mixtures of PSM and Chol and PC and Chol [8, 9, 25–28]. Finally, simulations on asymmetric bilayers have also been reported. A simulation study by Bhide et al. [29] was performed on systems consisting of PSM and Chol molecules in upper leaflet and SOPS and Chol molecules in the lower leaflet, with equal number of phospholipids in both the leaflets. Comparisons between each leaflet of the asymmetric bilayer with corresponding simulations of symmetric bilayers showed no significant differences in their physical properties.

In this chapter, the equilibrium properties and dynamics of coarsening of a multicomponent asymmetric (both lateral and transverse) bilayer using atomistic molecular dynamics (MD) simulations are studied. Specifically, the physical properties of a 3-component asymmetric lipid bilayer comprising of an unsaturated POPC, a saturated PSM and Chol molecules, which exhibits lateral compositional heterogeneities in the form of liquid ordered (l_o) - liquid disordered (l_d) domains, thought to represent the characteristic lipid composition

of rafts on the cell membrane, are investigated. In addition to studying a variety of order parameters, their correlations and spatial distribution, transport properties of the component lipid molecules are also studied. Our study suggests that the presence of lateral heterogeneities in the bilayer can potentially affect the molecular diffusion at short time scales, which may be of relevance to molecular diffusion at the cell surface. However lipid based lateral heterogeneities on the cell surface are likely to be small and below optical resolution; it is only recently that advances in high resolution single-particle tracking (SPT) [30, 31] allow one to measure subtle changes in diffusion characteristics as molecules move across the heterogeneous cell surface. In addition, the transverse asymmetry would suggest that the diffusion characteristics of the molecule is different in the two leaflets of the bilayer. Correlations between the local physical environment and the tagged particle diffusion are also investigated in this chapter.

3.2. Model membrane

Two bilayer model systems have been simulated : (A) a symmetric three-component bilayer consisting of 170 POPC, 171 palmitoyl-sphingomyelin (PSM, saturated lipid) and 171 Chol whose ratio is $1:1:1$ in each leaflet, for a total 1024 lipids and (B) an asymmetric bilayer with a composition of 170 POPC, 168 PSM and 171 Chol whose ratio is roughly $1:1:1$ in the upper leaflet and 256 POPC and 256 Chol whose ratio is $1:1$ in the lower leaflet, for a total 1024 lipids. Two control systems have also been simulated, which are (C) a symmetric one-component bilayer made up of a total 128 pure POPC and (D) a symmetric two-component bilayer made up of a total 64 POPC and 64 Chol whose ratio is $1:1$ in both leaflets.

The two model systems A and B have been simulated starting from two sets

of initial conditions : (i) where the components in each leaflet are homogeneously mixed and (ii) where the ternary components are completely phase segregated (Figure 3.1).

The details of methods of the simulations are given in Chapter 2.

3.3. Results and discussion

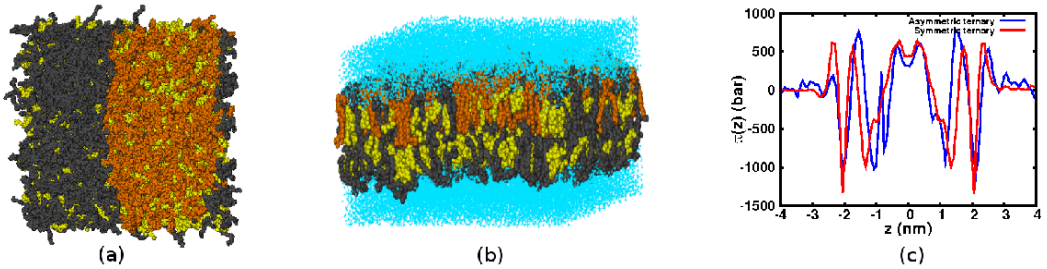

FIGURE 3.1: (a) Snapshot (top view) at the end of the simulation starting from a fully segregated configuration of the ternary system POPC (gray), PSM (orange), Chol (yellow) forming a stable asymmetric bilayer in water (not shown for visual clarity). (b) Snapshot (side view) at the end of the simulation starting from a homogeneous mixed configuration of the same asymmetric bilayer in water (cyan). (b) Lateral pressure profiles $\pi(z)$ as a function of position across the bilayer, for the ternary asymmetric bilayer (blue), and the ternary symmetric bilayer (red). (Lateral pressure profiles for symmetric bilayers made of POPC and POPC+Chol shown in Chapter 2). See Results for definition.

To make sure that a stable, surface tension-less asymmetric bilayer is being simulated, the forces, torques and surface tension of the bilayer are computed from the local stress tensor $\sigma_{ij}(x,y,z) = \frac{1}{v}\sum_\alpha f_i^\alpha r_j^\alpha$, where f_i^α is the i^{th} component of the force on the α^{th}-particle due to all other particles within a coarse-grained volume $v = [0.1\,nm]^3$.

The net force $F_i = \int \partial_k \sigma_{ik}\, dv$ and its first moment (related to the torque) $M_{ik} = \int (\partial_l \sigma_{il} x_k - \partial_l \sigma_{kl} x_i)\, dv$ for the bilayer were computed and both force and torque balance – $F_1 = 0.29 \pm 3.34$, $F_2 = -2.56 \pm 2.09$, $F_3 = -2.16 \pm 3.2$, in units of nN and $M_{12} = 0.77 \pm 0.428, M_{13} = -8.83 \pm 2.04, M_{23} = -13.303 \pm 1.67$,

in units of nN·nm were achieved suggesting a mechanically stable asymmetric bilayer. These are comparable to the corresponding values for the symmetric bilayers (see Appendix A). The membrane surface tension is calculated as $\gamma = \int \pi(z)dz$, integrated over the width of the bilayer, where $\pi(z)$ is the lateral pressure, given by $\pi(z) = \frac{1}{2}\left(\overline{\sigma}_{xx}(z) + \overline{\sigma}_{yy}(z)\right) - \overline{\sigma}_{zz}(z)$ [32, 33], resulting in a value of $\gamma = -0.0018 \pm 0.0301$ bar-nm, essentially a 'zero' surface tension bilayer. More details of time dependence of net forces, their moments and surface tension are provided in Chapter 2, Figure 2.11. A snapshot of the equilibrium bilayer configuration of the asymmetric membrane is shown in Figure 3.1(a,b). In Figure 3.1(c), the pressure profiles of symmetric and asymmetric bilayers are shown for comparison. In contrast to the asymmetric bilayer, the symmetric bilayer exhibits a symmetric pressure profile about the midplane. On the other hand the pressure profile of the asymmetric bilayer shows larger spatial oscillations.

As mentioned in previous section, the simulations on systems A and B have been carried out from two sets of initial conditions. One set of initial conditions is where the composition is *homogeneously mixed* in each leaflet; with this as the configuration at time $t = 0$, the membrane was quickly seen to enter a coarsening regime (as explicitly demonstrated below), with l_o-domains, enriched in cholesterol and PSM, growing slowly (algebraically) in time. We will see below that the dynamics by which domains grow corresponds to the well-known coarsening dynamics of phase segregation [34], which implies that there is both local equilibrium and an *approach towards global equilibrium*. The time taken to attain global equilibrium however gets larger as the system size gets larger, in all runs on system B we have gone upto 220 ns. The other set of initial conditions is where the composition is completely segregated; with this as initial condition, the configuration was seen to very quickly attain equilibrium phase segregation with large domain coexistence. We have used the time dependence of the area per lipid (see Appendix A) to test for equilibration

(≈ 20 ns) and have run the simulation for times longer than that.

Both these initial conditions are important. The first one tells us that the homogeneous mixed phase is unstable, the coarsening dynamics suggests that it *approaches* global equilibrium. The second tells us that the global segregated equilibrium phase is stable. The bulk properties at late times from these two initial conditions are expected to be consistent, as explicitly demonstrated below. In each of the subsections below, we have presented results from both these initial conditions.

3.3.1. Lipid composition

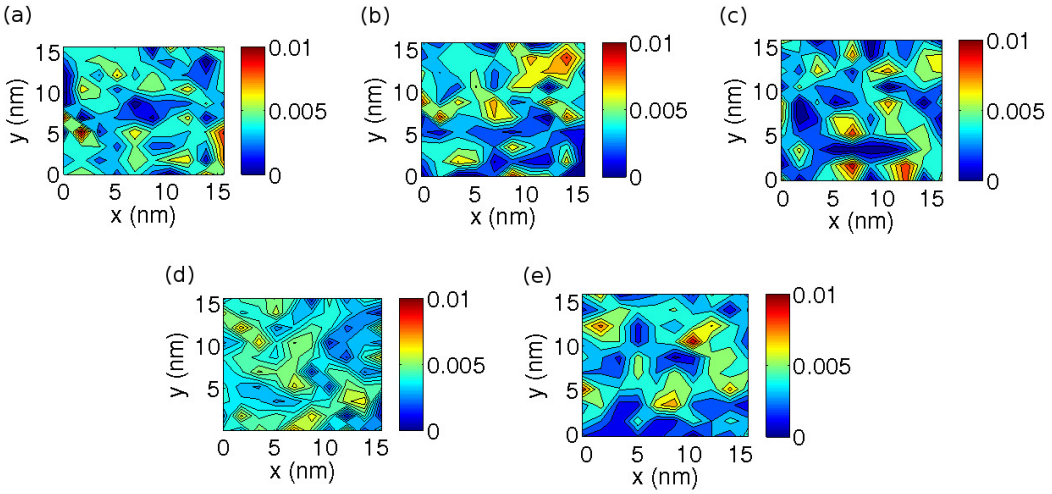

FIGURE 3.2: Spatial variation of lipid concentration in the asymmetric ternary bilayer system in the coarsening regime : (a) POPC, (b) PSM, (c) Chol in the upper leaflet, and (d) POPC and (e) Chol in the lower leaflet. The LUT bars denote the fraction of the lipid species within an area $[1.56\,nm]^2$.

At the temperature and overall lipid composition under consideration, the homogeneous mixed phase of both the asymmetric and symmetric bilayers is unstable and exhibits definite features of phase separation between POPC-rich and PSM-rich domains (shown in Figure 3.2,3.3); in the asymmetric bilayer

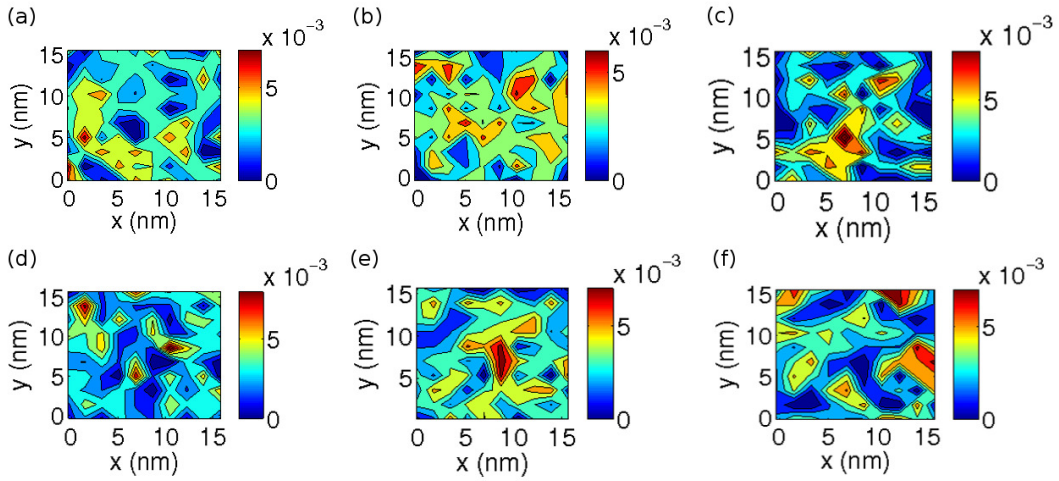

FIGURE 3.3: Spatial variation of lipid concentration in the symmetric ternary bilayer system in the coarsening regime : (a) POPC, (b) PSM, (c) Chol in the upper leaflet, and (d) POPC, (e) PSM and (f) Chol in the lower leaflet. The LUT bars denote the fraction of the lipid species within an area $[1.56\,nm]^2$. Note from (b) that the domain sizes are larger than in the asymmetric bilayer.

phase segregation occurs in the upper leaflet alone, while the composition in the lower leaflet remains homogeneous. To show that the bilayer is undergoing phase separation towards a complete phase segregated configuration, the theory of dynamical coarsening [34], which deals with the study of the dynamics of domain formation starting from a complete disordered phase is used. In simulations starting from an initial mixed state, it is found that the system quickly phase segregates; at early times the domain sizes are small and grow over the simulation time, 220 ns. To demonstrate that at these times the system enters a nonlinear coarsening regime (a hallmark of phase segregation leading to an eventual completely phase segregated state), we have computed the time dependence of (i) the probability distribution $P(\phi)$ of the order parameter $\phi = \frac{\rho_{\mathrm{SM}} - \rho_{\mathrm{POPC}}}{\rho_{\mathrm{SM}} + \rho_{\mathrm{POPC}}}$ of the asymmetric bilayer membrane, model B (where $\rho_{\mathrm{SM/POPC}}$ is the local density of PSM/POPC), and (ii) the energy density $\epsilon = E/V$, where the energy $E \propto \int d^2r\,(\nabla\phi)^2$. In Figure 3.4 (a), we have shown the $P(\phi)$ of the

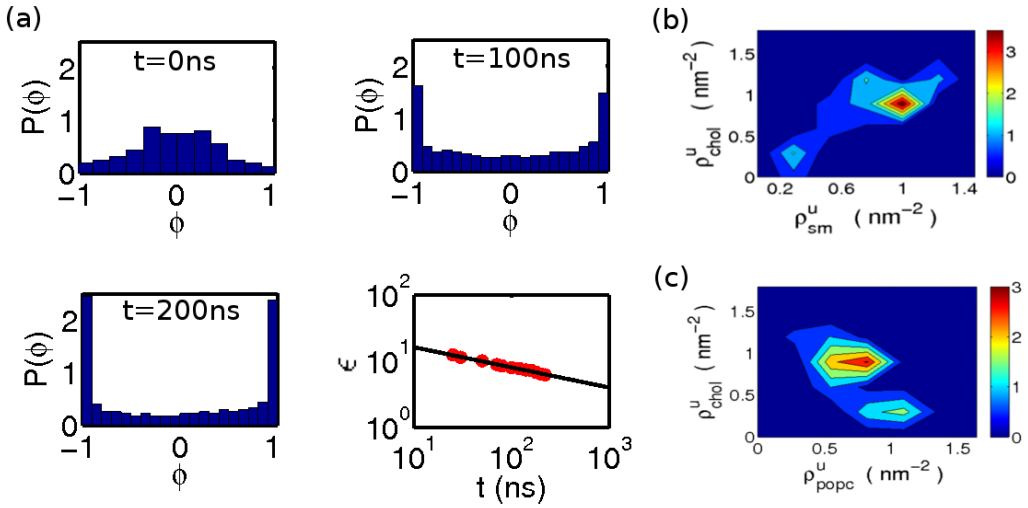

FIGURE 3.4: (a) Probability distribution $P(\phi)$ (normalized) of the order parameter $\phi = \frac{\rho_{\mathrm{SM}} - \rho_{\mathrm{POPC}}}{\rho_{\mathrm{PSM}} + \rho_{\mathrm{POPC}}}$, where ρ_{PSM} and ρ_{POPC} are the concentrations of PSM and POPC, respectively, in the asymmetric ternary bilayer. Its time dependence from $t = 0 - 200$ ns, shows that the system, initially prepared in the mixed state ($\phi = 0$), has coarsened into PSM rich ($\phi = 1$) and POPC rich ($\phi = -1$) domains separated by sharp interfaces. The last panel shows the dependence of the energy density ϵ with time. The data (red filled circles) suggests that ϵ goes as a power-law, $\epsilon \sim t^{-.3\pm0.15}$ (fitted line), with an exponent consistent with dynamical scaling, $z = 3$. (b) Joint probability distribution (color bar) of the concentration (in units of $\mathrm{number/nm^2}$) of (b) PSM and Chol and (c) POPC and Chol, coarse-grained over $[1.73\,\mathrm{nm}]^2$ in the upper leaflet and averaged over 20 ns. Red shows the highest joint probability and blue the lowest. Note the strong correlation (anticorrelation) between PSM-Chol (POPC-Chol), respectively. The figures clearly show an enrichment of cholesterol in PSM-enriched domains by a ratio $3:1$.

asymmetric ternary bilayer at initial ($t = 0\,ns$), final ($t = 200\,ns$) and intermediate time ($t = 100\,ns$). Initially $P(\phi)$ is peaked at $\phi = 0$ (mixed state) and subsequently evolves into a distribution with two peaks at ± 1 (phase coexistence of POPC-rich and PSM-rich domains). As time progresses ($t = 100\,ns$ and $t = 200\,ns$), the peaks at ± 1 get progressively sharper and the weight at $\phi = 0$ diminishes, suggesting that the domain boundaries are getting sharper and that the value of ϕ *within* the domains approaches the value at equilibrium.

We calculate the *scaling* of the domain size with time in the coarsening

regime, through the computation of the scaling of the energy density. The relation between the scaling of the energy density and the domain size $R(t)$ in d dimensions (here $d = 2$) is the following : $\epsilon(t) \sim \frac{R^{d-1}}{R^d} \sim R^{-1}(t) \sim t^{-1/z}$, where $z = 3$ is the expected dynamical exponent. In addition, at one place we say that from a visual inspection of the configurations we find that the domain size in the ternary asymmetric bilayer is larger than that in the symmetric bilayer. This statement can be made more quantitatively by comparing the value of the energy densities at the same time. One prescription for computing the domain size is via the radial distribution function $g(r)$, however we have found that for the system sizes under consideration, this is very noisy.

To show that we are in the coarsening regime, we need to verify the energy density scaling, which measures the time dependence of the amount of interface separating the two phases (it is more convenient to compute the energy density in Fourier space). This decreases in time, in the dynamical scaling regime, which characterizes nonlinear coarsening. Our simulations show that $1/z = 0.30 \pm 0.15$, consistent with this scaling prediction (Figure 3.4(a)).

As mentioned earlier, this demonstration of coarsening towards the phase segregated state shows that (i) the homogeneous mixed phase is unstable, (ii) the order parameter within the domains is in local equilibrium and (iii) the configurations are slowly evolving towards global phase segregation. Of course to attain this complete phase segregated state starting from an initial mixed phase takes a very long time for a large sized system, and has been estimated to be on the microsecond time scale in coarse-grained simulations [35, 36].

To determine physical properties in the global equilibrium state, we would need to run the MD simulation starting from a totally segregated configuration. To make the simulation more efficient, we set the initial partitioning of cholesterol in the two phases consistent with its equilibrium partitioning. This is done by fixing it at the partition coefficient of cholesterol measured in the coarsening regime. To estimate the relative partitioning of cholesterol in the POPC

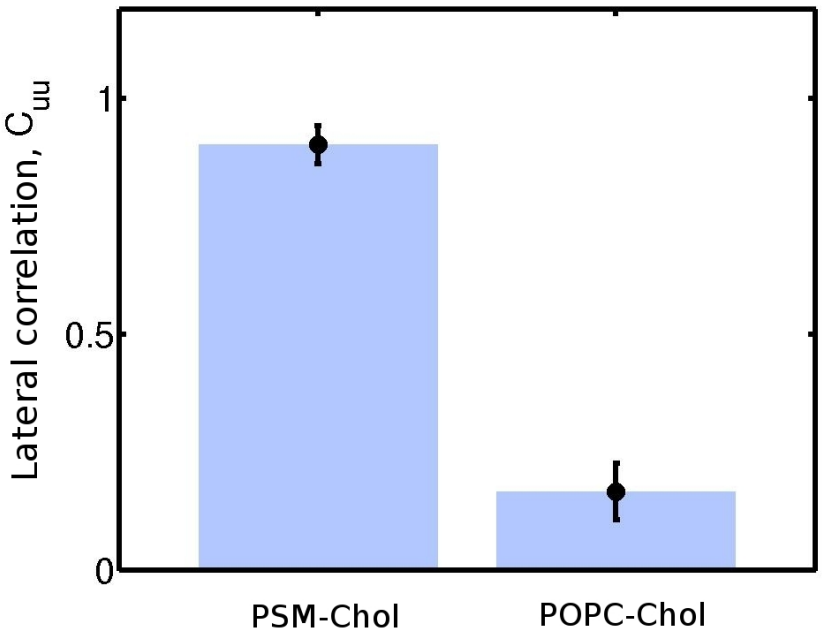

FIGURE 3.5: shows lateral correlation, C_{uu} defined from the correlation $C(\rho^u_{PSM/POPC}(r), \rho^u_{Chol}(r))$ between the density of upper leaflet PSM and Chol and upper leaflet POPC and Chol of the ternary asymmetric bilayer membrane respectively. The value of C_{uu} is small for the POPC and Chol, indicating weak spatial corrlation between the POPC and Chol in the same leaflet whereas, the high value of C_{uu}, suggests the high spatial correlation between the PSM and Chol in the same leaflet of ternary asymmetric bilayer.

and the PSM rich regions in the upper leaflet in the coarsening regime, the joint probability distribution of finding a given concentration of PSM with Chol in an xy region (similarly, POPC with Chol) is calculated and shown in Figure 3.4 (b) and Figure 3.4 (c). These joint probabilities show that the cholesterol concentration completely correlates with the PSM concentration (i.e., Chol is low (high) when the PSM concentration is low (high)) and completely *anticorrelates* with the POPC concentration (i.e., Chol is low (high) when POPC is high (low)), and shows that cholesterol preferentially partitions in the PSM-rich phase three times more than in POPC-rich region (more precisely $2.97:1$).

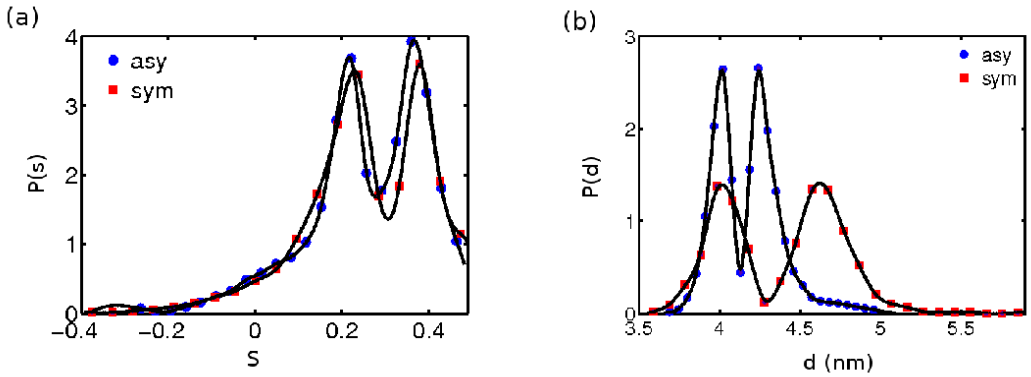

FIGURE 3.6: (a) Probability distribution of the deuterium order parameter S in the asymmetric (blue) and symmetric (red) bilayers following equilibration from the fully segregated configuration. Here S of the selected carbons (C5-C7) of POPC and PSM is displayed, after suitable binning in the xy-plane, with the lower branch $0.1 - 0.26$ corresponding to the low partitioning of PSM in the l_d phase and the higher branch $0.35 - 0.45$ corresponding to its enrichment in the l_o phase. (b) Probability distribution of the bilayer thickness d in the asymmetric (blue) and symmetric (red) bilayers following equilibration from the fully segregated configuration. The two distinct peaks in the asymmetric bilayer at 4 nm and 4.3 nm indicates the coexistence of the l_d and l_o phases. (See Chapter 2).

To study the correlation between the Chol to PSM/POPC in the upper leaflet of the asymmetric bilayer membrane, we define a 'Lateral correlation' from the normalized spatial correlation (r denotes the 2d coordinate (x, y)), $C(\rho^u_{PSM/POPC}(x, y), \rho^u_{Chol}(x, y))$, between the spatial density of the PSM (POPC) of the upper leaflet to that of the Chol with same coordinate (x,y) which is defined as,

$$C(\rho^u_{PSM/POPC}(x,y), \rho^u_{Chol}(x,y)) = \frac{\langle \rho^u_{PMS/POPC}(x,y)\rho^u_{Chol}(x,y)\rangle - \langle \rho^u_{PSM/POPC}(x,y)\rangle\langle \rho^u_{Chol}(x,y)\rangle}{\sqrt{\langle \rho^u_{PSM/POPC}(x,y)^2\rangle - \langle \rho^u_{POPC}(x,y)\rangle^2}\sqrt{\langle \rho^u_{Chol}(x,y)^2\rangle - \langle \rho^u_{Chol}(x,y)\rangle^2}} \tag{3.1}$$

averaged over space (denoted by C_{uu}) and compute for the two pairs, PMS-Chol and POPC-Chol in the upper leaflet of the asymmetric bilayer. Figure

3.5 shows the lateral correlation, C_{uu} for the two pairs, PMS-Chol and POPC-Chol in the upper leaflet of the asymmetric bilayer. The high value of C_{uu} for PSM-Chol in upper leaflet, suggests that there is a high spatial correlation between the PSM and Chol in upper leaflet which brings them together while the small value of C_{uu} for POPC-Chol in upper leaflet, indicates waek correlation between the POPC and Chol in the ternary bilayer membrane.

The totally segregated PSM/POPC configuration with cholesterol partitioned in the ratio $3:1$ was then used as the initial configuration for the MD runs. Following equilibration, we computed a variety of local and global physical quantities over a time scale of 100 ns, as described below. We calculated the deuterium order parameter S for POPC and PSM, which describes the rigidity of the acyl chain. The deuterium order parameter (S) for each lipid was calculated from selected carbon atom positions of the PSM and POPC lipid chains. In our atomistic MD simulations, S is defined for every selected CH_2 group in the chains as, $S \equiv \frac{1}{2}\langle 3\cos^2\theta - 1\rangle$ where θ is the angle between a CH-bond and the normal to the plane of the membrane (z-axis). Since we have used a united atom model description in our simulation, we have to reconstruct the CH-bond from the positions of successive CH_2-groups, assuming tetrahedral geometry of the CH_2-groups. For each molecule, an averaging is done over the two bonds in each CH_2-group. This is then coarse-grained (binned) over a spatial scale of 1.56 nm and time scale of 20 ns. For the present purposes, carbon atoms $5-7$ were selected from each acyl chains (corresponding to palmitoyl-oleoyl chains of POPC, and palmitoyl-sphingomyelin of PSM). This choice of carbon atoms best characterizes the acyl chain rigidity induced by the proximal cholesterol [8]. Using this, the saturated lipid tails of PSM that are in the PSM-enriched domains were found to be more rigid than both the PSM and POPC molecules in the POPC-rich domains. This is reflected in the bimodal distribution of $P(S)$ in Figure 3.6(a). The distinction of the deuterium

order parameter in the two regions indicate that the PSM- and POPC-rich regions may be identified with l_o and l_d phases, respectively. From Figure 3.6(a), it can be seen that the probability distribution of deuterium order parameters in the asymmetric bilayers are comparable to that of symmetric bilayer. These features are replicated in the configurations obtained during coarsening. The probability distribution of S in the coarsening regime is bimodal (Figure 3.7[A]). Further, the segregation of chemical composition is naturally accompanied by an l_o-l_d phase separation, as seen from the spatial variation of S for both asymmetric and symmetric bilayers (Figure 3.8). From this spatial distribution, it is visually apparent that the size of l_o domain size (enriched in PSM) is significantly larger in the symmetric bilayer compared to that of asymmetric bilayer, over the time scale measured.

The bilayer thickness d also shows a variation across the phases, the probability distribution of the local bilayer thickness in the fully equilibrated bilayer is displayed in Figure 3.6(b). As with deuterium order parameter, the distribution of bilayer thickness for both the symmetric and asymmetric bilayers is bimodal, corresponding to the (smaller d) POPC- enriched l_d and (larger d) PSM-enriched l_o domains. It is significant that the difference in the bilayer thickness between the l_o and l_d phases in the symmetric bilayer is consistent with recent AFM studies [37], and is *more than twice compared to asymmetric bilayer*. On probing further, we found that the difference between the mean monolayer thickness in the l_o-l_d domains in the symmetric bilayer (≈ 0.37 nm) is more than that in the asymmetric bilayer (≈ 0.358 nm). Even in the coarsening regime, the probability distribution of d is bimodal Figure 3.7[A]). Further, there is a spatial heterogeneity in the bilayer thickness which follows the l_o-l_d phase segregation (Figure 3.8) consistent with the deuterium order parameter results.

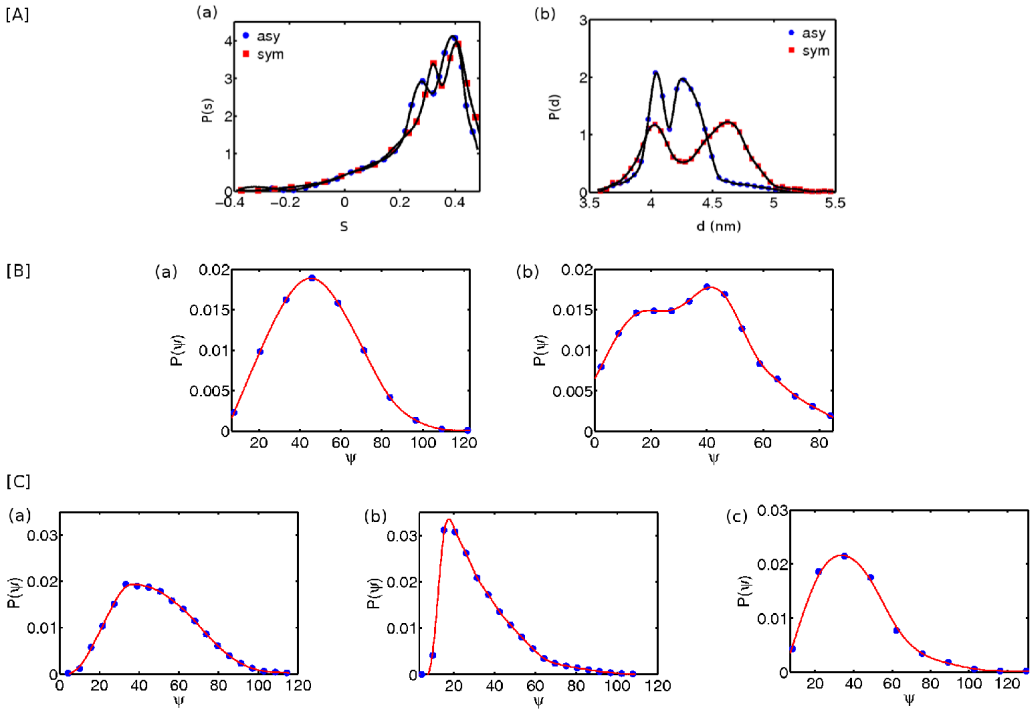

FIGURE 3.7: [A] Probability distribution of the (a) deuterium order parameter S and (b) bilayer thickness d in the asymmetric and symmetric ternary bilayers in the coarsening regime. [B] Probability distribution of splay of POPC in the symmetric bilayer of (a) POPC and (b) POPC-CHOL (with ratio $1:1$). [C] Probability distribution of splay of (a) POPC and (b) PSM in the upper leaflet and (c) POPC in the lower leaflet of the asymmetric ternary bilayer.

3.3.2. Lipid splay and tilt

To quantify the relative packing of lipid chains, the amount of splay between the two lipid tails is calculated, in addition to deuterium order parameter computed above. A tail vector is defined as a vector originating from the carbon of the carbonyl group and pointing to the terminal methyl carbon of a lipid tail. The splay angle ψ is the angle between two such tail vectors of each lipid. The probability distribution, $P(\psi)$, of the splay angle of POPC and PSM is shown in the Figure 3.7. Simulation results show that the extent of the splay angle in PSM lipid tails which are predominantly enriched in the l_o-domain is significantly smaller $(17°)$ than that in POPC lipid tails $(40°)$ which predominantly enrich the l_d-domain. In

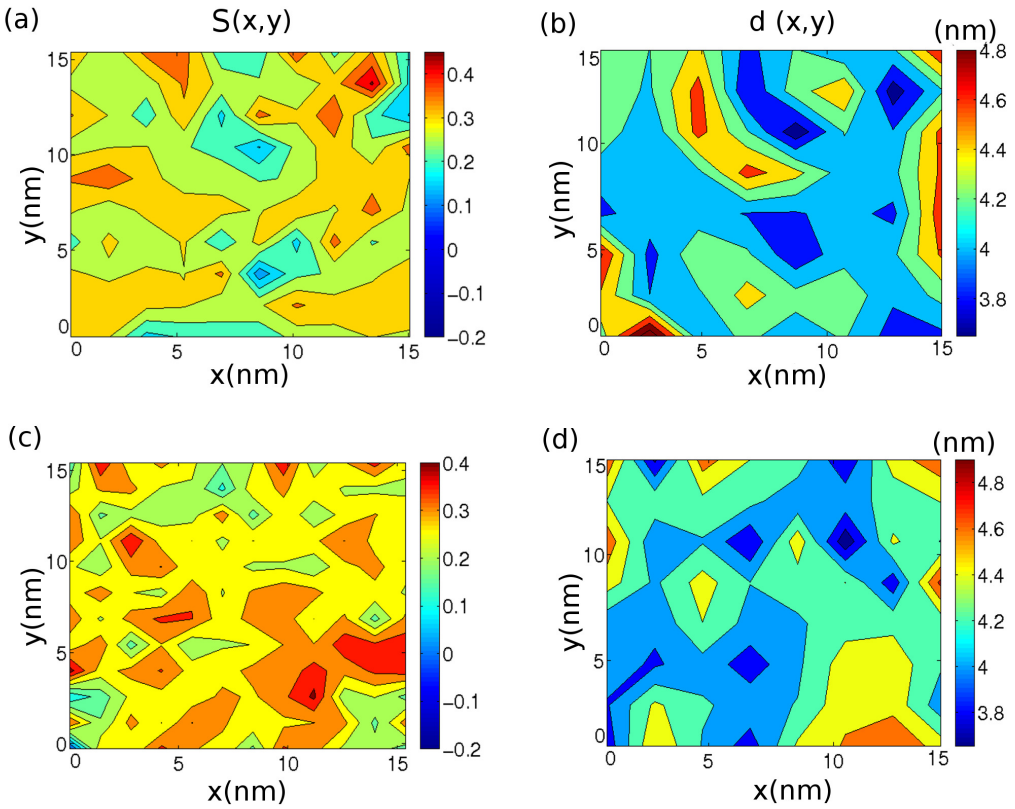

FIGURE 3.8: Spatial variation of deuterium order parameter $S(x, y)$ and bilayer thickness $d(x, y)$ of (a-b) asymmetric bilayer and (c-d) symmetric bilayer of the ternary system in the coarsening regime. The domains appear larger in the symmetric bilayer compared to the asymmetric bilayer, evaluated over the same time.

addition, the extent of lipid splay in the symmetric and asymmetric bilayers is comparable. Taken together with the deuterium order parameter data, the lipid splay results strongly suggest that the packing fraction of lipids in the PSM-rich phase is higher than that in the POPC-rich phase.

Tilt angle of the lipid tail chain is defined as the orientation of the mean tail vector of the lipid with respect to the local outward normal to the membrane, and is described by two angles (θ, ϕ), the polar and azimuthal angles, respectively. The angle ϕ measures the orientation of the 2d tilt vector, the projection of the tail vector onto the tangent plane, with the x-axis. An accurate determination of the tilt angles of the component lipids is quite involved, since, over

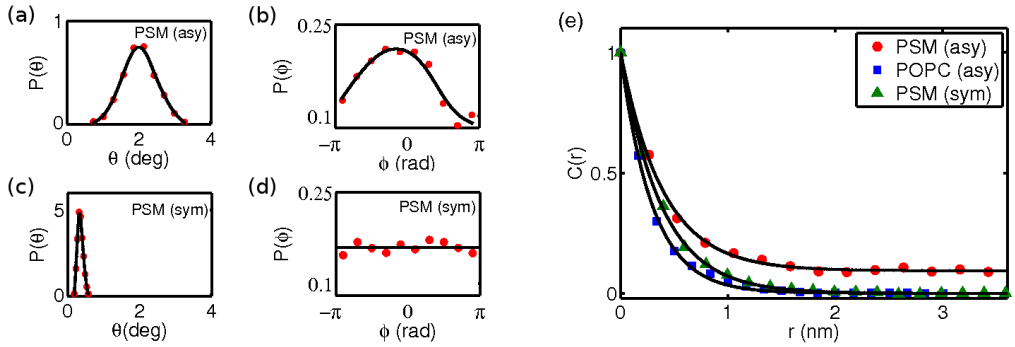

FIGURE 3.9: Probability distribution of the coarse-grained tilt angles θ and ϕ of PSM in (a, b) the asymmetric bilayer, and (c, d) symmetric bilayer, respectively. These data are collected from equilibrium configurations that exhibit complete phase segregation, where the domain size is about half the system size. In the asymmetric ternary bilayer, PSM exhibits a measurable tilt, as evidenced from the distributions of θ and ϕ. In comparison, PSM in the symmetric bilayer shows an absence of tilt – the distribution of θ is peaked at a value close to 0, while the distribution of ϕ is uniform. (e) The tilt correlation function $C(r) \equiv \langle \phi(r)\phi(0) \rangle$, normalized to its value at $r = 0$, shows an exponential decay to zero for POPC (asymmetric bilayer) and PSM (symmetric bilayer). However PSM in the asymmetric bilayer shows an exponential decay to a *nonzero value*, demonstrating long range tilt correlations. The correlation length, defined by the scale at which $C(r)$ decreases to $1/e$ of its value at $r = 0$, can be easily read out, $\xi_{\text{PSM}}(sym) = 0.35\,nm$, $\xi_{\text{PSM}}(asy) = 0.5\,nm$ and $\xi_{\text{POPC}}(asy) = 0.3\,nm$.

short length scales, the local normal to the membrane fluctuates due to molecular protrusion effects. To compute local average tilt, a coarse-graining scale is chosen, which should be more than the protrusion scale and less than the tilt correlation length (which in turn should of course be smaller than the size of the l_o domain). Over this coarse-grained scale, a membrane normal is considered to be along the z-axis. A convenient choice of coarse graining scale is around a $1\,\text{nm}^2$ (which encompasses ≈ 3 lipids on an average), for which statistically reliable results can be obtained. For instance, for POPC-only bilayer, the probability distribution of the coarse-grained angle, $P(\theta)$, is peaked about zero, while the distribution $P(\phi)$ is uniform, consistent with the known fact that POPC does not exhibit a tilt at this temperature [38].

We have used the above procedure to study the local tilt angle distribution of the lipids in the equilibrium phase segregated configurations of the ternary

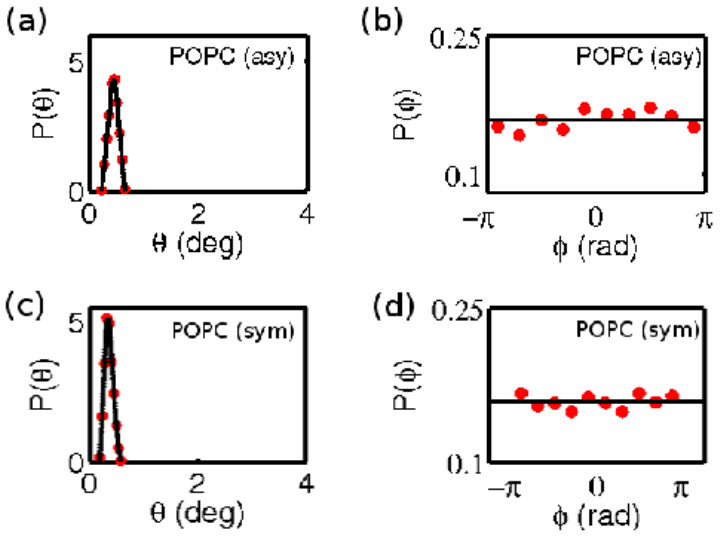

FIGURE 3.10: Probability distribution of the tilt angles (a) θ and (b) ϕ for POPC in the asymmetric ternary bilayer. (c)&(d) are the same for the symmetric ternary bilayer. Note that the distribution of θ is peaked about ≈ 0, while the distribution of ϕ is uniform, consistent with the known fact that POPC does not exhibit a tilt at these temperatures [38].

system. The tilt angle distribution of POPC lipids in the symmetric and asymmetric ternary bilayers has a similar distribution as in the case of POPC-only bilayer as seen in Figure 3.10. On the other hand, the tilt angle distribution for PSM shows an interesting trend. While PSM in the symmetric bilayer shows no evidence of tilt ($P(\theta)$ is peaked at around 0° and $P(\phi)$ is uniform), PSM in the PSM-rich (l_o) domain of the asymmetric bilayer has a nonzero tilt of around $2.016 \pm 0.69^\circ$. This small tilt of PSM in the asymmetric bilayer is consistent with the decrease in bilayer thickness of the asymmetric membrane compared to that of symmetric bilayer (see Figure 3.6(b)). Tilt angle correlations defined as $C(r) = \langle \phi(r)\phi(0) \rangle$ are computed for POPC and PSM lipid molecules and the results are shown in Figure 3.9. The correlation functions of the tilt of POPC and PSM (symmetric bilayer) decay exponentially to zero, consistent with the above findings. However, $C(r)$ for PSM in the asymmetric bilayer decays exponentially to a non zero value, signaling long range order [39] in PSM molecules

in the asymmetric bilayer. This suggests that the asymmetric nature of the bilayer can potentially generate a tilt ordering of PSM molecules in the PSM-rich (l_o) domain.

Previous simulations [8, 36, 40] and experiments [5, 37, 41–44] have shown that the thickness of l_o domains is larger than that of l_d domain. This difference in thickness between l_o and l_d domains gives rise to line tension along the domain boundary [42]. The lipid tails of the l_o domain can be exposed to solvent as a result of such mismatch, which is energetically unfavourable. One of the ways to mitigate such mismatch is for the thicker l_o domain to undergo a small tilt such that the head groups of the two domains can be at the same height. The observed small tilt in the simulations of asymmetric bilayers supports this hypothesis and is consistent with our observation of the smaller monolayer thickness difference of the asymmetric bilayer reported above. Within a Landau theory, the asymmetric bilayer can be thought of as being subjected to a transverse compression, which would naturally lead to a tilt when the lipids are stretched out (as they are in the l_o domain) [45, 46]. This was however done in the context of a symmetric bilayer. In order to study the asymmetric bilayer within such a framework, one needs to work with monolayer thicknesses, ψ_+, ψ_-. There is a natural coupling of the gradients of ψ_+, ψ_- to the local tilt, $\mathbf{m}_+, \mathbf{m}_-$, that enters the Landau free energy functional as $A\left(\mathbf{m}_+ \cdot \nabla\psi_+\right)^2$. If the coefficient $A > 0$, then this will imply that larger spatial variations in the thickness ψ will be accompanied by small (or no) tilt, whereas smaller spatial variations in thickness will be accompanied by larger tilt. This is consistent with our computations of the tilt and the thickness variation of the monolayers in the asymmetric and symmetric systems.

The existence of a finite tilt and its correlation over long scales, if verified experimentally [47], could have important consequences for membrane deformation and budding [48]. The tilt vector naturally couples to the local curvature tensor of the membrane, giving rise to anisotropic bending stresses. If

the constituent molecules are chiral (as they usually are), then there are additional bending stresses coming from chiral couplings of the tilt and curvature. If strong enough, these bending stresses can induce membrane deformation giving rise to spherical buds or cylindrical tubules [42, 48].

3.3.3. Tagged particle diffusion

We have also studied transport quantities such as tagged particle diffusion of the component molecules in the fully segregated equilibrium ternary system. The mean square displacement (MSD) is defined as $\langle \delta r_i(t)^2 \rangle$ of a tagged particle, where $\delta r_i(t) = r_i(t) - r_i(0)$ is the displacement of tagged i^{th} lipid of a given species at time t from its position at $t = 0$. One way to analyze the MSD is to fit it to $\langle \delta r_i(t)^2 \rangle \propto t^{\alpha}$, where α close to 1 could be interpreted as simple diffusion and $\alpha \ll 1$ as sub-diffusion. The values of α obtained from fits to the POPC and PSM data taken over a large equilibrium phase segregated domain in (as)symmetric bilayers are close to 1 and suggest a dynamics close to simple diffusion (Figure 3.11 a).

However recent single particle tracking experiments of labeled molecules on the cell surface show *marked* deviations from simple diffusion. A variety of explanations have been invoked to explain these data and include molecular crowding and the presence of an actin skeleton fence. Another explanation stems from the lack of evidence for large scale lipid rafts at the cell surface, and have prompted investigators to suggest that the sub-resolution lipid domains which are in a process of slow coarsening could be responsible for the slowing down of single-particle transport. This is the motivation to study tagged particle diffusion of component molecules in the coarsening regime.

It should be noted that even though the membrane composition forms well defined domains during the process of coarsening, the individual component molecules can traverse across domains. The dynamics of 'tagged' component

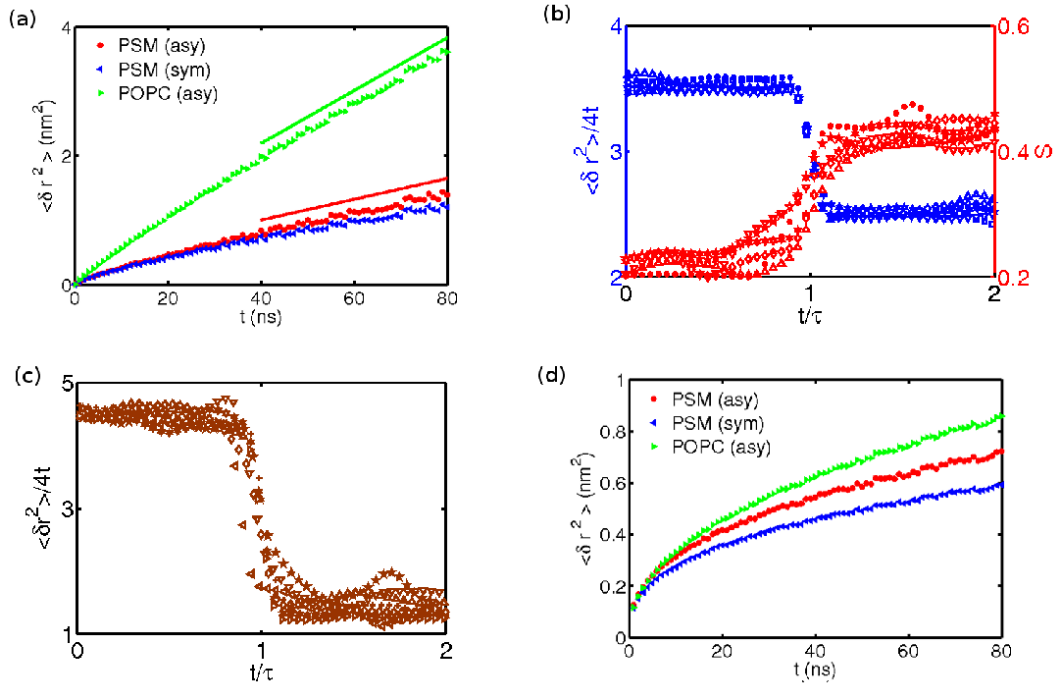

FIGURE 3.11: Mean square displacement (MSD) of tagged particles as a function of time collected at high resolution in the ternary bilayer. (a) For the fully segregated equilibrium configuration, the computed MSD vs time data has been fit to $\langle \delta r_i(t)^2 \rangle \propto t^\alpha$: in the asymmetric bilayer $\alpha_{POPC} = 0.89 \pm 0.04$ and $\alpha_{PSM} = 0.82 \pm 0.08$, while in the symmetric bilayer $\alpha_{POPC} = 0.79 \pm 0.03$ and $\alpha_{PSM} = 0.77 \pm 0.02$. Data collected over 80 ns. This analysis shows that the MSD of tagged molecules in large phase segregated domains at equilibrium is close to simple diffusion (lines drawn for comparison). (b-c) MSD of tagged particles collected at high resolution over short time scales during coarsening in the ternary asymmetric bilayer. Tagged particle diffusion of (b) PSM and (c) Chol in the upper leaflet – statistics collected over 6 tagged particles, each starting from the l_d domain, shows a data collapse onto a nonlinear crossover scaling curve. The crossover from high to low diffusion occurs at a time τ, computed as the first-passage time of the tagged particle. For PSM, we find that $D_0 = 3.49\mu$m^{2}s^{-1} and $D_\infty = 2.69\mu$m^{2}s^{-1}, while for Chol, $D_0 = 4.23\mu$m^{2}s^{-1} and $D_\infty = 1.36\mu$m^{2}s^{-1}. Note that in (b) as PSM moves across domains, the deuterium order parameter S of tagged PSM shows a similar crossover, going from ~ 0.22 (l_d) to ~ 0.42 (l_o). (d) MSD versus time with fits to $\langle \delta r_i(t)^2 \rangle \propto t^\alpha$, for PSM in the asymmetric ($\alpha = 0.39 \pm 0.03$) and symmetric bilayers ($\alpha = 0.35 \pm 0.02$), and POPC and Chol in the upper leaflet of the asymmetric bilayer ($\alpha = 0.45 \pm 0.01$ and 0.41 ± 0.03, respectively), all in the coarsening regime. Note that the α exponent for PSM in the symmetric bilayer is smaller than the asymmetric bilayer, due to the transbilayer coupling. Likewise, the MSD for POPC and Chol in the symmetric ternary bilayer are shown in Figure 3.12, for comparison.

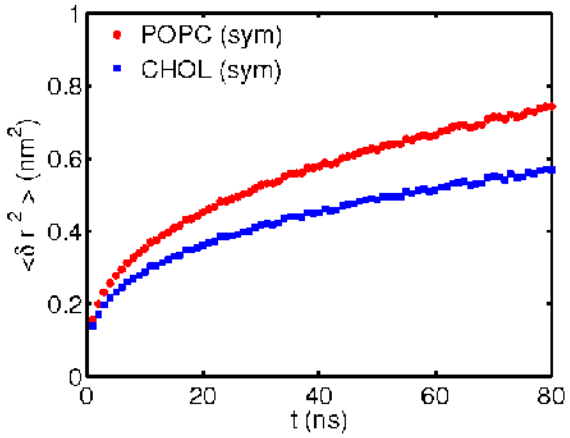

FIGURE 3.12: MSD versus time for tagged POPC and Chol in the symmetric ternary bilayer evaluated in the coarsening regime. Fits to $\langle \delta r(t)^2 \rangle \propto t^{\alpha}$ gives $\alpha = 0.35 \pm 0.02$ (POPC) and $\alpha = 0.32 \pm 0.03$ (Chol). Note that the values of α are consistently lower than those in the asymmetric ternary bilayer.

lipids can be monitored by measuring their diffusion coefficients and correlating them with the physical and chemical heterogeneity across the membrane. While computing the MSD, the location of the tagged lipid, whether it is in the POPC-rich (l_d) or PSM-rich (l_o) domain, is monitored by computing the instantaneous deuterium order parameter S of the tagged lipid and the local bilayer thickness. The diffusion analysis is shown in Figure 3.11. It can be seen that the diffusion coefficient of both PSM and Chol molecules, given by the value of $\langle \delta r_i^2(t) \rangle / 4t$ where it is constant, is different depending on whether the tagged lipid molecule is in the l_o and l_d domain as has been reported in other simulation studies[36].

Note that only a fraction of tagged molecules will be seen traversing across the domain boundary when measured over a fixed time interval. In the coarsening regime, where the domain sizes are small, this fraction is appreciable. When the tagged PSM or Chol molecules that initially lie in the POPC-rich (l_d) domain cross over to the l_o domain, the local diffusion coefficient crosses over from an early time high value (D_0) to a late time low value (D_∞). For each of the

tagged components, a first-passage time, defined as the first time that a tagged molecule residing in a domain moves out of it, is computed. The crossover time τ for each tagged particle is then obtained from such a computed first-passage time. Note that the first passage time, and hence the crossover time, depends on the trajectory of the tagged particle and is therefore a stochastic quantity. Further, the crossover MSD data is collected only for those molecules which cross the domain boundary exactly once.

The MSD is found to obey a crossover scaling relation,

$$\langle \delta r^2 \rangle = 4 D_0 t F\left(t/\tau\right) \tag{3.2}$$

where the nonlinear scaling function F has the asymptotic form,

$$\begin{aligned} F\left(t/\tau\right) &= 1 \qquad \text{for} \quad t/\tau \ll 1 \\ &= \frac{D_\infty}{D_0} \quad \text{for} \quad t/\tau \gg 1 \end{aligned} \tag{3.3}$$

The data collapse shown in Figure 3.11(b) and 3.11(c) demonstrate this crossover scaling for PSM and Chol molecules, respectively. Experimentally the crossover time scale τ can be obtained from the value of t at which the instantaneous $D(t) = \left(D_0 + D_\infty\right)/2$, rather than the first-passage time. The values of the diffusion coefficients for PSM molecules (Figure 3.11(b)) are in agreement with the experimental findings [49, 50], while the values for Chol molecules (Figure 3.11(b)) are slightly lower than those reported in other simulations [36]. This discrepancy can be attributed to the differences in lipid composition of the ternary bilayer used in both the simulations. The difference in the tagged particle diffusion coefficient between the two domains can be attributed to changes in local viscosity (η), moment-of-inertia (I) of the particle

and to changes in the local density correlations (given by the local partial structure factors, $S_{\alpha\beta}(q)$) with neighbouring molecules that the tagged particle experiences as it traverses across the domain. The change in the deuterium order parameter S is used to track the changes in moment-of-inertia of the tagged molecules. For PSM molecules, this shows a crossover similar to the crossover diffusion, with the value of S being low (high) when the diffusion coefficient is high (low) as seen in Figure 3.11(b). On the other hand cholesterol being a rigid molecule is unlikely to undergo any conformational change, resulting change in moment-of-inertia, as it traverses across the domains. Thus a substantial change in the diffusion coefficient of Chol molecules can be attributed to the changes in viscosity and local density correlations, $S_{\alpha\beta}(q)$, arising from changes in the local environment.

In the context of SPT experiments, if the time scale over which the tagged particle is tracked is large enough so that the particle crosses and recrosses the domains, then one would measure the MSD of $\delta r_i(t) = \int dt' \, (r_i(t'+t) - r_i(t'))$. For the control pure POPC symmetric bilayer, it is seen that the trajectories are purely diffusive ($\langle \delta r_i(t)^2 \rangle \propto t$) in nature. For the ternary bilayer, however, this MSD would exhibit deviations from true diffusion, which can be characterized by $\langle \delta r_i(t)^2 \rangle \propto t^\alpha$. Figure 3.11(d) shows the MSD for the tagged lipids in both the symmetric and asymmetric bilayers and the corresponding values of the exponent α. The value of α obtained for PSM in the asymmetric bilayer ($\alpha \approx 0.39$) is consistent with the experimental value obtained by analyzing recent SPT of labeled PSM on the plasma membrane of epithelial cells, $\alpha \approx 0.3$ [31]. The interbilayer coupling in the symmetric ternary system, makes the tagged PSM movement slower, as seen by the lower value of $\alpha \approx 0.35$ (see Figure 3.11(d)). The tagged particle dynamics of the other lipids in the asymmetric bilayer, viz., POPC and cholesterol, show interesting differences between the two leaflets – typically, the upper leaflet lipids show a smaller α ($\alpha = 0.45, 0.41$, respectively), than the lower leaflet lipids ($\alpha = 0.85, 0.89$, respectively). Note that we expect

that this analogous behavior is a finite time effect, asymptotically the motion of tagged molecules will be diffusive.

3.4. Conclusion and future direction

The cell membrane exhibits both lateral and transverse heterogeneity. In this chapter, the equilibrium properties of a ternary component asymmetric bilayer membrane system at l_o-l_d phase coexistence are studied using an atomistic MD simulation over a time scale of 220 ns. The asymmetric bilayer considered in this study is composed of POPC, PSM and cholesterol in the ratio of $1:1:1$ in the upper leaflet and POPC and cholesterol in the lower leaflet. The two significant results from this study are: (i) cholesterol prefers to be associated with PSM-rich domains (l_o) three times more than in POPC-rich domains (l_d) and (ii) the saturated lipid PSM in the l_o domain exhibits long-range tilt correlations purely as a result of the asymmetry in the bilayer composition (in contrast, the PSM lipid molecules in the symmetric bilayer show no such tilt).

This bilayer-asymmetry induced lipid tilt in the l_o domain has important implications to local membrane deformation and hence membrane budding and endocytosis. The existence of a lipid tilt expressed over large scales provides a natural coupling to the local curvature tensor, and results in anisotropic bending stresses at the membrane [48]. Moreover, if the constituent lipids are chiral (as they are in 'raft'-lipids), then there would be additional bending stresses serving to deform the membrane locally. When the strength of these couplings are large enough, they can induce the local formation of spherical buds or cylindrical tubules. Recent FRET-based studies of the organization of lipid tethered proteins on the outer surface of living cells, such as GPI-anchored proteins, have shown that they form cholesterol sensitive nanoclusters mediated by the activity of cortical actin [51, 52]. These studies imply that there must exist a

molecular linkage between the outer leaflet GPI-anchored proteins and cortical actin. The current study will form the basis for further investigations on possible transbilayer interactions between GPI-anchored proteins, PSM and cholesterol, with specific saturated, long chain lipids at the inner leaflet that have potential interactions with actin or actin remodeling proteins.

References

[1] P. F Devaux and R Morris. Transmembrane asymmetry and lateral domains in biological membranes. *Traffic*, 5:241–6, 2004.

[2] Daniel Lingwood and Kai Simons. Lipid rafts as a membrane-organizing principle. *Science*, 327:46–50, 2010.

[3] K Simons and E Ikonen. Functional rafts in cell membranes. *Nature*, 387:569–72, 1997.

[4] M. D Collins and S. L Keller. Tuning lipid mixtures to induce or suppress domain formation across leaflets of unsupported asymmetric bilayers. *Proc. Natl. Acad. Sci. U.S.A.*, 105:124–128, 2007.

[5] Sarah L Veatch and Sarah L. Keller. Organization in lipid membranes containing cholesterol. *Phys. Rev. Lett.*, 89:268101, Dec 2002.

[6] Sarah L. Veatch and Sarah L. Keller. Separation of liquid phases in giant vesicles of ternary mixtures of phospholipids and cholesterol. *Biophys J.*, 85(5):3074–83, 2003.

[7] T Baumgart, S.T Hess, and WW Webb. Imaging coexisting fluid domains in biomembrane models coupling curvature and line tension. *Nature*, 425(6960):821–4, 2003.

[8] Perttu S Niemelä, Samuli Ollila, Marja T Hyvnen, Mikko Karttunen, and Ilpo Vattulainen. Assessing the nature of lipid raft membranes. *PLoS Comput Biol.*, 3(2):e34, 2007.

[9] Jussi Aittoniemi, Perttu S. Niemel, Marja T. Hyvnen, Mikko Karttunen, and Ilpo Vattulainen. Insight into the putative specific interactions between cholesterol, sphingomyelin, and palmitoyl-oleoyl phosphatidylcholine. *Biophys J.*, 92(4):1125–1137, 2007.

[10] Santi Esteban-Martín, H. Jelger Risselada, Jesús Salgado, and Siewert J. Marrink. Stability of asymmetric lipid bilayers assessed by molecular dynamics simulations. *J. Am. Chem. Soc.*, 131 (42):15194–202, 2009.

[11] Andrey A. Gurtovenko and Ilpo Vattulainen. Lipid transmembrane asymmetry and intrinsic membrane potential:two sides of the same coin. *J. Am. Chem. Soc.*, 129 (17):5358–5359, 2007.

[12] Andrey A. Gurtovenko and Ilpo Vattulainen. Membrane potential and electrostatics of phospholipid bilayers with asymmetric transmembrane distribution of anionic lipids. *J. Phys. Chem. B*, 112 (15):4629–34, 2008.

[13] Mohamed Laradji and P. B. Sunil Kumar. Anomalously slow domain growth in fluid membranes with asymmetric transbilayer lipid distribution. *Phys. Rev. E*, 73:040901, Apr 2006.

[14] Jason D. Perlmutter and Jonathan N. Sachs. Interleaflet interaction and asymmetry in phase separated lipid bilayers: Molecular dynamics simulations. *J. Am. Chem. Soc.*, 133 (17):6563–6577, 2011.

[15] AJ Wagner, S Loew, and S May. Influence of monolayer-monolayer coupling on the phase behavior of a fluid lipid bilayer. *Biophys J.*, 93(12):4268–77, 2007.

[16] D. W. Allender and M. Schick. Phase separation in bilayer lipid membranes: Effects on the inner leaf due to coupling to the outer leaf. *Biophys J.*, 91(8):2928–35, 2006.

[17] J Elizabeth, Wallace, Nigel M. Hooper, and Peter D. Olmsted. The kinetics of phase separation in asymmetric membranes. *Biophys J.*, 88(6):4072–83, 2005.

[18] J Elizabeth, Wallace, Nigel M. Hooper, and Peter D. Olmsted. The kinetics of phase separation in asymmetric membranes. *Biophys J.*, 88(6):4072–83, 2005.

[19] Per Lyngs Hansen, Ling Miao, and John Hjort Ipsen. Fluid lipid bilayers: Intermonolayer coupling and its thermodynamic manifestations. *Phys. Rev. E*, 58:2311–2324, Aug 1998.

[20] O Berger, O Edholm, and F Jhnig. Molecular dynamics simulations of a fluid bilayer of dipalmitoylphosphatidylcholine at full hydration, constant pressure, and constant temperature. *Biophys J.*, 72(5):2002–13, 1997.

[21] Egbert Egberts, Siewert-Jan Marrink, and Herman J. C. Berendsen. Molecular dynamics simulation of a phospholipid membrane. *European Biophysics Journal*, 22:423–36, 1994.

[22] DP Tieleman, LR Forrest, MS Sansom, and HJ Berendsen. Lipid properties and the orientation of aromatic residues in ompf, influenza m2, and alamethicin systems: molecular dynamics simulations. *Biochemistry*, 37(50):17554–61, 1998.

[23] Monika Höltje, Thomas Förster, Birte Brandt, Thomas Engels, Wolfgang von Rybinski, and Hans-Dieter Höltje. Molecular dynamics simulations of stratum corneum lipid models: fatty acids and cholesterol. *Biochim Biophys Acta*, 1511:156–67, 2001.

[24] P Niemelä, MT Hyvönen, and I Vattulainen. Structure and dynamics of sphingomyelin bilayer: insight gained through systematic comparison to phosphatidylcholine. *Biophys J.*, 87(5):2976–89, 2004.

[25] G. A Khelashvili and H. L Scott. Combined monte carlo and molecular dynamics simulation of hydrated 18:0 sphingomyelin-cholesterol lipid bilayers. *J Chem Phys*, 120(20):9841–7, 2004.

[26] H Ohvo-Rekilä, B Ramstedt, P Leppimäki, and JP Slotte. Cholesterol interactions with phospholipids in membranes. *Prog Lipid Res.*, 41(1):66–97, 2002.

[27] T Róg and M Pasenkiewicz-Gierula. Cholesterol-sphingomyelin interactions: a molecular dynamics simulation study. *Biophys J.*, 91(10):3756–67, 2006.

[28] Z Zhang, SY Bhide, and ML Berkowitz. Molecular dynamics simulations of bilayers containing mixtures of sphingomyelin with cholesterol and phosphatidylcholine with cholesterol. *J Phys Chem B.*, 111(44):12888–97, 2007.

[29] Shreyas Y. Bhide, Zhancheng Zhang, , and Max L. Berkowitz. Molecular dynamics simulations of sops and sphingomyelin bilayers containing cholesterol. *Biophys J.*, 92(4):1284–1295, 2007.

[30] A Kusumi, C Nakada, K Ritchie, K Murase, K Suzuki, H Murakoshi, RS Kasai, J Kondo, and T Fujiwara. Paradigm shift of the plasma membrane concept from the two-dimensional continuum fluid to the partitioned fluid: high-speed single-molecule tracking of membrane molecules. *Annu Rev Biophys Biomol Struct.*, 34:351–78, 2005.

[31] Steffen J. Sahl, Marcel Leutenegger, Michael Hilbert, Stefan W. Hell, and Christian Eggeling. Fast molecular tracking maps nanoscale dynamics of

plasma membrane lipids. *Proc. Natl. Acad. Sci. USA*, 107:6829–6834, 2009.

[32] Michael Patra. Lateral pressure profiles in cholesteroldppc bilayers. *Eur. Biophys. J.*, 35:79–88, 2005.

[33] Samuel A. Safran. *Statistical Thermodynamics of Surfaces, Interfaces, and Membranes*. Addison-Wesley, 1994.

[34] A J Bray. Theory of phase-ordering kinetics. *Advances in Physics*, 43:357–459, 1994.

[35] Sagar A. Pandit, Eric Jakobsson, and H. L. Scott. Simulation of the early stages of nano-domain formation in mixed bilayers of sphingomyelin, cholesterol, and dioleylphosphatidylcholine. *Biophys J.*, 87(5):3312–3322, 2004.

[36] H. Jelger Risselada and Siewert J. Marrink. The molecular face of lipid rafts in model membranes. *Proc. Natl. Acad. Sci. U.S.A.*, 105:17367–17372, 2008.

[37] HA Rinia, MM Snel, JP van der Eerden, and B de Kruijff. Visualizing detergent resistant domains in model membranes with atomic force microscopy. *FEBS Lett.*, 501(1):92–6, 2001.

[38] Jianjun Pan, Thalia T Mills, Stephanie Tristram-Nagle, and John F Nagle. Cholesterol perturbs lipid bilayers nonuniversally. *Phys. Rev. Lett.*, 100:198103, May 2008.

[39] P. M. Chaikin and T. C. Lubensky. *Principles of Condensed Matter Physics*. Cambridge University Press, 2000.

[40] Lars V. Schäfer, Djurre H. de Jong, Andrea Holt, Andrzej J. Rzepiela, Alex H. de Vries, Bert Poolman, J. Antoinette Killian, and Siewert J. Marrink. Lipid packing drives the segregation of transmembrane helices into

disordered lipid domains in model membranes. *Proc. Natl. Acad. Sci. U.S.A.*, 108:1343–8, 2010.

[41] D.A Brown and E London. Structure and function of sphingolipid- and cholesterol-rich membrane rafts. *J Biol Chem.*, 275(23):17221–4, 2000.

[42] AJ García-Sáez, S Chiantia, and P Schwille. Effect of line tension on the lateral organization of lipid membranes. *J Biol Chem.*, 282:33537–33544, 2007.

[43] DE Saslowsky, J Lawrence, X Ren, DA Brown, RM Henderson, and JM Edwardson. Placental alkaline phosphatase is efficiently targeted to rafts in supported lipid bilayers. *J Biol Chem.*, 277(30):26966–70, 2002.

[44] Smita P. Soni, Daniel S. LoCascio, Yidong Liu, Justin A. Williams, Robert Bittman, William Stillwell, and Stephen R. Wassall. Docosahexaenoic acid enhances segregation of lipids between raft and nonraft domains: 2h-nmr study. *Biophys J.*, 95(1):203–214, 2008.

[45] Md. Arif Kamal, Antara Pal, V. A. Raghunathan, and Madan Rao. Theory of the asymmetric ripple phase in achiral lipid membranes. *EPL*, 95:48004, 2011.

[46] Md. Arif Kamal, Antara Pal, V. A Raghunathan, and Madan Rao. Phase behavior of two-component lipid membranes: Theory and experiments. *Phys. Rev. E*, 85:051701, May 2012.

[47] E. B. Watkins, C. E. Miller, J. Majewski, and T. L. Kuhl. Membrane texture induced by specific protein binding and receptor clustering: active roles for lipids in cellular function. *Proc Natl Acad Sci U S A.*, 108(17):6975–6980, 2011.

[48] RC Sarasij, S Mayor, and M Rao. Chirality-induced budding: a raft-mediated mechanism for endocytosis and morphology of caveolae? *Biophys J.*, 92(9):3140–58, 2007.

[49] G Lindblom, G Ordd, and A Filippov. Lipid lateral diffusion in bilayers with phosphatidylcholine, sphingomyelin and cholesterol. an nmr study of dynamics and lateral phase separation. *Chem Phys Lipids.*, 141(1-2):179–84, 2006.

[50] A Pralle, P Keller, EL Florin, K Simons, and JK Hörber. Sphingolipid-cholesterol rafts diffuse as small entities in the plasma membrane of mammalian cells. *J Cell Biol.*, 148(5):997–1008, 2000.

[51] Debanjan Goswami, Kripa Gowrishankar, Sameera Bilgrami, Subhasri Ghosh, Riya Raghupathy, Rahul Chadda, Ram Vishwakarma, Madan Rao, and Satyajit Mayor. Nanoclusters of gpi-anchored proteins are formed by cortical actin-driven activity. *Cell*, 135:1085–97, 2008.

[52] P Sharma, R Varma, RC Sarasij, Ira, K Gousset, G Krishnamoorthy, M Rao, and S Mayor. Nanoscale organization of multiple gpi-anchored proteins in living cell membranes. *Cell*, 116(4):577–89, 2004.

4

Bilayer registry in a multicomponent asymmetric membrane : dependence on lipid composition and chain length

4.1. Introduction

Cell membranes are composed of many different lipid species and exhibit both lateral heterogeneity [1–3] and bilayer asymmetry in their lipid composition [4]. While there have been many in-vitro studies of lateral phase segregation in multicomponent giant unilamellar vesicles (GUVs) [5–7] and suspended membranes [6, 7], it is only recently that attention has turned to membranes with

asymmetric bilayers [8, 9]. One of the issues highlighted in these experiments and relevant to cell membrane biology, is the extent of correlation or registry of phase segregated domains in the two leaflets of the bilayer. This has inspired theoretical [10, 11] and coarse-grained computer simulation [12] studies of *bilayer registry* of domains in asymmetric bilayers. A well studied multicomponent model system is the 3-component lipid mixture comprising an unsaturated lipid (POPC), a saturated lipid (PSM) and cholesterol (Chol) which exhibits liquid-ordered (l_o) - liquid-disordered (l_d) phase coexistence. Since the extent of bilayer registry is likely to be sensitive to lipid chemistry, in this chapter, we study the transbilayer coupling and extent of bilayer registry of the phase domains across the membrane, using an atomistic molecular dynamics (MD) simulation of an asymmetric lipid bilayer membrane comprising POPC/PSM/Chol.

The registry of lipids across the bilayer suggest a mechanism by which outer leaflet lipids may couple with inner leaflet lipids and vice versa. Our motivation for this work comes from a series of experiments that study the spatial organization and dynamics of GPI-APs, on the surface of living cells, as mentioned in the Introduction 1. A variety of experimental strategies such as Fluorescence Resonance Energy Transfer (FRET) [4, 13–16], near-field microscopy (NSOM) and electron microscopy, have revealed that both the organization and dynamics of the outer-leaflet GPI-APs are regulated by cholesterol, sphingolipids and *cortical actin and myosin* at the inner leaflet. The question is how do the outer-leaflet GPI-APs couple to cortical actin that abuts the inner leaflet of the cell membrane [13, 14]. Since the interaction across the bilayer must be indirect, are there other lipids, such as cholesterol and sphingolipids, that are involved in this linkage ? Do specific inner leaflet lipids that interact with actin, participate in this transbilayer coupling [14] ? This naturally brings up the issue of bilayer registry in the cell membrane and its dependence on the specificity of lipids and its chemistry. Here, we address this important issue using atomistic

MD simulation of multicomponent model membranes.

The chapter is organized as follows : We first describe the details of the multicomponent bilayer membrane. In Section 4.3, we present our results on lateral compositional heterogeneity, extent of bilayer registry and mismatch area across the bilayer, as a function of the concentration of the saturated lipid (PSM). We also study how changes in lipid chain length of SM affect bilayer registry. We end with a short summary of the results and conclusions.

4.2. Model membrane

We study the phase segregation and bilayer registry of a symmetric and asymmetric 3-component bilayer membrane embedded in an aqueous medium. We prepare the bilayer membrane at 23°C at different relative concentrations of palmitoyl-oleoyl-phosphatidyl-choline (POPC), long chain palmitoyl-sphingomyelin (SM-16:0) (PSM) and cholesterol (Chol). All multicomponent bilayer membranes have 512 lipids in each leaflet (with a total 1024 lipids) and 32768 water molecules (such that the ratio of water to lipid is $32 : 1$) so as to completely hydrate the simulated lipid bilayer.

For the symmetric bilayer, the relative concentration (in percentage, x) of PSM and Chol in the upper and lower leaflet is varied from $x\,(in\,\%) = 33.3$, 19.9, 12.5, 10.0, 9.1, 7.1, 5.8, 2 and 1%, with POPC contributing to the rest of the lipid content.

For the asymmetric bilayer, the upper leaflet has POPC /PSM /Chol in the ratio $1 : 1 : 1$ (i.e., the relative concentration of each component is 33%). We vary the relative composition in the lower leaflet; denoting x as the relative concentration (in percentage) of PSM and Chol in the lower leaflet, we run through the values $x\,(in\,\%) = 33.3$, 25.0, 19.9, 14.3, 12.5, 10.0, 9.1, 7.1, 5.9 and 4.5%, with POPC contributing to the rest of the lipid content. With this choice of compositions and temperature, the upper leaflet is in the putative l_o-l_d phase

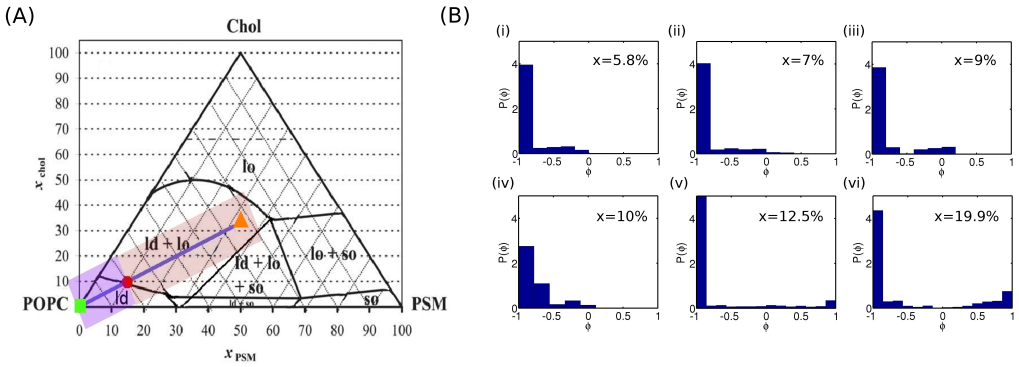

FIGURE 4.1: (A) Ternary phase diagram of POPC, PSM and CHOL at $T = 23°$C taken from Ref. [17]. Triangle (orange) represents the composition $1 : 1 : 1$ which is deep in the phase coexistence region; Dot (red) is a point on the phase boundary $x_c = 10\%$. (B) We have verified this phase diagram by doing simulations at different compositions along the blue line in (A). Panel shows the probability distribution of the phase segregation order parameter ϕ (main text) for the symmetric bilayer at different values of x : (i) - (iii) shows that for $x < 10\%$, the bilayer is in the l_d phase, while (v) - (vi) shows that for $x > 10\%$, the membrane is at l_o-l_d coexistence. The phase transition is clearly at (iv) $x_c = 10\%$.

coexistence regime (see Figure 4.1A, for the ternary phase diagram at $23°$C, taken from Ref. [17]), while in the lower leaflet the compositions straddle the phase boundary allowing us to go from the l_o-l_d phase coexistence regime to the l_d phase, Figure 4.2A.

To study the role of lipid chemistry, we repeat the above set of simulations with PSM in the lower leaflet replaced by the short chain sphingomyelin, SM-14:0 (MSM). We vary the concentration x of MSM (Chol) across the range $x\,(in\,\%) = 4.5$, 5.9, 7.1, 9.1, 10.0, 12.5 and 14.35%.

The details of the MD simulation of the bilayer membrane are given in Chapter 2.

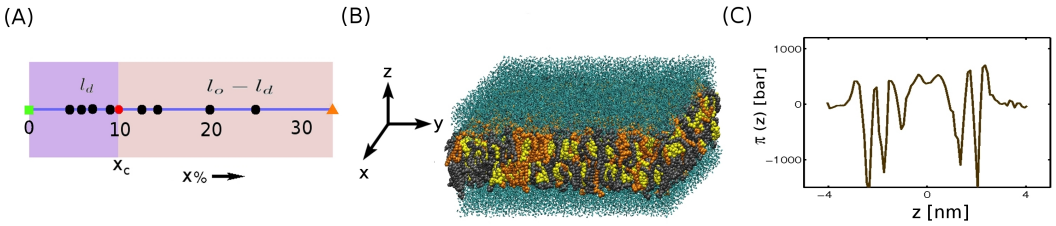

FIGURE 4.2: (A) For the simulations of the asymmetric bilayer, we hold the composition of the upper leaflet at $1:1:1$, while in the lower leaflet the composition of PSM and Chol is varied from $x = 33.3\%$ (orange dot) to 0% (green square), with POPC contributing to the rest. The composition where the simulations are carried out, denoted by black dots (see *Methods*), are indicated against the reference ternary phase diagram of the symmetric bilayer (blue line in Figure. 4.1A). Triangle (orange) represents the composition $1:1:1$ which is deep in the phase coexistence region; Dot (red) is a point on the phase boundary $x_c = 10\%$. (B) Snapshot of equilibrium configuration of the asymmetric bilayer when $x = 25\%$, with POPC (gray), PSM (orange), Chol (yellow) and water (cyan). (C) Lateral pressure profile $\pi(z)$ for the same bilayer at equilibrium.

4.3. Results and discussion

We compute the local stress profile of the bilayer membrane from the virial, and use this to calculate the net surface tension, force and torque. We ensure that the prepared bilayer membrane is mechanically stable, with both the net force and torque balanced. In addition we ensure that the surface tension is zero to within numerical error. Figure 4.1A shows the phase diagram of the symmetric bilayer comprising POPC, PSM and Chol at $23°$C taken from Ref. [17]. We have simulated the symmetric bilayer membrane composed of POPC, PSM and Chol with concentration, $x = 1\%, 2\%, 5.8\%, 7.1\%, 9.1\%, 10\%, 12.5\%, 19.9\%$ and 33.3% of the PSM (Chol). We have plotted $P(\phi)$ with different x for the symmetric bilayer where, ϕ is defined as, $\phi = \frac{\rho_{PSM} - \rho_{POPC}}{\rho_{PSM} + \rho_{POPC}}$ (Figure 4.1B).

By varying x (in %) in the range $33.3 \leq x \leq 1$ at fixed temperature, we move across the equilibrium phase boundary x_c (in %) $= 10$, separating the one-phase l_d region from l_o-l_d phase coexistence. In the phase coexistence region $x > x_c = 10$, the saturated PSM preferentially partitions in the l_o phase while the unsaturated POPC partitions in the l_d phase. We find that while the

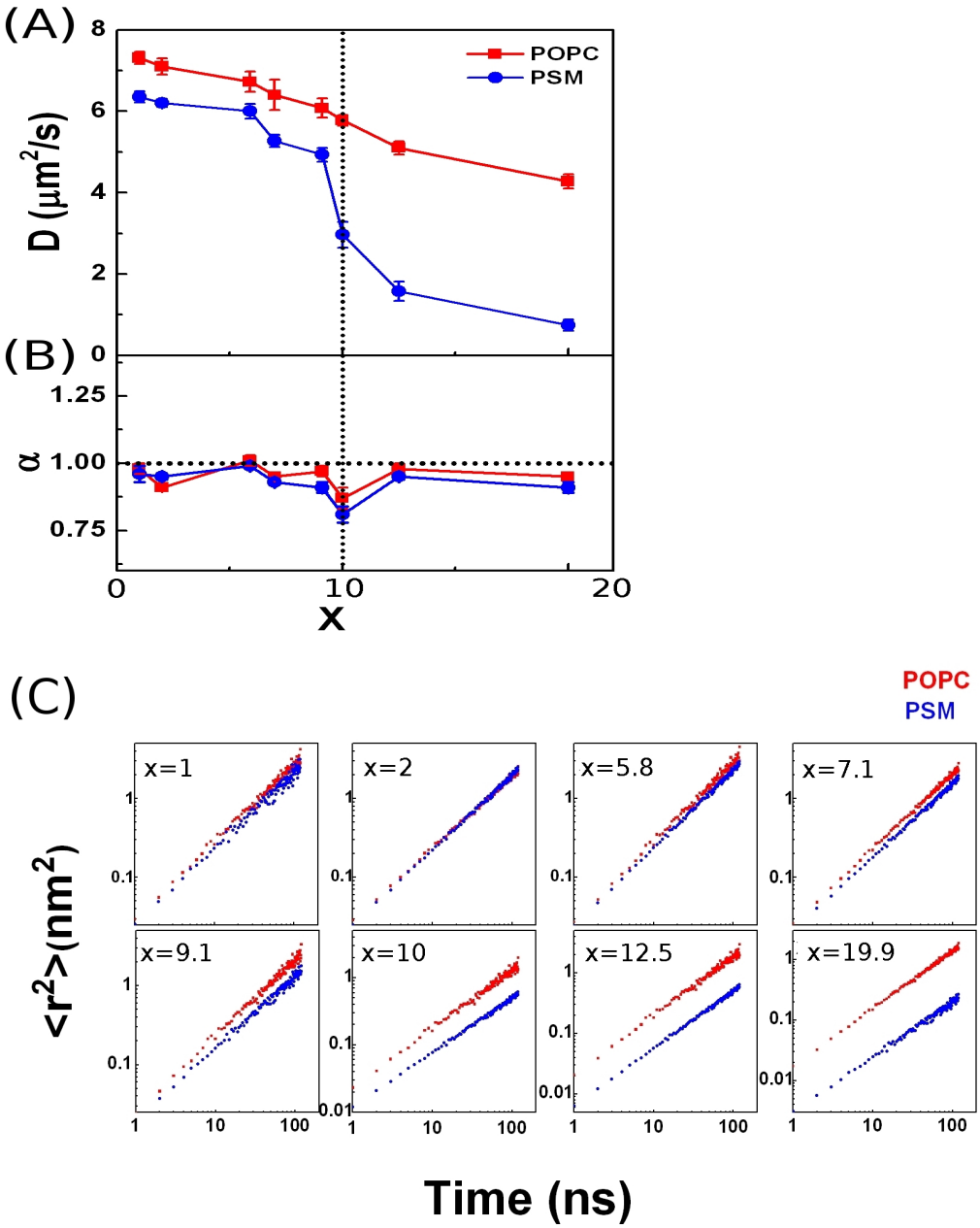

FIGURE 4.3: We study tagged-particle diffusion of POPC and PSM for the symmetric bilayer membrane composed of POPC, PSM and Chol as x, the relative concentration of PSM/Chol, is varied across the phase boundary at $x_c = 10\%$. The mean square displacement (MSD) is defined as $\langle \delta r_i(t)^2 \rangle$ of a tagged molecule, where $\delta r_i(t) = r_i(t) - r_i(0)$ is the displacement of tagged i^{th} lipid of a given species at time t from its position at $t = 0$. We fit the MSD to $\langle \delta r_i(t)^2 \rangle \propto t^{\alpha}$, and find that α is close to 1 for all values of x, suggesting simple diffusion. We then plot the diffusion coefficients of POPC and PSM as a function of x. (A) Plot of diffusion coefficients D of POPC and PSM across x_c from the MSD. (B) Plot of α of POPC and PSM across x_c from the MSD fit. (C) Panel of MSD-time plots for PSM and POPC at different values of x.

diffusion coefficient of the unsaturated POPC varies smoothly with x, the diffusion coefficient of the saturated lipid PSM experiences an *abrupt jump* at the phase boundary $x = x_c$ (Figure 4.3). This would suggest that for probes which partition into the l_o phase (e.g., 'raft'-components), we should expect an abrupt change in the diffusion coefficient as one traverses the phase boundary. This feature should hold independent of how one traverses the equilibrium phase boundary – one may either vary composition at fixed temperature or vary temperature at fixed composition.

For details of the mechanical stability of the asymmetric bilayer, (see Appendix A), where we record the net force, torque and surface tension at each composition of the asymmetric bilayer in tabular form. Here, we show a snapshot of the ternary asymmetric bilayer membrane composed of POPC, PSM and Chol and its lateral pressure profile $\pi(z)$, Figure 4.2 B and C, respectively (profiles at other concentrations are displayed in Appendix A).

We perform simulations on our model asymmetric bilayer at varying concentrations x of PSM and Chol in the lower leaflet, whilst maintaining the upper leaflet at a composition $1:1:1$, which is deep in the l_o-l_d phase coexistence region. The simulations done at various values of x along the line shown in Figure 4.2A, traverses across the phase boundary at $x_c = 10\%$ into the l_d phase.

We perform a similar study when the lower leaflet PSM is replaced by the short chain sphingomyelin, MSM.

4.3.1. Lateral compositional heterogeneity

The coarse-grained spatial profile of the lipid number density is calculated with a grid size 1.3 nm. As stated in the section *Model membrane*, the composition in the upper leaflet is fixed at $1:1:1$, while the composition of PSM/Chol in the lower leaflet is varied from 33% to 4.5%. The top and middle panels in Figure 4.4 show the spatial profile of the number density of PSM in the upper and

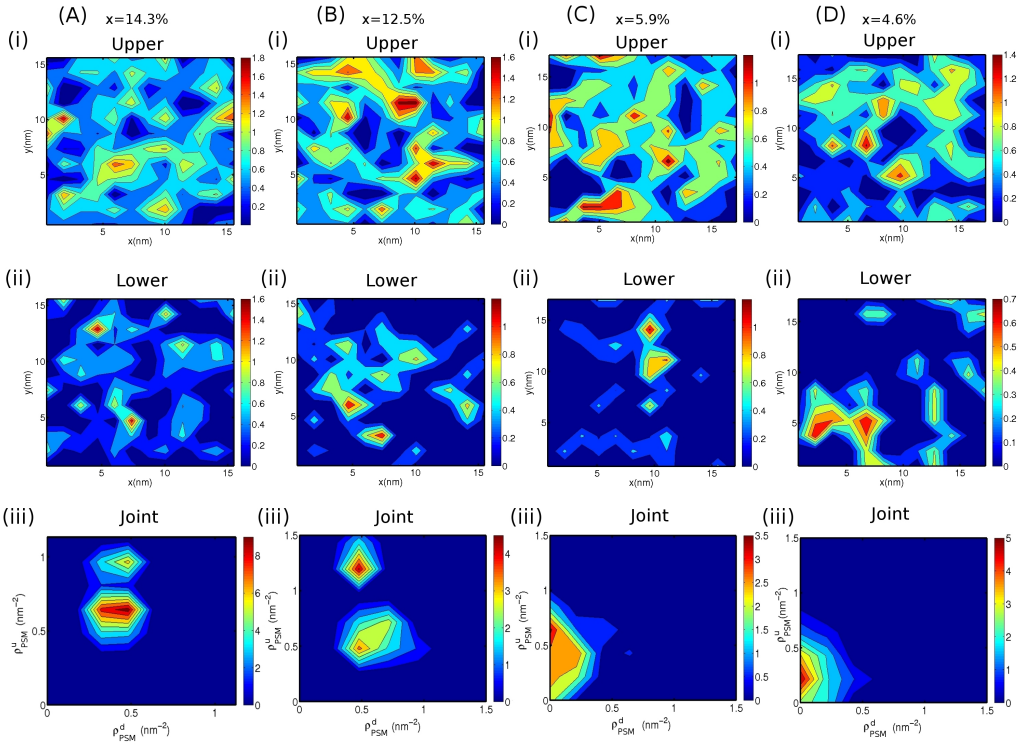

FIGURE 4.4: Spatial profile of the coarse-grained number density of PSM (color bar) in the upper leaflet (top panel) at different compositions of PSM in the lower leaflet (as indicated at the top of the panels) The middle panel shows the corresponding profile of the number density of PSM (color bar) in the lower leaflet. The bottom panel shows the extent of correlation between the PSM-rich domains across the bilayer, as measured by the joint probability distribution, JPD (color bar, see text). For $x > x_c = 10\%$, the JPD show strong transbilayer correlations, while for $x \ll x_c$, the correlations are poor.

lower leaflets, respectively, at 4 representative compositions on either side of the phase boundary, $x_c = 10\%$. The lower panel, described in the next section, shows the joint correlation of the PSM rich domains across the bilayer.

Figure 4.5 shows a similar study done when PSM in the lower leaflet is replaced by short chain MSM.

4.3.2. Domain registry across bilayer

We have studied the extent of registry of l_o-l_d domains across the bilayer of an asymmetric multicomponent membrane as a function of varying composition

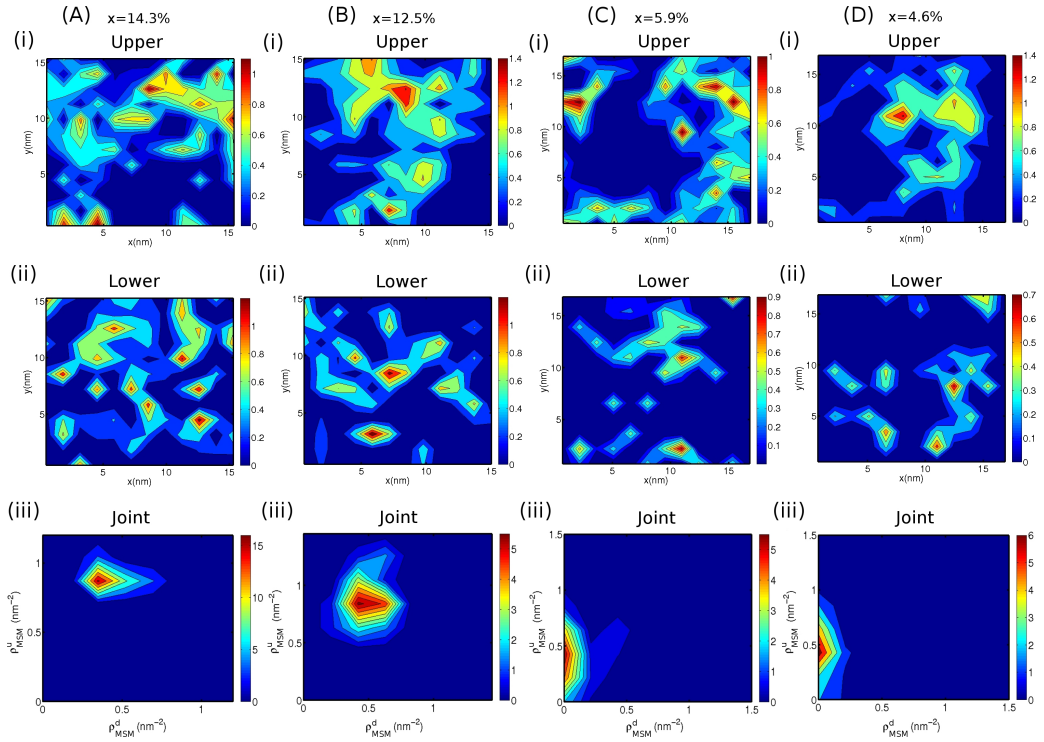

FIGURE 4.5: Spatial profile of the coarse-grained number density of PSM (color bar) in the upper leaflet (top panel) at different compositions of MSM in the lower leaflet (as indicated at the top of the panels) The middle panel shows the corresponding profile of the number density of MSM (color bar) in the lower leaflet. The bottom panel shows the extent of correlation between the PSM-rich domain in the upper leaflet and the MSM-rich domain in the lower leaflet, as measured by the joint probability distribution, JPD (color bar, see text). As in Figure 4.4, for $x > x_c = 10\%$, the JPD show strong transbilayer correlations, while for $x \ll x_c$, the correlations are poor.

and lipid chemistry. We measure the extent of transbilayer registry by computing the joint probability distribution (JPD) of the coarse-grained number density of PSM in the upper and lower leaflets at the same coarse-grained spatial location (x, y). The lower panel of Figure 4.4 shows the JPD at different values of the concentration x of PSM in the lower leaflet.

In the lower panel in Figure 4.4, the JPD shows a distinct peak along the diagonal when $x > x_c = 10\%$, which is clear evidence of *bilayer registry* of l_o-domains. The off-diagonal peak in the JPD is merely an indication of the relative abundance of PSM in the upper leaflet. On the other hand, for $x \ll x_c$, this diagonal peak in the JPD is absent, indicating lack of bilayer registry.

A similar conclusion regarding the bilayer registry can be drawn when the lower leaflet PSM is replaced by the short chain MSM (Figure 4.5).

These observations suggest that the configurations of the two leaflets mutually influence each other. We can ask whether the segregation of lipids in the upper leaflet can induce a phase segregation in lower leaflet, i.e., can the composition in the upper leaflet act as a local "field" for the composition in the lower leaflet. To study this, we define a 'transbilayer order-parameter' from the normalized transbilayer correlation (r denotes the 2d coordinate (x, y)),

$$C(\rho^u_{PSM}(x,y), \rho^d_{PSM}(x,y)) = \frac{\langle \rho^u_{PSM}(x,y)\rho^d_{PSM}(x,y)\rangle - \langle \rho^u_{PSM}(x,y)\rangle\langle \rho^d_{PSM}(x,y)\rangle}{\sqrt{\langle \rho^u_{PSM}(x,y)^2\rangle - \langle \rho^u_{PSM}(x,y)\rangle^2}\sqrt{\langle \rho^d_{PSM}(x,y)^2\rangle - \langle \rho^d_{PSM}(x,y)\rangle^2}} \quad (4.1)$$

averaged over space (denoted by C_{ud}) and compute this as a function of the relative concentration x of PSM/Chol. Figure 4.7 shows the transbilayer order-parameter C_{ud} as a function of x for a symmetric bilayer. C_{ud} jumps from a high value in the $l_o - l_d$ phase coexistence region to a low value in the l_d phase. The jump in C_{ud} coincides with the phase boundary $x_c = 10\%$ (Figure 4.1).

For the asymmetric bilayer, we compute the transbilayer order parameter as a function of x, the concentration of PSM (or MSM) in the lower leaflet (Figure 4.6). The transbilayer order parameter C_{ud} is very nearly zero for $x \ll x_c$ and rises sharply to ~ 1 at $x = x_c^{PSM} < x_c$, showing the influence of the upper leaflet on the phase segregation of the lower. This transbilayer influence is stronger for the long chain PSM than for the short chain MSM, as seen by the fact that $x_c^{MSM} = 9.09\% > x_c^{PSM} = 5.88\%$.

There is thus a shift in the phase boundary from its value of $x_c = 10\%$ for the ternary symmetric bilayer of POPC-PSM-Chol. This shift is plotted as $\Delta = |x_c^{PSM/MSM} - x_c|$ for both the long chain PSM ($\Delta^{PSM} = 4.12\%$) and short chain MSM ($\Delta^{MSM} = 0.91\%$) in the lower leaflet (inset Figure 4.6).

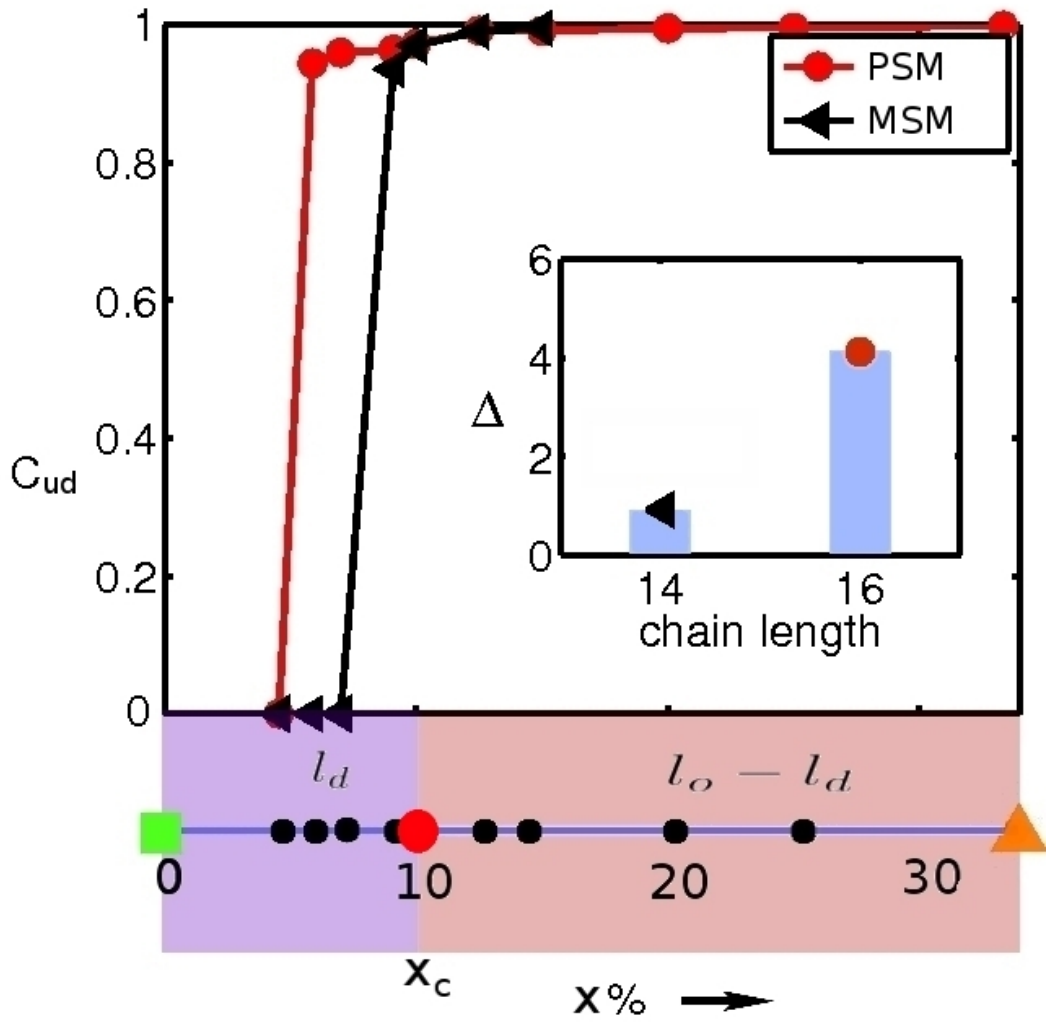

FIGURE 4.6: Transbilayer order parameter C_{ud} defined from the transbilayer correlation $C(\rho^u(r), \rho^d(r))$ (see text) between the density of upper leaflet PSM and lower leaflet PSM (red circle) or MSM (black triangle) versus x, the concentration of PSM or MSM in the lower leaflet. Color panel below drawn for reference, denotes the values of x at which C_{ud} has been evaluated. The value of C_{ud} is zero for small x and jumps sharply at $x_c^{PSM/MSM} < x_c = 10\%$ (red dot in color panel), indicating a first-order phase transition. The phase transition point for the long chained PSM, $x_c^{PSM} = 5.88\%$ is smaller than that of the short chained MSM $x_c^{MSM} = 9.09\%$. Inset shows the shift in the transition Δ (see text) as a function of lipid chain length.

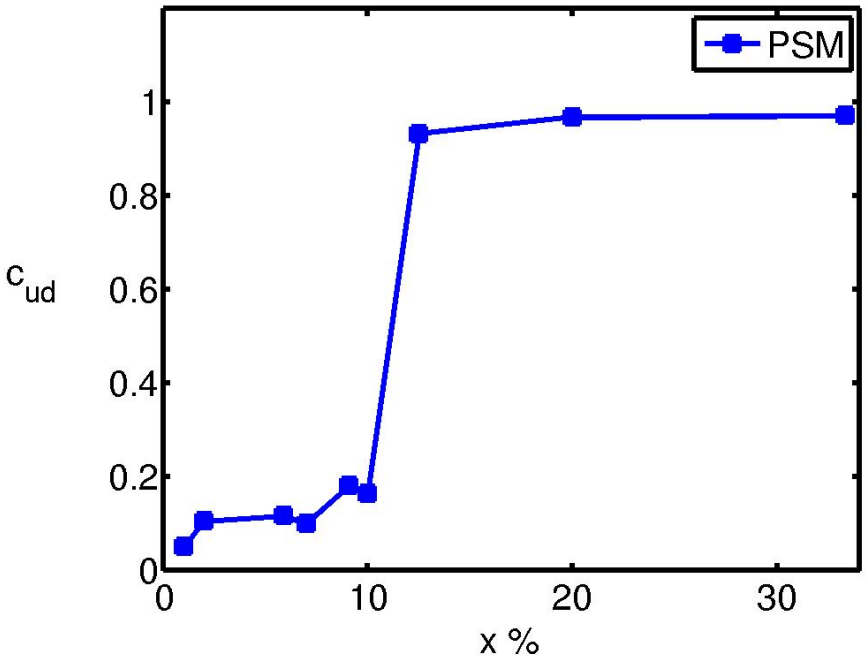

FIGURE 4.7: Transbilayer order parameter C_{ud} for the symmetric bilayer, defined from the transbilayer correlation $C(\rho^u(r), \rho^d(r))$ between the density of upper leaflet PSM and lower leaflet PSM (blue square) versus x, the concentration of PSM. The value of C_{ud} is zero for small x and jumps sharply at $x_c = 10\%$, coinciding with the first-order phase transition of the symmetric bilayer shown in Figure 4.1.

The above phenomenology can be understood within a mean-field theory of phase transitions [18], with a Helmholtz free-energy functional written in terms of ϕ_u and ϕ_d, where ϕ_u (ϕ_d) is the relative concentration of the l_o and l_d species in the upper (lower) leaflet. The form of the free-energy functional for

the asymmetric bilayer can be written as,

$$\begin{aligned} F[\phi_u, \phi_d] &= \frac{1}{2}\int d^2x\ [f_u(\phi_u) + f_d(\phi_d) + f_{ud}(\phi_u, \phi_d)] \\ f_u &= C_u(\nabla\phi_u)^2 - r_u\phi_u^2 + u\phi_u^3 + \mathrm{v}\phi_u^4 \\ f_d &= C_d(\nabla\phi_d)^2 + r_d\phi_d^2 \\ f_{ud} &= -A\phi_u\phi_d + B\phi_u\phi_d^2 + D\phi_u^2\phi_d \end{aligned} \tag{4.2}$$

where $r_u \sim (x - x_c^u), r_d \sim (x - x_c^d) > 0$ reflects the fact that the upper leaflet is in the l_o-l_d phase coexistence regime, $\langle\phi_u\rangle \neq 0$, and the isolated lower leaflet is in the l_d phase, $\langle\phi_d\rangle = 0$. The coefficient $A > 0$ to account for the fact that the local transbilayer coupling is attractive.

We first minimize F with respect to ϕ_u : setting $\delta F/\delta\phi_u = 0$, and keeping terms to linear order, we get

$$C_u\nabla^2\phi_u + r_u\phi_u = A\phi_d\,, \tag{4.3}$$

whose Fourier transform, lends itself to a useful interpretation,

$$\phi_u(\mathbf{q}) = \frac{A\phi_d(\mathbf{q})}{-C_u q^2 + r_u}\,, \tag{4.4}$$

namely a spatially varying ϕ_u can induce a spatially varying ϕ_d. Nonlinearities in the free-energy that we have neglected, reinforce this and will lead to bilayer registry. Plugging this expression back into Eq. (4.3), we obtain an effective free-energy functional in terms of ϕ_d alone, which shows that the coefficient of the quadratic term gets reduced by $r_d \to r_d - A^2/r_u$, which for large enough A can become negative. This shows that the segregation in the upper leaflet can induce a segregation in the lower, by shifting the phase transition point. This mean field analysis is entirely consistent with our MD simulations.

4.3.3. Mismatch area and interfacial tension

We calculate the coarse-grained spatial profile of the deuterium order parameter, S in each leaflet using grid size $0.5\,nm$. We use our previous estimation of the deuterium order parameter S of the l_o-l_d domains of the bilayer membrane (Chapter 3), to declare a region to be liquid-ordered (l_o) when the value of $S \geq 0.35$. We compute the area and perimeter of the l_o domains in each leaflet using the cluster algorithm available in Image Processing Toolbox, MATLAB 2009. This is used to calculate the overlap and mismatch area of the domains across the bilayer.

When there is perfect bilayer registry, the area of the l_o domain in the upper leaflet will completely overlap with the area in the lower leaflet (Figure 4.11A). Any mismatch in the overlap area will cost energy proportional to the mismatch area A, defined as $A = A^u_{l_o} + A^d_{l_o} - 2A^o$, where $A^u_{l_o}$ and $A^d_{l_o}$ are the areas of the l_o-domains in the upper and lower leaflets and A^o is the overlap area between the l_o-domains in the upper and lower leaflets (Figure 4.11B). The proportionality constant is a tension γ or a mismatch free energy per unit area, and is a measure of the domain overlap, a larger value of γ implies a more complete overlap. This tension γ acts as a driving force for inter-leaflet registration of the phase domains across the bilayer. In principle, the value of the tension γ is affected by short wavelength curvature and protrusion fluctuations, which we have ignored in our computation of the area - this will typically go to reduce the value of γ.

The linear dependence of the energy on the mismatch area A holds as long as the mean size of the mismatch region $\langle R \rangle$ is larger than its root mean square fluctuation $w = \sqrt{\langle \delta R^2 \rangle}$, where $\delta R = R(\theta) - \langle R \rangle$, and $R(\theta)$ is the distance from the domain centre to the domain boundary at the angular position θ. (see Figure 4.8). There are strong corrections to this leading behaviour, of order

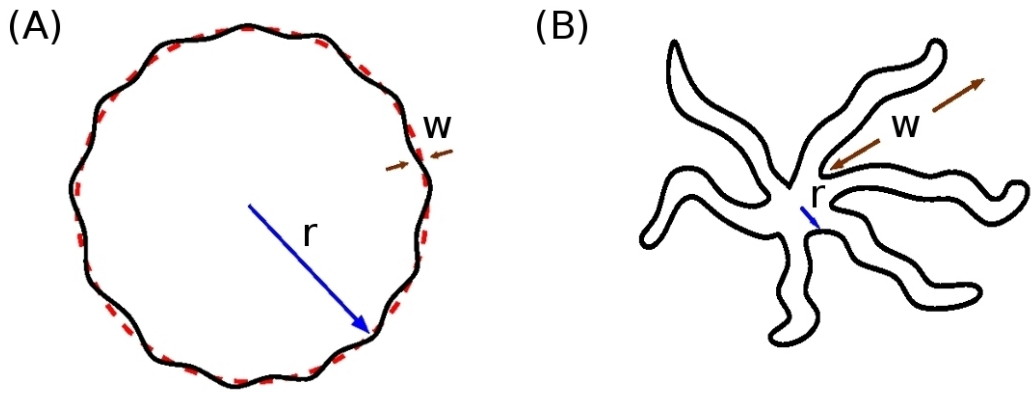

FIGURE 4.8: (A) shows the mismatch region with small fluctuation i.e., $r \gg w$ whereas (B) shows the miosmatch region where the fluctuation dominates i.e., $r \ll w$.

$(w/\langle R\rangle)^2$, when the domains are small or ramified. Given that the lateral dimension of the model membrane is 15.6 nm, this is likely the case in our atomistic MD simulations. To check this, we have plotted the perimeter per area of the mismatch region (Figure 4.9) versus area, at different values of x, the relative concentration of PSM in the lower leaflet - this shows that the mean domain shapes deviate from circularity, especially for small values of x.

With this caveat, we have estimated the domain interfacial tension γ by computing the probability distribution of the mismatch area A of the l_o-domains between the two leaflets of the bilayer, and equating it to the Boltzmann form, $P(A) \propto \exp(-\gamma A)$, where γ is measured in units of k_BT. In Figure 4.10, the plot of the probability distribution of A at various values of x, shows a distinct peak at the most probable value of A; in a semi-log plot Figure 4.11C, we fit the distribution to the Boltzmann form to extract the value of the tension γ. These values, at x well within the coexistence region, for instance $\gamma = 0.146 \pm 0.02\,\mathrm{k}_B\mathrm{T/nm}^2$ at $x = 33\%$, are consistent with those obtained from other coarse-grained simulations [19, 20]. Moreover, the qualitative trend showing γ decrease with x, with a sharp drop to zero at $x \simeq x_c^{PSM}$ (Figure 4.11D), is reassuring.

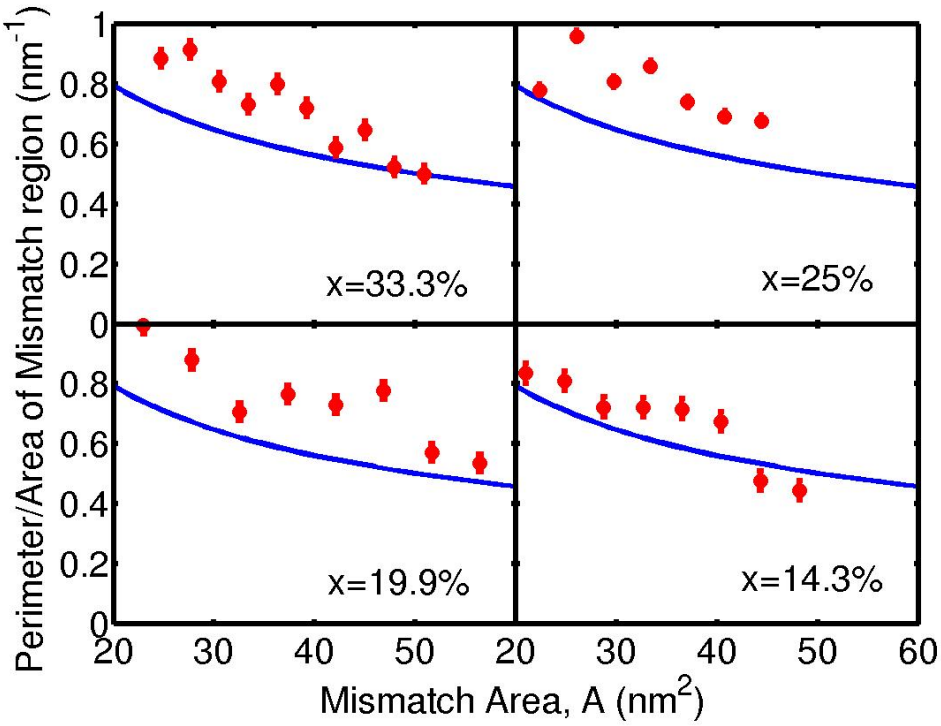

FIGURE 4.9: shows perimeter per area of the mismatch region versus area, at different values of x, the relative concentration of PSM in the lower leaflet

4.4. Conclusion and future direction

We have analyzed the equilibrium properties of a ternary component, asymmetric bilayer membrane using atomistic molecular dynamics study. Our central goal was to study the conditions under which bilayer registry takes place in an asymmetric, multicomponent membrane. To summarize, our main results are: (i) l_o phase domains formed in the two leaflets are registered across the bilayer membrane, (ii) phase segregation in upper leaflet can induce segregation in the lower, thus the composition on the upper leaflet acts as a "field" which couples linearly to the composition in the lower leaflet and (iii) the strength of the transbilayer coupling and the extent of bilayer registry depends sensitively on the lipid chain length and is greater for longer chain lipids.

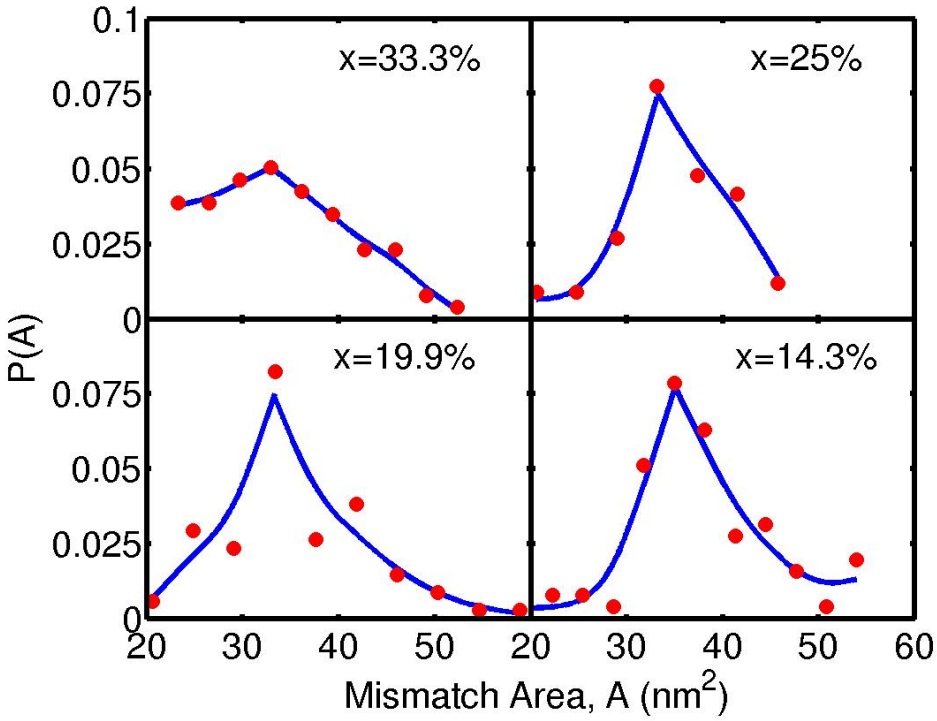

FIGURE 4.10: shows the probability distribution $P(A)$ of A at various values of x, the relative concentration of PSM in the lower leaflet

The registry of the phase domains across the two leaflets of the bilayer membrane has an important implication to the sorting and signaling in live cell membrane. The cell membrane is inherently asymmetric with both lateral and transverse lipid heterogeneity. Recent experiments on live cells, using Fluorescence Resonance Energy Transfer (FRET) [13, 14, 16] show that outer leaflet GPI-APs organized as monomers and cholesterol-sensitive nanoclusters are regulated by the active dynamics of cortical actin (CA) and myosin. The present work forms the basis for our next chapter investigation of the transbilayer interaction between lateral heterogeneities of the outer leaflet GPI-anchored proteins, PSM and cholesterol with saturated, long chain lipids at the inner leaflet whose organization depends on the actin and actin remodeling proteins.

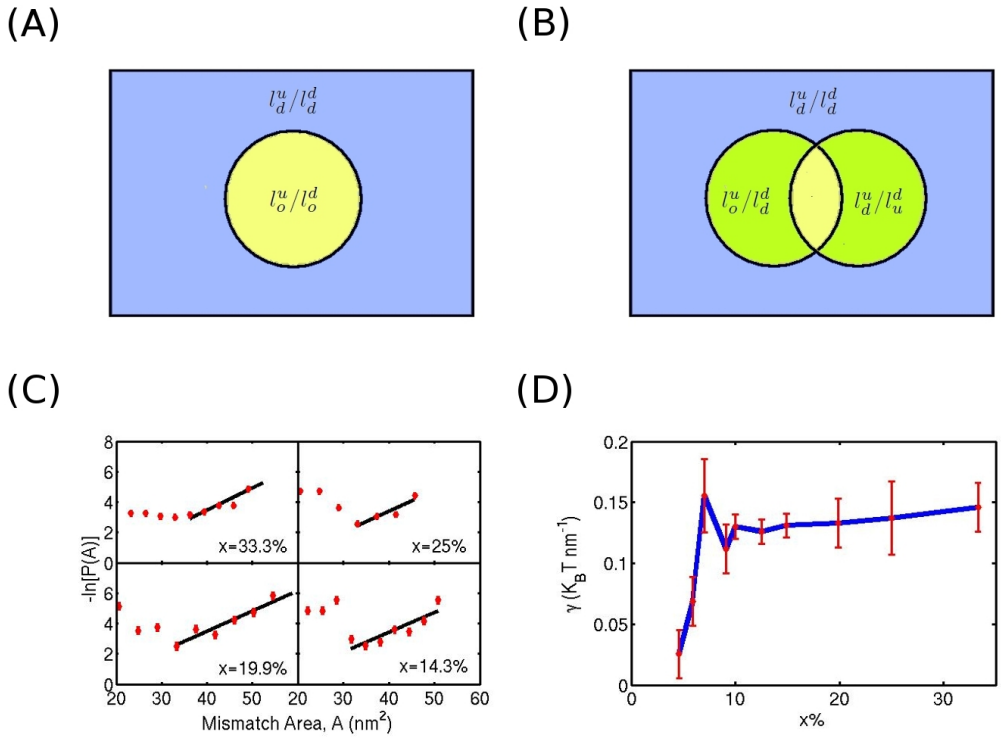

FIGURE 4.11: Schematic showing (A) domains in complete registry or overlap across the bilayer and (B) domains in partial overlap with a defined mismatch area (see text). (C) Semi-log plot of the probability distribution of the mismatch area, $-\ln P(A)$ vs. A (red dots), at different values of x, the concentration of PSM in the lower leaflet (indicated in the panel). The straight lines in the high A regime are fits to the Boltzmann form (see text), from which we extract the value of the tension γ. Error bars are indicated. (D) Tension γ as a function of x shows a sharp drop to zero at $x \simeq x_c^{PSM}$.

References

[1] D Lingwood and K Simons. Lipid rafts as a membrane-organizing principle. *Science*, 327(5961):46–50, 2010.

[2] K Simons and E Ikonen. Functional rafts in cell membranes. *Nature*, 387:569–72, 1997.

[3] K Simons and D Toomre. Lipid rafts and signal transduction. *Nat Rev Mol Cell Biol*, 1:31–39, 2000.

[4] S Mayor and M Rao. Rafts: scale-dependent, active lipid organization at the cell surface. *Traffic*, 5(4):231–40, 2004.

[5] T Baumgart, S.T Hess, and WW Webb. Imaging coexisting fluid domains in biomembrane models coupling curvature and line tension. *Nature*, 425(6960):821–4, 2003.

[6] Sarah L Veatch and Sarah L. Keller. Organization in lipid membranes containing cholesterol. *Phys. Rev. Lett.*, 89:268101, Dec 2002.

[7] Sarah L. Veatch and Sarah L. Keller. Separation of liquid phases in giant vesicles of ternary mixtures of phospholipids and cholesterol. *Biophys J.*, 85(5):3074–83, 2003.

[8] MD Collins and SL Keller. Tuning lipid mixtures to induce or suppress domain formation across leaflets of unsupported asymmetric bilayers. *Proc Natl Acad Sci U S A*, 105(1):124–128, 2008.

[9] C Wan, V Kiessling, and LK Tamm. Coupling of cholesterol-rich lipid phases in asymmetric bilayers. *Biochemistry*, 47(7):2190–8, 2008.

[10] D. W. Allender and M. Schick. Phase separation in bilayer lipid membranes: Effects on the inner leaf due to coupling to the outer leaf. *Biophys J.*, 91(8):2928–35, 2006.

[11] GG Putzel, MJ Uline, I Szleifer, and M Schick. Interleaflet coupling and domain registry in phase-separated lipid bilayers. *Biophys J.*, 100(4):996–1004, 2011.

[12] HJ Risselada and SJ. Marrink. The molecular face of lipid rafts in model membranes. *Proc Natl Acad Sci U S A.*, 105(45):17367–17372, 2008.

[13] Debanjan Goswami, Kripa Gowrishankar, Sameera Bilgrami, Subhasri Ghosh, Riya Raghupathy, Rahul Chadda, Ram Vishwakarma, Madan Rao, and Satyajit Mayor. Nanoclusters of gpi-anchored proteins are formed by cortical actin-driven activity. *Cell*, 135:1085–97, 2008.

[14] Kripa Gowrishankar, Subhasri Ghosh, Suvrajit Saha, C Rumamol, Satyajit Mayor, and Madan Rao. Active remodeling of cortical actin regulates spatiotemporal organization of cell surface molecules. *Cell*, 149:1353–67, 2012.

[15] John F. Hancock. Lipid rafts: contentious only from simplistic standpoints. *Nature Reviews Molecular Cell Biology*, 7:456–462, 2006.

[16] P Sharma, R Varma, RC Sarasij, Ira, K Gousset, G Krishnamoorthy, M Rao, and S Mayor. Nanoscale organization of multiple gpi-anchored proteins in living cell membranes. *Cell*, 116(4):577–89, 2004.

[17] Rodrigo F. M. de Almeida, Aleksandre Fedorov, and Manuel Prieto. Sphingomyelin/phosphatidylcholine/cholesterol phase diagram: Boundaries and composition of lipid rafts. *Biophys J.*, 85(4):2406–2416, 2003.

[18] P. M. Chaikin and T. C. Lubensky. *Principles of Condensed Matter Physics*. Cambridge University Press, 2000.

[19] G Garbés Putzel, Mark J. Uline, Igal Szleifer, and M Schick. Interleaflet coupling and domain registry in phase-separated lipid bilayers. *Biophys J.*, 100:996–1004, 2011.

[20] E. B. Watkins, C. E. Miller, J Majewski, and T. L. Kuhl. Membrane texture induced by specific protein binding and receptor clustering: active roles for lipids in cellular function. *Proc Natl Acad Sci U S A.*, 108(17):6975–6980, 2011.

5

Transbilayer coupling of outer leaflet GPI-APs and inner leaflet lipids across the bilayer membrane

5.1. Introduction

GPI-APs are lipid tethered proteins which reside on the outer leaflet of plasma membrane. A series of studies [1–6] have shown that GPI anchored proteins (GPI-APs) form transient cholesterol sensitive nanocluters regulated by the dynamics of actin and myosin at the cell cortex. A natural question to aske is: how does the outer-leaflet GPI-APs couple to the cortical actin that abuts the inner

leaflet of the cell membrane? Surely, there must be an indirect transbilayer coupling between the outer-leaflet GPI-anchored proteins and cortical actin or its immediate interacting partners. This naturally brings up a question: what is the molecular linkage between the GPI-APs and dynamic cortical actin? Having set the stage (Chapter 2, 3 and 4), we are now in a position to address this question using atomistic molecular dynamics (MD) simulations.

PS is the most abundant negatively charged phospholipid in the Eukaryotic cell membrane [7] and is resides predominantly in the inner leaflet of the plasma membrane. It has been reported that PS binds with CA via binding proteins [8] such as spectrin [9], talin [10], caldesmon [11]. This naturally brings up the issue of transbilayer coupling between the upper-leaflet GPI-APs and specific inner leaflet lipids (e.g., PS) and its dependence on the specificity of the lipids and its chemistry. In this chapter, we addresses these issues using atomistic molecular dynamics (MD) simulations on multicomponent asymmetric model membranes.

This chapter is organized as follows: we first describe the lateral compositional heterogeneity of the muticomponent bilayer composed of POPC, long chain palmitoyl-sphingomyelin (SM-16:0) (PSM), cholesterol (Chol) and GPI/PS. Next, we present our results on compositional dependency of the registry of GPI-APs and PS across the bilayer membrane. Then, we describe conditions under which GPI-APs and PS are registered as a function of relative concentration of the components and lipid chemistry. We end with a short summary of the results and conclusions.

5.2. Model membrane

We prepare symmetric 3-component lipid bilayer membrane composed of POPC, PSM and Chol with concentration 33% of each component. All multicomponent bilayer membranes have 512 lipids in each leaflet (with a total 1024 lipids) and

32768 water molecules (such that the ratio of water to lipid is $32 : 1$) so as to completely hydrate the simulated lipid bilayer.

We simulate the multicomponent asymmetric bilayer with different chemical structures of GPI and PS (Table-5.1).

GPI species (upper leaflet)	PS species (lower leaflet)
GPI-16:0/16:0 (long saturated GPI)	PS-18:0/18:0 (long saturated PS)
GPI-12:0/12:0 (short saturated GPI)	PS-12:0/12:0 (short saturated PS)
GPI-18:1/18:1 (long unsaturated GPI)	PS-18:1/18:1 (long unsaturated PS)

Table 5.1.: shows the structural details of GPI/PS that we have used in our studies.

I. We study 4 sets of multicomponent bilayers by adding 10 molecules of long chain GPI (GPI-16:0/16:0), long chain PS(PS-18:0/18:0), short chain GPI (GPI-12:0/12:0) and short chain PS (PS-12:0/12:0) respectively, to the above mentioned symmetric 3-component bilayer membrane having liquid ordered-liquid disordered ($l_o - l_d$) phase coexistence to find the preferable site of GPI/PS in the $l_o - l_d$ phase domains.

II. we prepare asymmetric bilayer membrane in which upper leaflet is composed of POPC (33.3%), PSM (33.3%) and Chol (33.3%) with few GPI molecules (10 molecules of GPI in total 1024 lipid bilayer membrane) and lower leaflet is composed of POPC (80%), PS (10%) and Chol (10%).

   To this asymmetric bilayer membrane following different combinations of acyl chain length of GPI/PS are added:

   A. (i) asymmetric bilayer with long chain GPI (GPI-16:0/16:0) and short chain PS (PS-12.0/12:0), (ii) asymmetric bilayer with short chain GPI (GPI-12:0/12:0) and long chain PS (PS-18:0/18:0), and (iii) asymmetric bilayer with long chain GPI (GPI-16:0/16:0) and long chain PS (18:0/18:0).

B. (i) asymmetric bilayer with unsaturated GPI (GPI-18:1/18:1) and saturated PS (PS-18:0/18:0), (ii) asymmetric bilayer with saturated GPI (GPI-18:0/18:0) and unsaturated PS (PS-18:1/18:1), and (iii) asymmetric bilayer with unsaturated GPI (GPI-18:1/18:1) and unsaturated PS (PS-18:1/18:1).

III. we prepare asymmetric multicomponent bilayers in which lower leaflet is composed of POPC (80%), long chain PS (10%) and Chol (10%) whereas, we vary the concentration, x of the PSM (Chol) at the upper leaflet having few saturated long chain GPI, across the range $x\,(in\,\%) = 0$, 4.5, 5.9, 7.1, 9.1, 10.0, 12.5 and 33.3.

IV. Finally, we study a set of multicomponent bilayer membranes where the relative concentration (x) of PSM and Chol in the upper leaflet is kept 4% while the relative concentration of Chol in the lower leaflet is varied from $x\,(in\,\%) = 15$, 20, 25, 30, 35, 40, 45 and 50 , with POPC contributing to the rest of the lipid content.

For each bilayer membrane, few (10 in number) long chain GPI (GPI-16:0/16:0) in the upper leaflet and few long chain PS (PS-18:0/18:0) in the lower leaflet are added. We simulate all these bilayers with 3 initial conditions: (i) we hold the PS at the center of the lower leaflet, while the GPI lipids remain unconstrained in the upper leaflet, (ii) we hold the GPI at the center of the upper leaflet, while the PS lipids remain free, and (iii) both GPI and PS remain unconstrained in the upper and lower leaflet respectively.

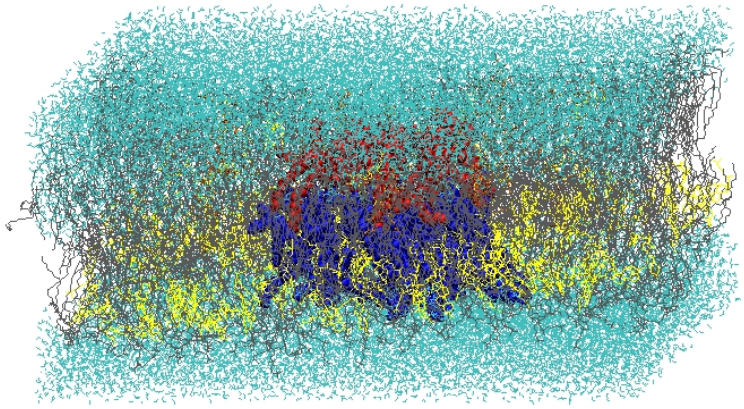

FIGURE 5.1: An equilibrium snapshot of the asymmetric bilayer where upper leaflet is composed of POPC (gray) with 4% of PSM (orrange) (Chol(yellow)) and few GPI (red) and lower leaflet is composed of POPC (gray), few PS (blue) and 35% of Chol (yellow). Water is represented by cyan.

5.3. Results and discussion

We compute the local stress profiles of all the asymmetric bilayer membranes and ensure the mechanical stability of the bilayer after getting the zero surface tension, force balanced and torque balanced membrane (shown in Appendix A). We show the snap shot of the ternary asymmetric bilayer membrane composed of POPC, PSM and Chol with GPI in the upper leaflet and PS in the lower leaflet in Figure 5.1.

5.3.1. Partitioning of GPI/PS in muliticomponent bilayer membrane

The homogeneous mixed phase of the symmetric 3-component bilayer having suitable compositions of POPC (33.3%), PSM (33.3%) and Chol (33.3%) undergoes phase separation at the temperature 23°C. Phase coexistence of stable

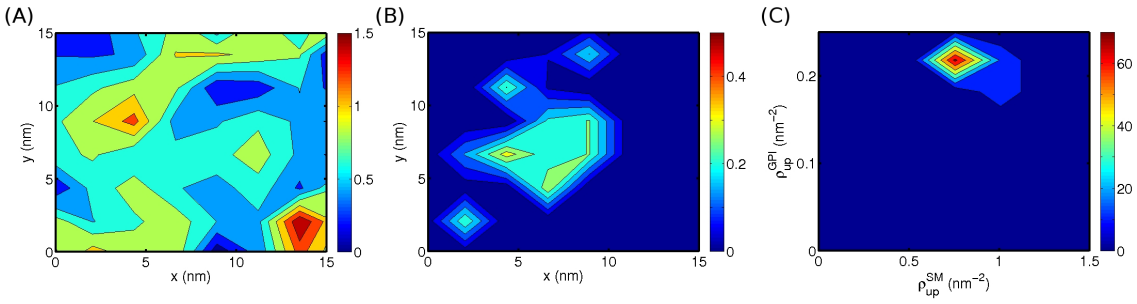

FIGURE 5.2: (A) and (B) show the spatial density of PSM and GPI of the bilayer membrane composed of POPC, PSM and Chol with the ratio $1:1:1$ and few GPI. (A) and (B) show that both, saturated long chain GPI and PSM have been enriched in the same region. The extent of correlation between the PSM-rich domain and GPI-rich domain in the upper leaflet of the bilayer membrane, as measured by the joint probability distribution, JPD shown in (C), indicates that saturated long chain GPI and PSM are correlated.

POPC-rich l_d and PSM-rich l_o domains have been observed in which Chol partitions more in l_o domains [12, 13]. We study 4 bilayer membrane where we uniformly add few saturated long chain GPI, few saturated long chain PS, few saturated short chain GPI and few saturated short chain PS, respectively, to the above symmetric equilibrated ternary bilayer membrane. Since very few GPI-APs/PS are added, they act as 'impurities' [1] to the bilayer membrane.

Here, we have added saturated long (short) chain GPI (PS) to the symmetric ternary bilayer membrane with phase coexistence of PSM-rich l_o - POPC-rich l_d domains [12, 13] to explore where saturated long (short) chain GPI (PS) would like to partition. Initially, GPI lipids are uniformly distributed to the multi-component bilayer membrane of POPC/PSM/Chol.

After the equilibration, the spatial heterogeneity of the saturated long chain GPI and PSM are shown in Figure 5.2 (A) and (B), respectively. Figure 5.2 (A) and (B) show that both saturated long chain GPI and PSM are enriched in the same region of the bilayer membrane. We measure the extent of the correlation between PSM-rich l_o domain and saturated long chain GPI by computing joint

[1] by 'impurities', we mean that the presence of a small number of GPI-APs does not affect the ternary phase diagram (Figure 4.1) of POPC/PSM/Chol [14]

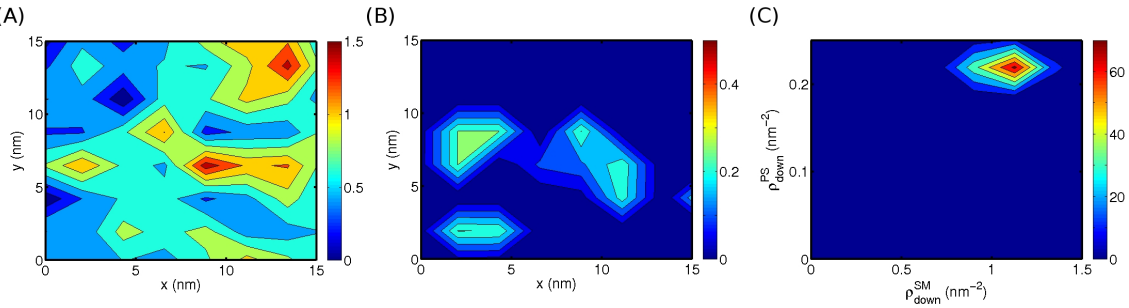

FIGURE 5.3: (A) and (B) show the spatial density of PSM and PS of the bilayer membrane composed of POPC, PSM and Chol with the ratio $1:1:1$ and few PS. (A) and (B) show that both, PS and PSM have been enriched in the same region. The extent of correlation between PSM-rich domain and saturated long chain PS-rich domain in the lower leaflet of the bilayer membrane, as measured by the JPD of PSM to PS shown in (C) indicates that saturated long chain PS and PSM are correlated.

probability distribution (JPD) of the coarse-grained number density of PSM in the upper leaflet and GPI in the upper leaflet at the same coarse-grained spatial location (x,y) (Figure 5.2 (C)) which indicates that long chain GPI are correlated with PSM-rich l_o domains.

We follow the same prescription for saturated long chain PS, saturated short chain GPI and saturated short chain PS and the spatial density and JPD of PSM and long (short) GPI (PS) are shown in Figure 5.2, 5.3, 5.4, 5.5, respectively. We find that both saturated long chain GPI and saturated long chain PS prefer to partition in PSM-rich l_o domains where as both saturated short chain GPI and saturated short chain PS are distributed homogeneously in the bilayer membrane and there is no correlation between the PSM-rich l_o domains and saturated short chain GPI (PS).

We have defined a 'lateral correlation',C_{uu}, from the normalized correlation,

$$C(\rho^u_{GPI/PS}(x,y),\rho^u_{SM}(x,y)) = \frac{\langle\rho^u_{GPI/PS}(x,y)\rho^u_{SM}(x,y)\rangle - \langle\rho^u_{GPI/PS}(x,y)\rangle\langle\rho^u_{SM}(x,y)\rangle}{\sqrt{\langle\rho^u_{GPI/PS}(x,y)^2\rangle - \langle\rho^u_{GPI/PS}(x,y)\rangle^2}\sqrt{\langle\rho^u_{SM}(x,y)^2\rangle - \langle\rho^u_{SM}(x,y)\rangle^2}}$$

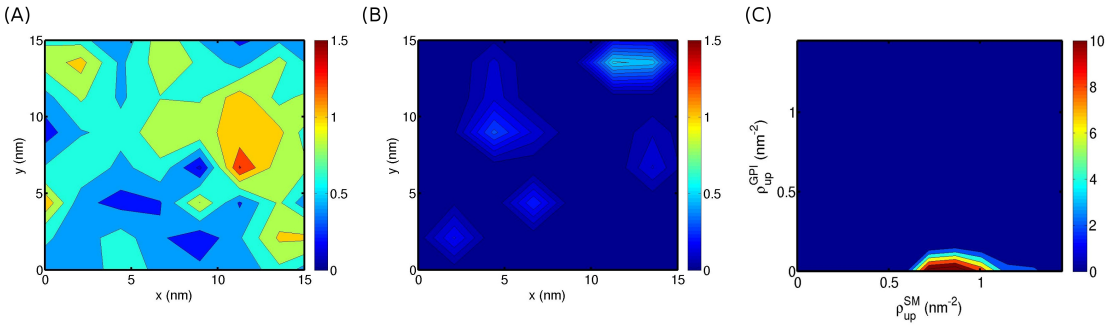

FIGURE 5.4: (A) and (B) show the spatial density of PSM and short chain GPI (GPI 12:0/12:0) of the bilayer membrane composed of POPC, PSM and Chol with the ratio $1:1:1$ and few GPI. (B) shows that there is no enrichment of short chain GPI in the upper leaflet and GPI lipids are homogeneously distributed through out the membrane. The JPD of the PSM to GPI shown in (C) indicates that there is no correlation between the saturated short chain GPI and PSM.

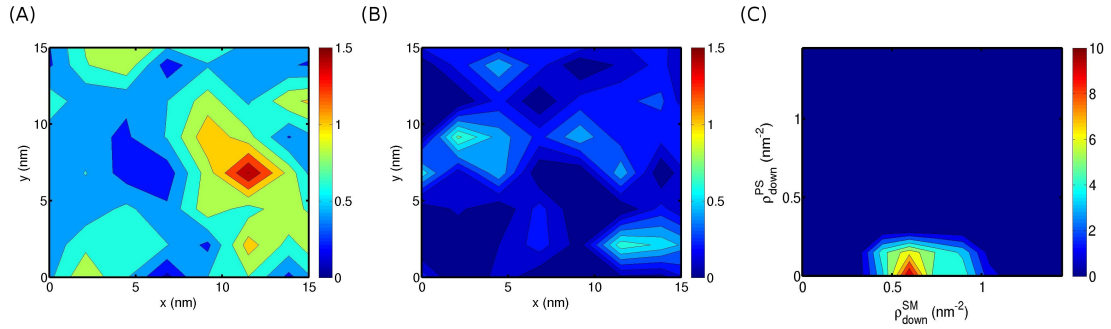

FIGURE 5.5: (A) and (B) show the spatial density of PSM and short chain PS (PS 12:0/12:0) of the bilayer membrane composed of POPC, PSM and Chol with the ratio $1:1:1$ and few PS. (B) shows that there is no enrichment of short chain PS in the lower leaflet and PS lipids are homogeneously distributed through out the membrane. The JPD of the PSM to PS shown in the (C) indicates that there is no correlation between saturated short chain PS and PSM.

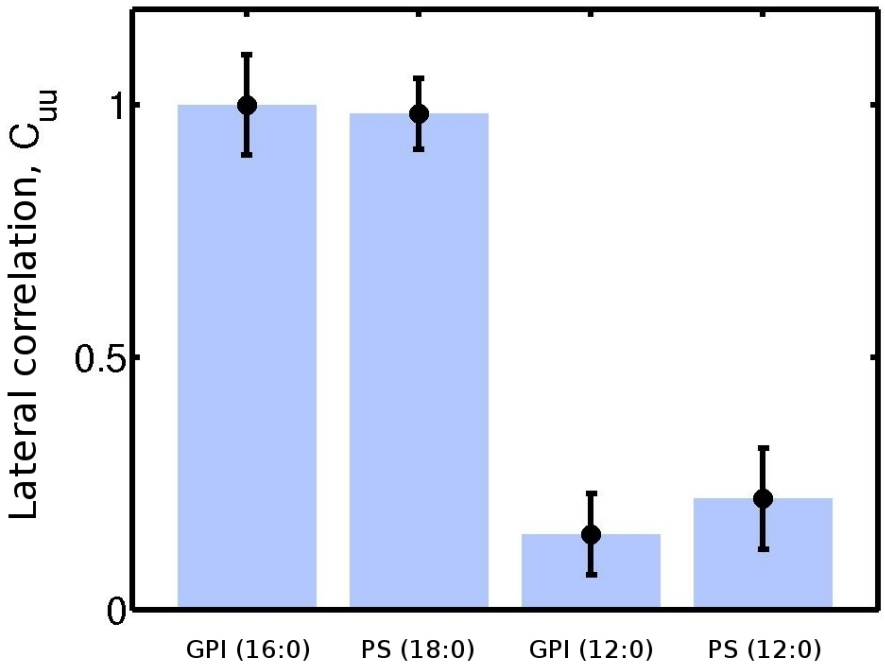

FIGURE 5.6: shows the lateral correlation, C_{uu} for the long chain GPI (GPI 16:0/16:0), long chain PS (PS 18:0/18:0), short chain GPI (GPI 12:0/12:0) and short chain PS (PS 12:0/12:0) to the SM in the symmetric bilayer membrane comprising POPC, PSM and Chol respectively.

averaged over $x - y$ plane and compute this for long (short) chain GPI(PS).

C_{uu} for the long chain GPI, long chain PS, short chain GPI and short chain PS to the PSM in the bilayer membrane respectively, are shown in Figure 5.6. The high value of C_{uu} for the saturated long chain GPI (PS) and PSM indicates that long chain GPI (PS) are correlated with the PSM-rich l_o phase domain and prefers to partition in l_o domains in the multicomponent bilayer membrane whereas, low value of C_{uu} for the saturated short chain GPI (PS) and PSM indicates that saturated short chain GPI (PS) are weakly correlated to PSM-rich l_o domains in the multicomponent bilayer membrane.

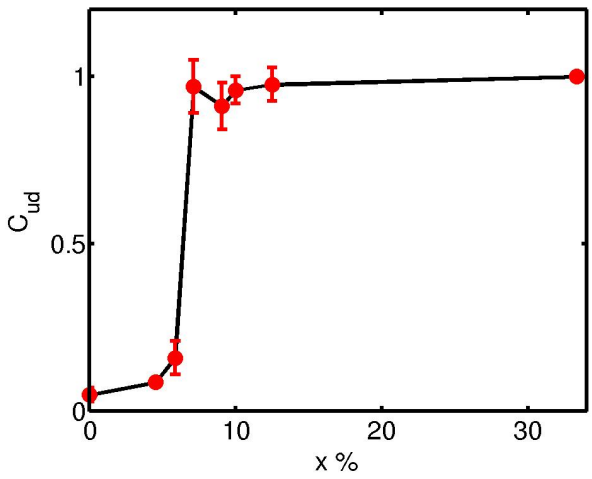

FIGURE 5.7: Transbilayer order parameter C_{ud} defined from the transbilayer correlation $C(\rho^u_{GPI}(x,y), \rho^d_{PS}(x,y))$ between the spatial density of the GPI of the upper leaflet to that of the PS of the multicomponent asymmetric bilayer while lower leaflet is composed of POPC, long chain saturated PS and Chol in a ratio $8:1:1$ whereas the upper leaflet is composed of POPC and $x\%$ of PSM (Chol) and a few long chain saturated GPI lipids. The value of C_{ud} is zero for small x and jumps sharply at $x_c^{PSM} = 7\%$ (red dot in color panel), indicating a first-order phase transition.

5.3.2. Compositional dependence of the registry between the GPI-APs and PS across the bilayer membrane

In this subsection, we characterize the effect of the local environment on the transbilayer coupling between the upper leaflet GPI and the lower leaflet PS lipids.

For this, we study the multicomponent asymmetric bilayer membrane in which lower leaflet is composed of POPC, long chain saturated PS and Chol in a ratio $8:1:1$ whereas the upper leaflet is composed of POPC, PSM, Chol and a few long chain saturated GPI lipids with relative concentration, x (in $\%$)$= 0$, 4.5, 5.9, 7.1, 9.1, 10.0, 12.5 and 33.3 of PSM and Chol.

We vary the concentration of PSM (Chol) in the upper leaflet to measure the

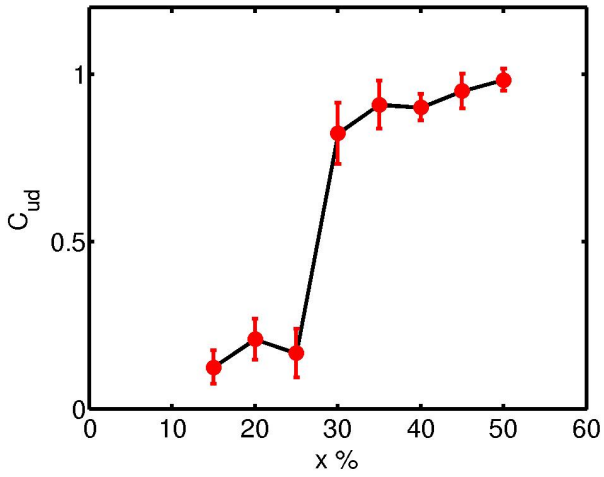

FIGURE 5.8: Transbilayer order parameter C_{ud} defined from the transbilayer correlation $C(\rho^u_{GPI}(x,y), \rho^d_{PS}(x,y))$ between the spatial density of the GPI of the upper leaflet to that of the PS of the multicomponent asymmetric bilayer where upper leaflet is composed of POPC, PSM and Chol with 4% PSM (Chol) having few GPI lipids and lower leaflet is composed of POPC and $x\%$ of Chol with few PS hold at the centre. The value of C_{ud} is zero for small x and jumps sharply at $x_c^{Chol} = 25\%$ (red dot in color panel), indicating a first-order phase transition.

extent of transbilayer registry between upper leaflet GPI and lower leaflet PS by computing a 'transbilayer order-parameter',C_{ud}, from the normalized transbilayer correlation,

$$C(\rho^u_{GPI}(x,y), \rho^d_{PS}(x,y)) = \frac{\langle \rho^u_{GPI}(x,y)\rho^d_{PS}(x,y)\rangle - \langle \rho^u_{GPI}(x,y)\rangle\langle \rho^d_{PS}(x,y)\rangle}{\sqrt{\langle \rho^u_{GPI}(x,y)^2\rangle - \langle \rho^u_{GPI}(x,y)\rangle^2}\sqrt{\langle \rho^d_{PS}(x,y)^2\rangle - \langle \rho^d_{PS}(x,y)\rangle^2}}$$

averaged over 2d space and compute this as a function x, the concentration of PSM (Chol) in the upper leaflet (Figure 5.5) of the bilayer where the lower leaflet contains 10% of the PS (Chol).

The value of C_{ud} is small for $x \ll x_c^{PSM}$ and rises sharply to ~ 1 at $x = x_c^{PSM}$,

showing the influence of the upper leaflet composition on the transbilayer coupling between GPI and PS. The low value of C_{ud} implies that upper leaflet GPI is weakly correlated with lower leaflet PS for $x \ll x_c$ whereas the high value of C_{ud} indicates the strong correlation between saturated long chain GPI and saturated long chain PS for $x \gg x_c$. The critical transition value, x_c separating the l_d phase ans $l_o - l_d$ phase coexistence is 10% [14] for the ternary symmetric bilayer of POPC-PSM-Chol. We find that the strength of the 'field' of the transbilayer coupling across the bilayer can hold upper leaflet GPI and lower leaflet PS upto the critical concentration $x_c^{PSM} = 7\%$, and below that it fails to keep registry between upper leaflet GPI and lower leaflet PS.

Next, we have studied the multicomponent asymmetric bilayer in which the upper leaflet is composed of POPC, PSM and Chol with small amount of saturated PSM (Chol), x (in %) $= 4 < x_c^{PSM}$ with a few saturated long chain GPI such that the upper leaflet is in l_d phase, whereas the lower leaflet is composed of POPC and Cholesterol and a few PS a the center of the leaflet. Figure 5.7 shows that there is no bilayer registry between GPI and PS if the concentration of saturated PSM in the upper leaflet is $x(= 4\%) < x_c^{PSM}$, while the lower leaflet contains 10% of PSM (Chol). Now, we perform simulations maintaining the upper leaflet composition with 4% PSM (Chol) whilst we vary the relative concentration, x of Chol at the lower leaflet across the range x (in $\%$)$= 15$, 20, 25, 30, 35, 40, 45 and 50.

Holding PS lipids at the center of the lower leaflet simulates the situation where PS in the inner leaflet is bound by the cortical actin via binding proteins. To measure the extent of transbilayer coupling, we calculate C_{ud} with varying the concentration x of Chol at the lower leaflet. The small value of C_{ud} for $x \ll x_c^{Chol}$ indicates weak correlation between GPI and PS whereas it jumps sharply to high value for $x \gg x_c^{Chol}$, showing the transbilayer registry of GPI and PS. Figure 5.8 shows that the transbilayer coupling across the bilayer can hold upper leaflet GPI and lower leaflet PS above the critical concentration

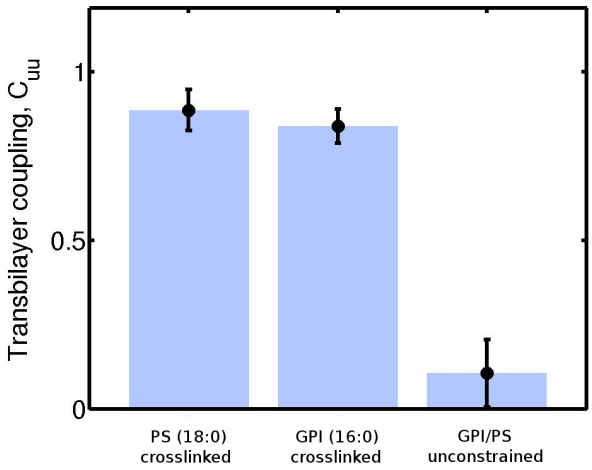

FIGURE 5.9: shows the Transbilayer coupling order parameter C_{ud} defined from the transbilayer correlation $C(\rho^u_{GPI}(x,y), \rho^d_{PS}(x,y))$ between the spatial density of the GPI of the upper leaflet to that of the PS of the multicomponent asymmetric bilayer where upper leaflet is composed of POPC, PSM and Chol with 4% PSM (Chol) having few GPI lipids and lower leaflet is composed of POPC and 35% of Chol with few PS. We plot the value of C_{ud} for three conditions: (i) where the PS in the lower leaflet are cross-linked, (ii) where GPI in the upper leaflet are cross-linked and (iii) where there is no constraint imposed on the both GPI/PS lipids.

$x_c^{Chol} = 25\%$ even if the bilayer is in l_d phase.

5.3.3. Bilayer registry of upper leaflet GPI to lower leaflet PS depending on constraints

We study the multicomponent bilayer membrane in which the upper leaflet is composed of POPC, PSM and Chol having 4% of PSM (Chol) with few [2] saturated long chain GPI where as the lower leaflet is composed of POPC with 35% ($> x_c^{Chol}$) of Chol with few [3] saturated long chain PS as mentioned in earlier subsection. Here, we perform the simulation with different conditions starting

[2] 10 in number of GPI in total 1024 lipid membrane
[3] 25 in number of PS in total 1024 lipid membrane

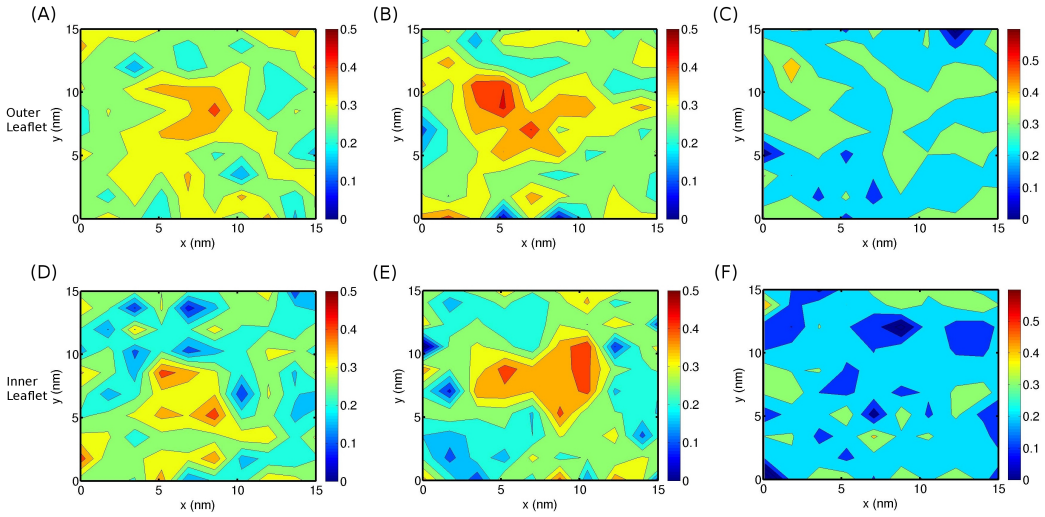

FIGURE 5.10: shows the spatial heterogeneity of deuterium order parameter, (S) of the outer (A-C) and inner leaflet (D-F) of asymmetric bilayer membrane for the all three conditions: (i) spatial heterogeneity of S for the bilayer where PS lipids in the lower leaflet are cross-linked as shown in A and D respectively, (ii) spatial heterogeneity of S for the bilayer where GPI lipids in the outer leaflet are cross-linked as shown in B and E respectively, and (iii) spatial heterogeneity of S for the bilayer where both GPI/PS lipids are unconstrained shown in C and F respectively.

from the configuration where the GPI and PS are at the center of bilayer membrane.

From this initial configuration, we perform the MD simulation of the asymmetric bilayer membrane and investigate the transbilayer coupling between GPI and PS across the asymmetric bilayer membrane for the three different conditions: (i) all the lipids in the asymmetric bilayer are free to move, except PS in the lower leaflet as if PS lipids are cross-linked from the inside of the membrane, (ii) all lipids in the bilayer membrane are free to move, except upper leaflet GPI as if GPI lipids are cross-linked from outside of the membrane, and (iii) no constraint is imposed on the bilayer membrane and all the lipids are moving freely.

Figure 5.9 shows that the value of C_{ud} between GPI to PS is high (~ 1) indicating high correlation between GPI and PS for the first two cases i.e.,

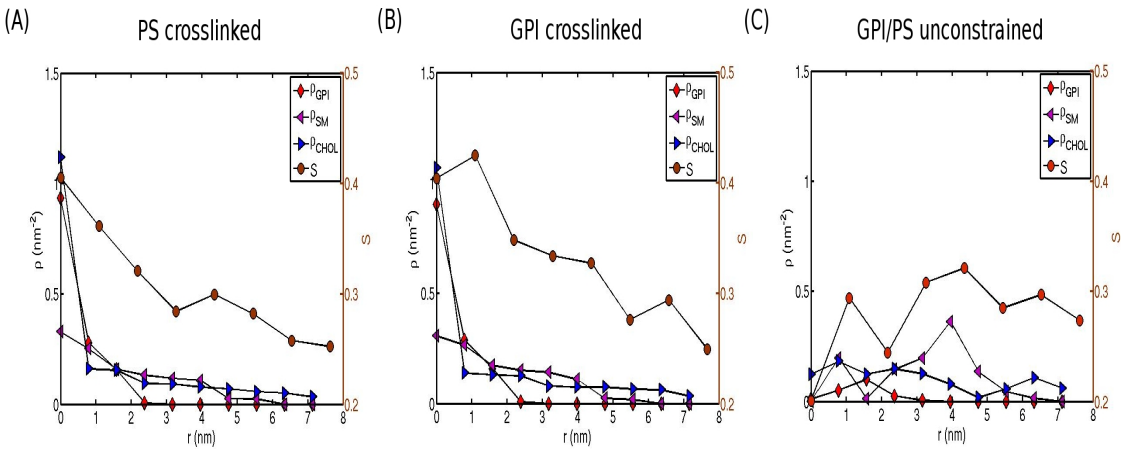

FIGURE 5.11: shows the density of upper leaflet GPI (ρ_{GPI}), PSM (ρ_{SM}) and Chol (ρ_{CHOL}) and deuterium order parameter, S as a function of radial position (r) of asymmetric bilayer membrane for the all three conditions: (A) where PS lipids in the lower leaflet are cross-linked, (B) where GPI lipids in the outer leaflet are cross-linked and (C) where both GPI/PS lipids are unconstrained, respectively.

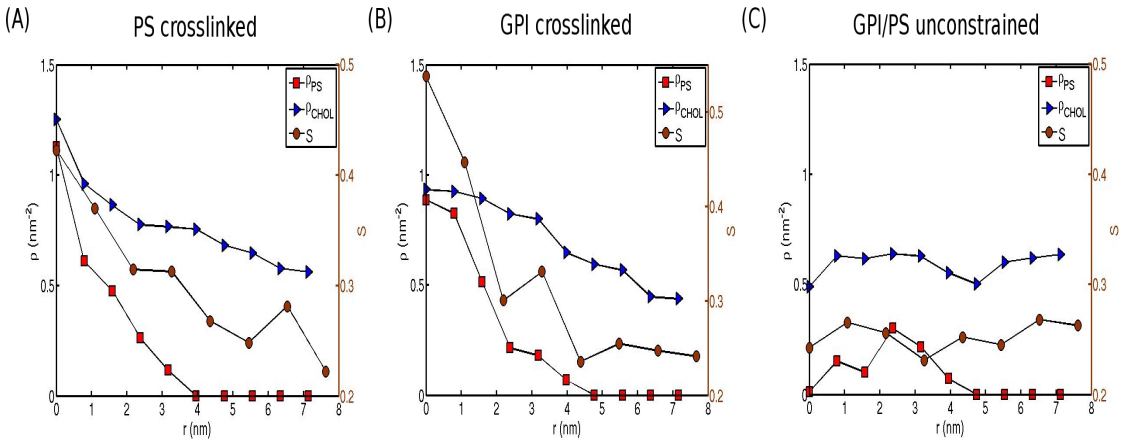

FIGURE 5.12: shows the density of lower leaflet PS (ρ_{PS}) and Chol (ρ_{CHOL}) and deuterium order parameter, S as a function of radial position (r) of asymmetric bilayer membrane for the all three conditions: (A) where PS lipids in the lower leaflet are cross-linked, (B) where GPI lipids in the outer leaflet are cross-linked and (C) where both GPI/PS lipids are unconstrained, respectively.

either PS lipids are held or GPI lipids are held. But, the value of C_{ud} is very low for the bilayer membrane where there is no constraint imposed on any lipids. Therefore, the upper leaflet GPI and lower leaflet PS are registered only if either of them are crosslinked.

We calculate the spatial heterogeneity of the deuterium order parameter, S of the upper leaflet and lower leaflet of the asymmetric bilayer membrane for all three conditions. The spatial heterogeneity of S of the upper leaflet for the three conditions are shown in the upper panel of Figure 5.10 whereas, that of the lower leaflet are shown in the lower panel of Figure 5.10. From Figure 5.10 A and D showing spatial heterogeneity of S of the two leaflets when the PS is cross-linked in the lower leaflet, we find that the value S is high at the center of both the leaflets indicating the formation of local l_o domain surrounded by globally l_d phase. Again, we find a similar l_o domain in both the leaflets when GPI is cross-linked in the upper leaflet in Figure 5.10 B and E, respectively. The value of S is low in the entire space in both the leaflets (Figure 5.10 C and F) indicating the formation of only l_d phase when there is no constraint on lipids. This indicates when PS (GPI) are held in the lower (upper) leaflet of the bilayer membrane, it creates a local l_o domain in the lower (upper) leaflet of the bilayer membrane and induces the upper (lower) leaflet GPI (PS) to be registered. However, the low value of S away from the vicinity of GPI/PS indicates l_d phases surrounding the cluster of GPI/PS lipids in both upper and lower leaflet.

Again, Figures 5.11 and 5.12 show the variation of S with the radial position ($r = r(x, y)$) for both upper and lower leaflets at all three conditions, respectively. We find that there is a high value (> 0.35) of S (indicating l_o phase) at the center for both upper and lower leaflet which falls to low value (< 0.35) (indicating l_d phase) after 1 nm for the first two conditions when either of the GPI/PS lipids held (cross-linked) shown in Figure 5.11 (A-B) and 5.12 (A-B), respectively. On the other hand, the density of the upper leaflet and lower leaflet

components are nearly flat and uniform, indicating the homogeneous distributions of the components in both leaflets (Figures 5.11 (C) and 5.12 (C)). As a consequence, the value of S in both leaflets are low in the entire regions suggesting the formation of only l_d phases in both leaflets, when GPI/PS are unconstrained.

Therefore, when PS (GPI) lipids are held in the lower (upper) leaflet, a local enrichment of saturated long chain PS (GPI) along with Chol in the lower (upper) leaflet form local l_o domain though the bilayer is globally in the l_d phase. The local l_o phase domain in the lower (upper) leaflet by holding PS (GPI) acts as 'field' to the upper (lower) leaflet and register the GPI (PS) in presence of saturated long chain lipid, PSM.

5.3.4. Structural dependency of the transbilayer coupling between the upper leaflet GPI to lower leaflet PS

In this subsection, we study the transbilayer coupling between the upper leaflet GPI and lower leaflet PS as a function of lipid chemistry.

I. **Dependency on acyl chain length :**

We simulate the multicomponent bilayer in which upper leaflet is composed of POPC/PSM/Chol (33.3% each) with few GPI lipids and lower leaflet with POPC/PS/Chol with 10% of PS (Chol) and study the bilayer registry between GPI and PS as a function acyl chain length of the lipids. We simulate the asymmetric bilayer membrane with (i) long chain GPI and short chain PS, (ii) short chain GPI and long chain PS and (iii) long chain GPI and short chain PS, respectively. We have calculated the spatial heterogeneity of each components of the bilayer membrane from which the JPD of GPI of the upper leaflet to PS of the lower leaflet for all the bilayer membranes have been computed.

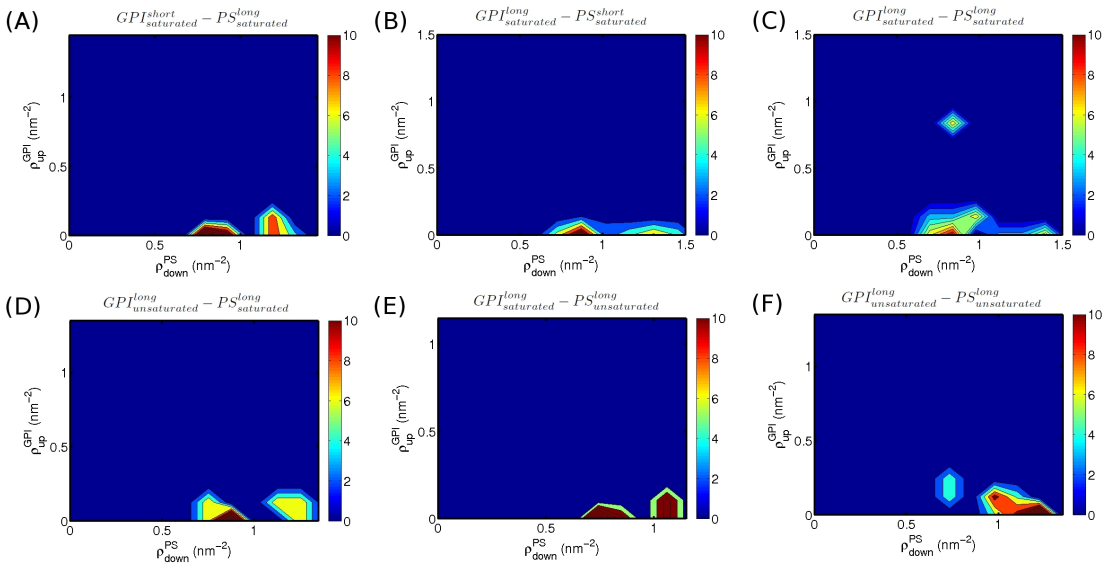

FIGURE 5.13: (A-C) show the JPD of GPI to PS for the multicomponent asymmetric bilayer having (i) long, saturated chain GPI and short, saturated chain PS, (ii) short, saturated chain GPI and long, saturated chain PS and (iii) long, saturated chain GPI and short, saturated chain PS wheresas, (D-F) show the JPD of GPI to PS for the multicomponent asymmetric bilayer having (i) long, unsaturated chain GPI and long, saturated chain PS, (ii) long, saturated chain GPI and long, unsaturated chain PS and (iii) long, unsaturated chain GPI and long, unsaturated chain PS. The upper leaflets of all 6 multicomponent bilayers are composed of POPC, PSM and Chol in a ratio $1:1:1$ with a few number of GPI whereas the lower leaflets are composed of POPC, PS and Chol in a ratio $8:1:1$.

Figure 5.13 (A-C) show the JPD of GPI to PS for the multicomponent asymmetric bilayer having (i) long chain GPI and short chain PS, (ii) short chain GPI and long chain PS and (iii) long chain GPI and short chain PS, respectively. Figure 5.13 (A) and (B) show that there is no correlation between the upper leaflet GPI to lower leaflet PS, while Figure 5.13 (C) shows a bilayer registry between the upper leaflet long chain saturated GPI to the lower leaflet long chain saturated PS.

II. **Dependency on lipid chain saturation :**

Similarly, we study the asymmetric multicomponent bilayer with upper leaflet composed of POPC/PSM/Chol (33.3% each) with few GPI lipids and lower

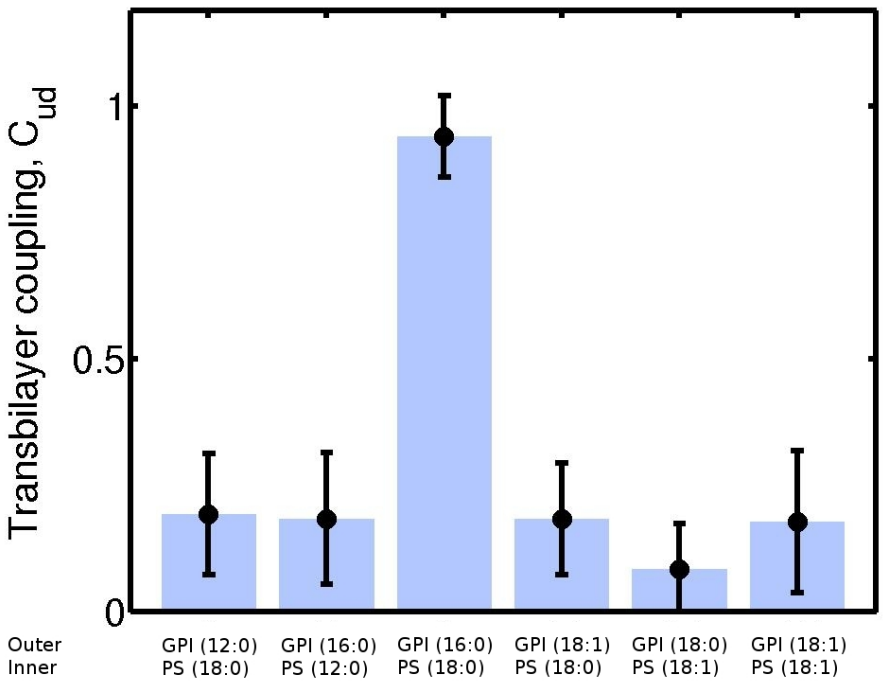

FIGURE 5.14: shows the transbilayer order parameter C_{ud} defined from the transbilayer correlation $C(\rho^u_{GPI}(x,y), \rho^d_{PS}(x,y))$ between the spatial density of the GPI of the upper leaflet to that of the PS of the multicomponent asymmetric bilayer having (i) long, saturated chain GPI and short, saturated chain PS, (ii) short, saturated chain GPI and long, saturated chain PS, (iii) long, saturated chain GPI and short, saturated chain PS, (iv) long, unsaturated chain GPI and long, saturated chain PS, (v) long, saturated chain GPI and long, unsaturated chain PS and (vi) long, unsaturated chain GPI and long, unsaturated chain PS. The upper leaflets of all 6 multicomponent bilayers are composed of POPC, PSM and Chol in a ratio $1:1:1$ with a few number of GPI whereas the lower leaflets are composed of POPC, PS and Chol in a ratio $8:1:1$.

leaflet composed of POPC/PS/Chol with 10% of PS (Chol) and study the bilayer registry between the GPI and PS as a function of saturation level of the lipids. Here, we perform the simulation of the asymmetric bilayer with (i) saturated GPI and unsaturated PS, (ii) unsaturated GPI and saturated PS and (iii) unsaturated GPI and unsaturated PS, respectively.

The JPD of the upper leaflet GPI to the lower leaflet PS for all three bilayers shown in Figure 5.13 (D-F) indicate that there is no correlation between GPI and PS if either of two has unsaturated acyl chain.

Again, to measure the extent of the transbilayer registry between the GPI and PS, we compute C_{ud} for all 6 bilayers as shown in Figure 5.14. The value of C_{ud} is high only for the asymmetric bilayer when GPI and PS both have saturated and long acyl chain indicating high correlation between GPI and PS whereas for all other asymmetric bilayers, the value of C_{ud} is low, suggesting the weak correlation between GPI and PS if either of them have unsaturated or short acyl chain.

5.4. Conclusion and future directions

The formation of nanoclusters of GPI-APs at the cell surface regulated by the cortical actin and myosin in the cell cortex represents a unique example of molecular complexity in nano-scale [1, 3]. This nano scale organization at the cell surface facilitates to induce functional domains responsible for signaling and sorting [6]. Lateral segregation of specific lipid/protein, serving as a platform for the sorting and signaling, is the central basis behind the idea of 'raft' [15]. The domains of the specific molecules regulated by active mechanism of the cortical actin and myosin can form at specific site on the cell surface [4, 5]. However, these specific molecules (e.g, GPI-APs) reside at the outer leaflet of the cell membrane whereas the cortical actin-myosin complexes are confined

beneath the cell membrane. Our central goal in this chapter has been to find the linkage of transbilayer coupling of the outer membrane molecular organization to the inner cell complexes. Here, we find that the transverse segregation and the strong transbilayer registry of the upper leaflet GPI lipids and inner leaflet PS lipids can occur even in the l_d phase as long as (i) significant levels of cholesterol are present in the both leaflets, (ii) upper leaflet GPI and lower leaflet PS both have saturated long chain acyl chain and (iii) PS in the lower leaflet are held (cross-linked).

This shows that the active dynamics of cortical acin-myosin complex induces aggregation of PS lipids having long saturated acyl chain in the lower leaflet which gives rise to local liquid ordered phase domains in the lower leaflet of the membrane in the presence of sufficient amount of cholesterol. These local liquid ordered phase domains in the inner leaflet induce segregation of the outer leaflet GPI-APs having saturated long acyl chain in presence of significant amount of long chain lipids (e.g., PSM) and cholesterol.

The high resolution experiments using Fluorescence Resonance Energy Transfer (FRET) [2, 4–6, 16], Near-field scanning optical microscopy (NSOM) and electron microscopy (EM) reveal that the size of nano cluster of GPI-APs is around 4-5 monomers which is dependent on the actin and myosin in cell cortex. If the nanoclusters are formed by the static actin in the cell cortex, then we might see large clusters of GPI-APs. Since the experiments [2, 4, 5] show transient and small nanoclusters of GPI-APs, this clusterization must be regulated by the dynamics of actin and myosin. This clusterization is not 'passive phase segregation' which would give large domains of GPI-APs with the size of domains following power law, well known in passive phase segregation below the critical temperature [17]. But, the earlier works [2, 4, 5] reveal that the GPI-APs, are organized as monomers and cholesterol-sensitive nanoclusters which are driven by the active nonequilibrium dynamics of the underlying actin and myosin at the cortex of the cell. In this thesis, we show that GPI-APs are

aggregated only if we crosslink PS in the lower leaflet, but not when both are unconstrained. This suggests that transient clustering of GPI-APs is controlled by dynamics of PS which is again driven by actin and myosin via binding proteins. Thus, our results provide clear evidence of GPI-AP clustering governed by dynamics of actin and myosin in the cell cortex and it is an 'active process'.

References

[1] RC Sarasij, S Mayor, and M Rao. Chirality-induced budding: a raft-mediated mechanism for endocytosis and morphology of caveolae? *Biophys J.*, 92(9):3140–58, 2007.

[2] P Sharma, R Varma, RC Sarasij, Ira, K Gousset, G Krishnamoorthy, M Rao, and S Mayor. Nanoscale organization of multiple gpi-anchored proteins in living cell membranes. *Cell*, 116(4):577–89, 2004.

[3] R Varma and S Mayor. Gpi-anchored proteins are organized in submicron domains at the cell surface. *Nature*, 394:798–3, 1998.

[4] Debanjan Goswami, Kripa Gowrishankar, Sameera Bilgrami, Subhasri Ghosh, Riya Raghupathy, Rahul Chadda, Ram Vishwakarma, Madan Rao, and Satyajit Mayor. Nanoclusters of gpi-anchored proteins are formed by cortical actin-driven activity. *Cell*, 135:1085–97, 2008.

[5] Kripa Gowrishankar, Subhasri Ghosh, Suvrajit Saha, C Rumamol, Satyajit Mayor, and Madan Rao. Active remodeling of cortical actin regulates spatiotemporal organization of cell surface molecules. *Cell*, 149:1353–67, 2012.

[6] S Mayor and M Rao. Rafts: scale-dependent, active lipid organization at the cell surface. *Traffic*, 5(4):231–40, 2004.

[7] PA Leventis and S Grinstein. The distribution and function of phosphatidylserine in cellular membranes. *Annu. Rev. Biophys.*, 39:407–27, 2010.

[8] S Garg, JX Tang, J Rühe, and CA Naumann. Actin-induced perturbation of ps lipid-cholesterol interaction: A possible mechanism of cytoskeleton-based regulation of membrane organization. *J Struct Biol.*, 168(1):11–20, 2009.

[9] X An, X Guo, H Sum, J Morrow, W Gratzer, and N Mohandas. Phosphatidylserine binding sites in erythroid spectrin: location and implications for membrane stability. *Biochemistry.*, 43(2):310–5, 2004.

[10] M Muguruma, S Nishimuta, Y Tomisaka, T Ito, and S Matsumura. Organization of the functional domains in membrane cytoskeletal protein talin. *J Biochem.*, 117(5):1036–42, 1995.

[11] R Makuch, A Zasada, K Mabuchi, K Krauze, CL Wang, and R Dabrowska. Phosphatidylserine liposomes can be tethered by caldesmon to actin filaments. *Biophys J.*, 73(3):1607–1616, 1997.

[12] Perttu S Niemelä, Samuli Ollila, Marja T Hyvnen, Mikko Karttunen, and Ilpo Vattulainen. Assessing the nature of lipid raft membranes. *PLoS Comput Biol.*, 3(2):e34, 2007.

[13] A Polley, S Vemparala, and M Rao. Atomistic simulations of a multicomponent asymmetric lipid bilayer. *J Phys Chem B.*, 116(45):13403–10, 2012.

[14] Rodrigo F. M. de Almeida, Aleksandre Fedorov, and Manuel Prieto. Sphingomyelin/phosphatidylcholine/cholesterol phase diagram: Boundaries and composition of lipid rafts. *Biophys J.*, 85(4):2406–2416, 2003.

[15] K Simons and E Ikonen. Functional rafts in cell membranes. *Nature*, 387:569–72, 1997.

[16] John F. Hancock. Lipid rafts: contentious only from simplistic standpoints. *Nature Reviews Molecular Cell Biology*, 7:456–462, 2006.

[17] A J Bray. Theory of phase-ordering kinetics. *Advances in Physics*, 43:357–459, 1994.

A

Appendix

A.1. Chemical structure of lipids

We have studied the multicomponent bilayer membrane composed of POPC, PSM, MSM and Chol in the Chapter 3 and 4. Figure A.1 shows the chemical stucture of POPC, PSM, MSM and Chol, respectively.

We have studied asymmetric bilayer composed of POPC, PSM and Chol with few GPI at the upper leaflet and PS at the lower leaflet. Figure A.2 shows the chemical structure of GPI and PS. In our simulation, we have not taken the full structure of head group of GPI (with 5 sugar groups) as shown in Figure A.2 but, we have used the simplified head structure of GPI (with 2 sugar groups). We have verified using complete structure of head group of GPI, that this modification of the structure of the head group of the GPI is reasonable for our interest on transbilayer coupling between GPI and PS as it does not affect the result.

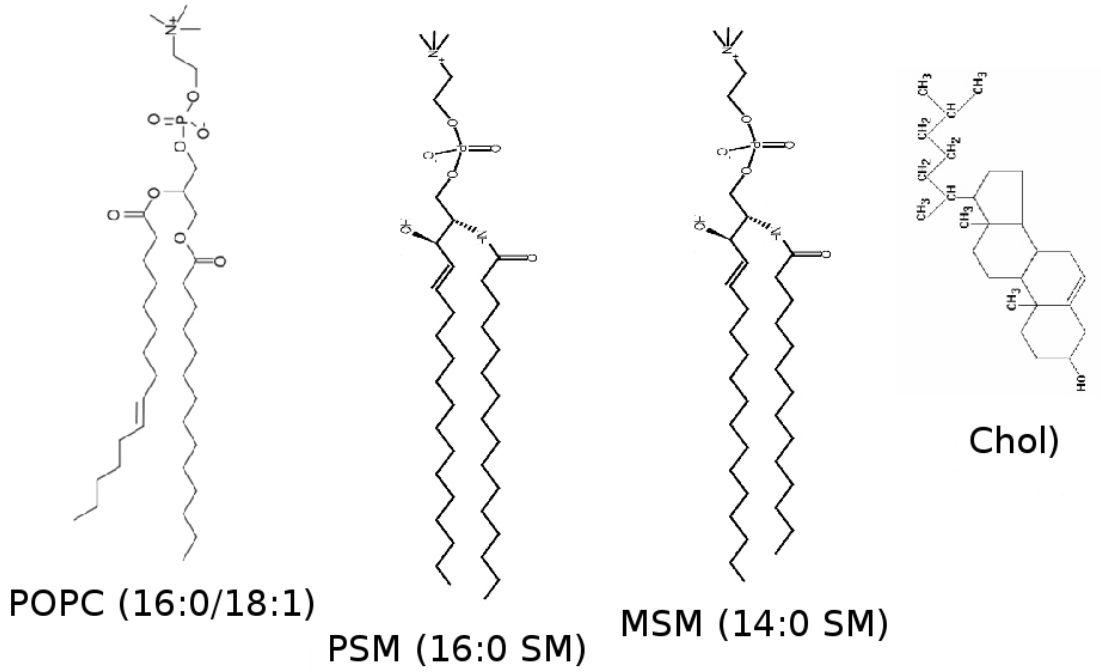

FIGURE A.1: shows chemical structure of POPC, PSM, MSM and Chol, respectively.

A.2. Area per lipid for Asymmetric bilayer membrane

We have used the time dependence of the area per lipid (Figure A.3, A.5 and A.6) to test for equilibration (≈ 20 ns) and have run the simulation for times longer than that.

A.3. Stress Profile Calculation

The lateral pressure profile,$\pi(z)$ of the bilayer membranes are shown in Figure A.11, A.13, A.14.

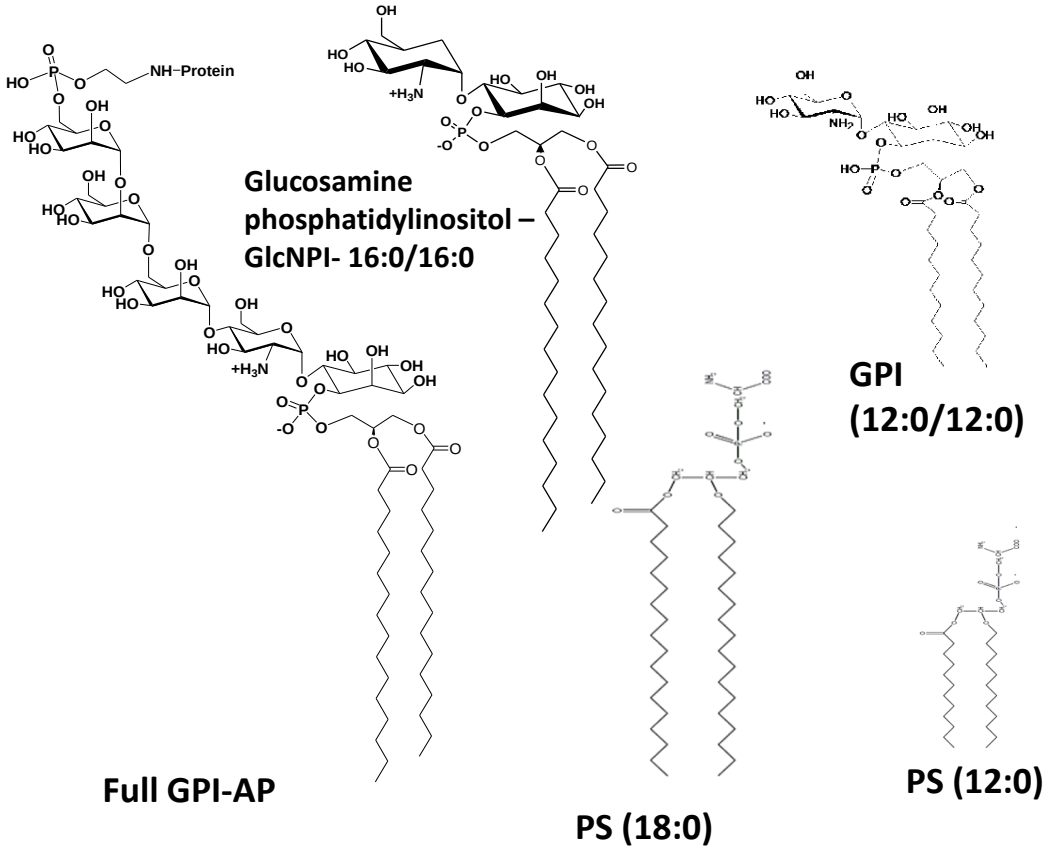

FIGURE A.2: shows chemical structure of GPI and PS, respectively.

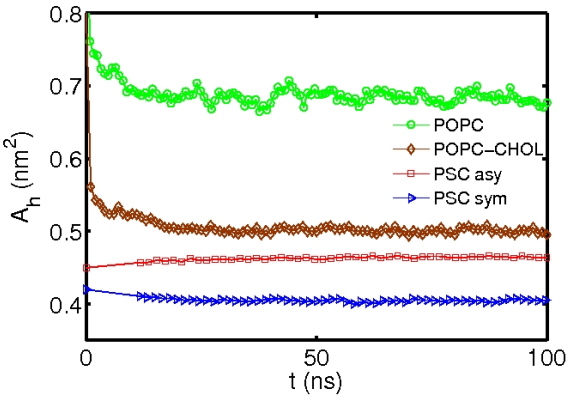

FIGURE A.3: shows the time variation of area per lipid of single (POPC), double (POPC+Chol) and ternary symmetric (POPC+PSM+CHOL with ratio $1:1:1$ in both the leaflets) and asymmetric (POPC+PSM+CHOL with the ratio $1:1:1$ in upper and POPC+Chol with ratio $1:1$ in lower the leaflet) bilayer membrane.

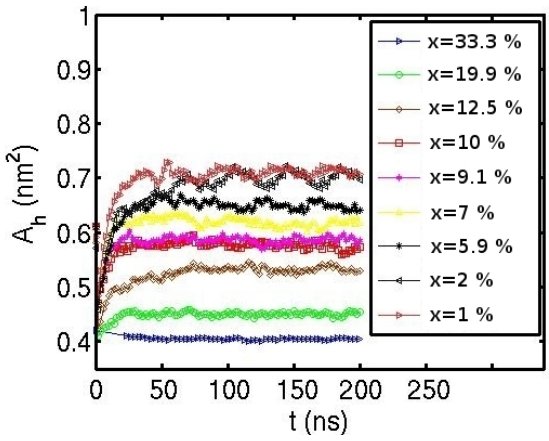

FIGURE A.4: Mean area per lipid A_h (mean calculated over all lipids in the bilayer membrane) versus time t for simulations done at different x, the concentration of PSM in both the leaflets. This shows that at times longer than ≈ 150 ns, the membrane is equilibrated.

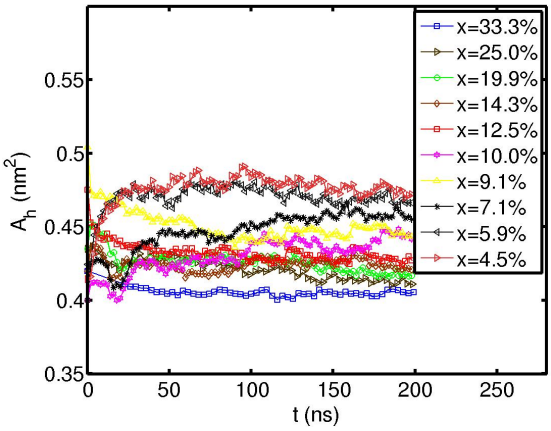

FIGURE A.5: Mean area per lipid A_h (mean calculated over all lipids in the bilayer membrane) versus time t for simulations done at different x, the concentration of PSM in the lower leaflet. This shows that at times longer than ≈ 150 ns, the membrane is equilibrated.

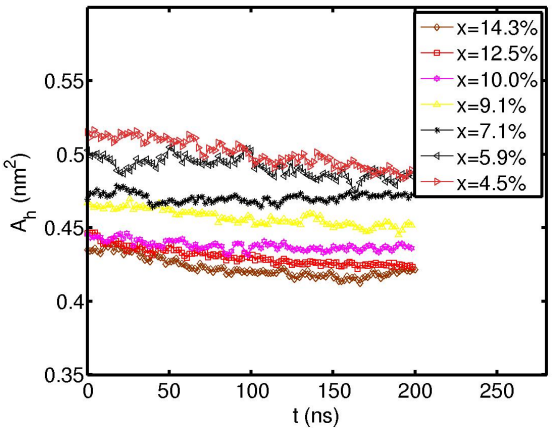

FIGURE A.6: Mean area per lipid A_h (mean calculated over all lipids in the bilayer membrane) versus time t for simulations done at different x, the concentration of MSM in the lower leaflet. This shows that at times longer than ≈ 150 ns, the membrane is equilibrated.

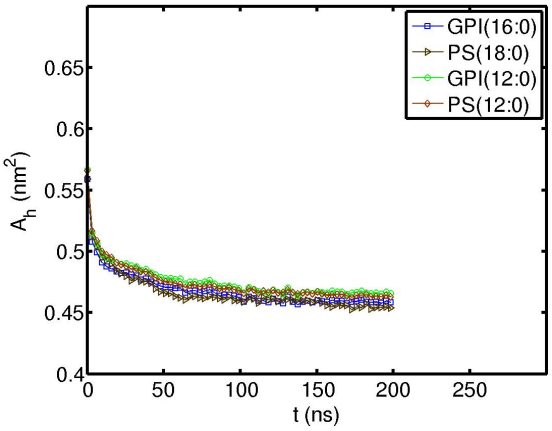

FIGURE A.7: Mean area per lipid A_h (mean calculated over all lipids in the bilayer membrane) versus time t for for symmetric bilayer composed of POPC, PSM and CHOL (33% each) with few long (short) GPI (PS). This shows that at times longer than ≈ 150 ns, the membrane is equilibrated.

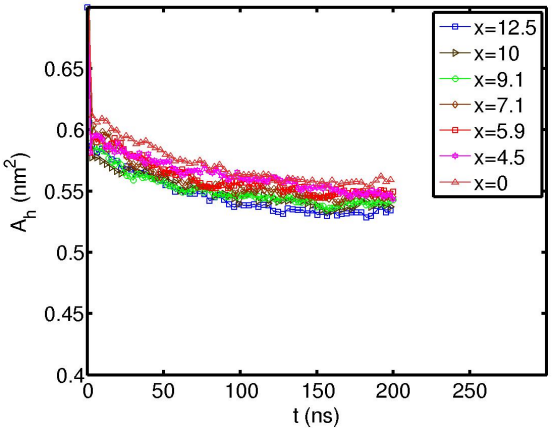

FIGURE A.8: Mean area per lipid A_h (mean calculated over all lipids in the bilayer membrane) versus time t for asymmetric bilayer of in which lower leaflet is composed of 80% of POPC and 10% of PS (Chol) whereas upper leaflet is composed of different concentration, x of PSM (Chol) and few GPI. This shows that at times longer than ≈ 150 ns, the membrane is equilibrated.

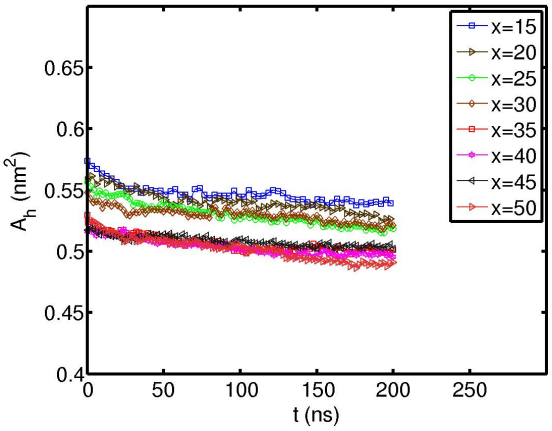

FIGURE A.9: Mean area per lipid A_h (mean calculated over all lipids in the bilayer membrane) versus time t for asymmetric bilayer of in which upper leaflet is composed of POPC and 4% of PSM (Chol) with few GPI whereas lower leaflet is composed of different concentration, x of Chol with few PS. This shows that at times longer than ≈ 150 ns, the membrane is equilibrated.

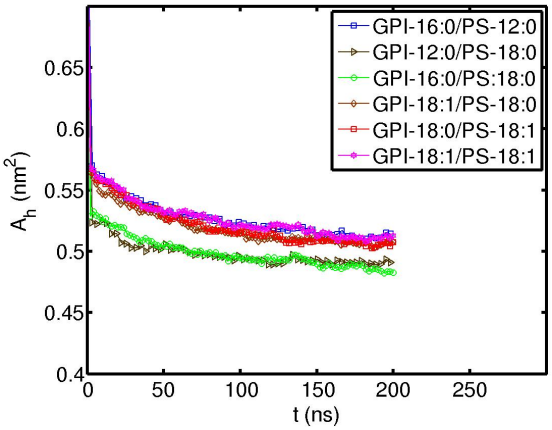

FIGURE A.10: Mean area per lipid A_h (mean calculated over all lipids in the bilayer membrane) versus time t for asymmetric bilayer of in which upper leaflet is composed of POPC and 33% of PSM (Chol) with few GPI whereas lower leaflet is composed of different concentration, 10 of PS(Chol) with different acyl structure of GPI and PS. This shows that at times longer than ≈ 150 ns, the membrane is equilibrated.

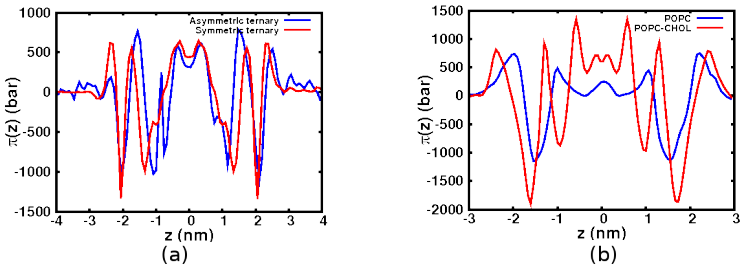

FIGURE A.11: shows the variation of Lateral pressure $\pi(z)$ profile with the normal (z-axis) to the bilayer. Figure A.11 (a) shows the lateral pressure profile for the asymmetric and symmetric ternary (POPC+PSM+Chol) bilayer membrane whereas, Figure A.11 (b) shows the lateral pressure profile for the single (POPC) and double (POPC+Chol) component bilayer membrane.

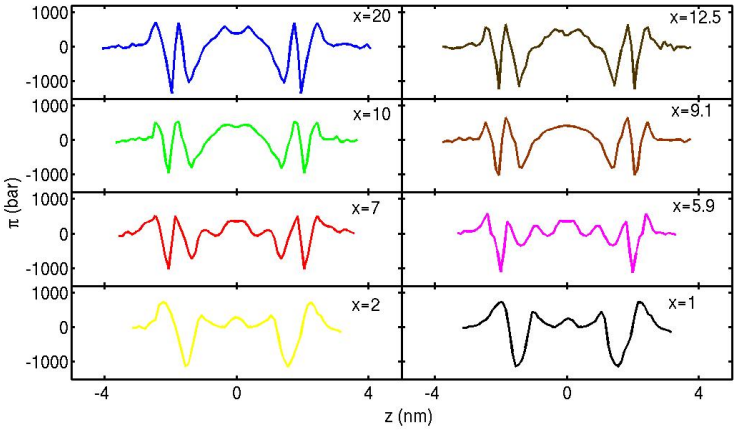

FIGURE A.12: Mean lateral pressure, $\pi(z)$ versus z, the transverse coordinate of the membrane, at equilibrium for different values of x, the concentration of PSM in both the leaflets.

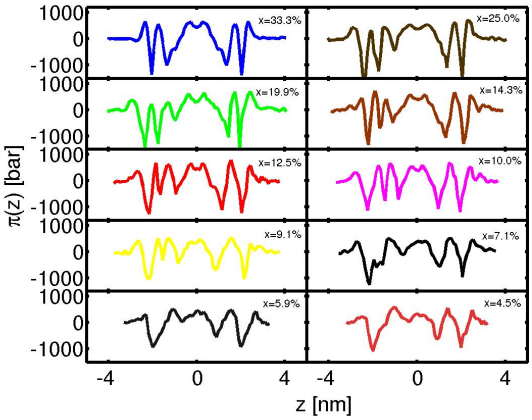

FIGURE A.13: Mean lateral pressure, $\pi(z)$ versus z, the transverse coordinate of the membrane, at equilibrium for different values of x, the concentration of PSM in the lower leaflet.

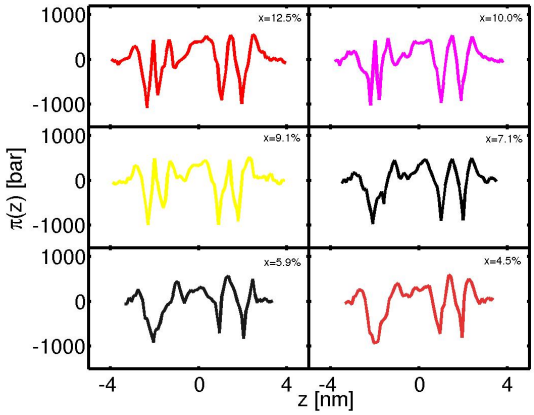

FIGURE A.14: Mean lateral pressure, $\pi(z)$ versus z, the transverse coordinate of the membrane, at equilibrium for different values of x, the concentration of MSM in the lower leaflet.

A.4. Tabulation of Force, torque and surface tension for the multicomponent bilayer membrane

We tabulate the values of the components of the force and torque asymmetric bilayer membrane (details in Chapter 3) :

Bilayer Membrane	$F_1(\,nN)$	$F_2(\,nN)$	$F_3(\,nN)$
POPC-PSM-Chol (asy)	0.29 ± 3.34	-2.56 ± 2.09	-2.16 ± 3.2
POPC-Chol	-1.01 ± 1.36	-0.32 ± 2.72	0.18 ± 0.62
POPC	0.83 ± 1.66	0.27 ± 1.14	-0.16 ± 1.25

Table A.1.: shows the values of the components of net force of the bilayer membrane. (See the time dependence of force , torque and surface tension in Figure 2.11)

Bilayer Membrane	$M_{12}(\,nN\cdot nm)$	$M_{13}(\,nN\cdot nm)$	$M_{23}(\,nN\cdot nm)$
POPC-PSM-Chol (asy)	0.77 ± 0.428	-8.83 ± 2.04	-13.303 ± 1.67
POPC-Chol	5.94 ± 0.082	8.882 ± 0.23	10.757 ± 0.42
POPC	8.26 ± 0.102	10.74 ± 0.066	9.33 ± 0.094

Table A.2.: shows the values of the components of net force of the bilayer membrane.

We tabulate the values of the components of the force and torque for the asymmetric bilayer containing PSM in the lower leaflet, for different values of its relative concentration x, (details in Chapter 4) :

x (in %)	$F_1(\,nN)$	$F_2(\,nN)$	$F_3(\,nN)$
33.3	0.663 ± 0.14	-0.839 ± 0.09	-0.196 ± 0.02
25.0	-0.334 ± 0.06	-0.476 ± 0.07	-0.282 ± 0.03
19.9	0.029 ± 0.09	-0.146 ± 0.04	-0.110 ± 0.05
14.3	-0.139 ± 0.11	0.083 ± 0.12	-0.200 ± 0.15
12.5	0.018 ± 0.01	0.141 ± 0.04	-0.301 ± 0.05
10.0	-0.123 ± 0.02	0.144 ± 0.01	-0.111 ± 0.01
9.1	-0.256 ± 0.01	0.180 ± 0.09	-0.299 ± 0.08
7.1	-0.055 ± 0.03	0.116 ± 0.04	-0.109 ± 0.01
5.9	-0.365 ± 0.01	-0.216 ± 0.02	-0.197 ± 0.05
4.5	0.298 ± 0.11	-0.371 ± 0.09	-0.136 ± 0.01

Table A.3.: Computed values of the components of the net force at different values of x, the relative concentration of PSM in the lower leaflet.

x (in %)	$M_{12}(\,nN\cdot nm)$	$M_{13}(\,nN\cdot nm)$	$M_{23}(\,nN\cdot nm)$
33.3	6.136 ± 0.128	1.102 ± 0.14	-8.153 ± 0.17
25.0	-4.396 ± 0.019	-2.927 ± 0.09	-0.001 ± 0.12
19.9	-2.220 ± 0.182	-0.687 ± 0.099	-4.246 ± 0.194
14.3	-0.224 ± 0.112	1.184 ± 0.106	5.449 ± 0.074
12.3	-1.622 ± 0.092	5.411 ± 0.091	0.086 ± 0.064
10.0	-4.260 ± 0.102	1.403 ± 0.076	0.057 ± 0.055
9.1	-10.047 ± 0.082	-0.136 ± 0.066	4.677 ± 0.081
7.1	-5.499 ± 0.099	-1.226 ± 0.064	2.449 ± 0.099
5.9	-4.214 ± 0.091	-3.042 ± 0.059	1.702 ± 0.048
4.5	6.291 ± 0.072	4.094 ± 0.086	2.383 ± 0.074

Table A.4.: Computed values of the components of the net torque at different values of x, the relative concentration of PSM in the lower leaflet.

We tabulate the values of the components of the force and torque for the asymmetric bilayer containing MSM in the lower leaflet, for different values of its relative concentration x, (details in Chapter 4) :

x (in %)	$F_1(\,nN)$	$F_2(\,nN)$	$F_3(\,nN)$
14.3	-0.237 ± 0.01	0.084 ± 0.08	-0.118 ± 0.05
12.5	-0.105 ± 0.02	-0.586 ± 0.01	-0.202 ± 0.01
10.0	0.337 ± 0.01	0.133 ± 0.05	-0.139 ± 0.03
9.1	-0.154 ± 0.02	-0.103 ± 0.01	-0.171 ± 0.01
7.1	-0.140 ± 0.01	0.072 ± 0.03	-0.216 ± 0.03
5.9	-0.147 ± 0.02	0.075 ± 0.01	-0.098 ± 0.04
4.5	0.073 ± 0.09	-0.147 ± 0.10	-0.127 ± 0.09

Table A.5.: Computed values of the components of the net force at different values of x, the relative concentration of MSM in the lower leaflet.

x (in %)	$M_{12}(\,nN\cdot\,nm)$	$M_{13}(\,nN\cdot\,nm)$	$M_{23}(\,nN\cdot\,nm)$
14.3	0.004 ± 0.012	-0.794 ± 0.126	0.551 ± 0.029
12.3	2.815 ± 0.088	1.332 ± 0.141	-0.795 ± 0.088
10.0	1.778 ± 0.092	2.729 ± 0.179	3.705 ± 0.069
9.1	-8.065 ± 0.076	-4.142 ± 0.106	-0.846 ± 0.049
7.1	-0.000 ± 0.084	4.058 ± 0.079	4.483 ± 0.097
5.9	-3.341 ± 0.034	2.889 ± 0.059	1.201 ± 0.059
4.5	-1.408 ± 0.092	-3.573 ± 0.016	-3.200 ± 0.060

Table A.6.: Computed values of the components of the net torque at different values of x, the relative concentration of MSM in the lower leaflet.

We tabulate the values of the components of the force and torque for the symmetric bilayer containing POPC/PSM/Chol with the relative concentration, $x = 33\%$ *having long (short) chain GPI(PS) in the upper (lower) leaflet, :*

	$F_1(\,nN)$	$F_2(\,nN)$	$F_3(\,nN)$
Long chain GPI	-0.647 ± 0.02	0.204 ± 0.01	0.120 ± 0.02
short chain GPI	-0.581 ± 0.02	0.465 ± 0.02	-0.291 ± 0.03
Long chain PS	0.677 ± 0.01	0.871 ± 0.01	-0.229 ± 0.02
Short chain PS	-0.701 ± 0.02	-0.463 ± 0.02	-0.801 ± 0.01

Table A.7.: Computed values of the components of the net force for the symmetric bilayer containing POPC/PSM/Chol with the relative concentration, $x = 33\%$ *having long (short) chain GPI(PS) in the upper (lower) leaflet.*

	$M_{12}(\,nN\cdot nm)$	$M_{13}(\,nN\cdot nm)$	$M_{23}(\,nN\cdot nm)$
Long chain GPI	-8.234 ± 0.01	9.184 ± 0.02	-8.178 ± 0.05
short chain GPI	-9.105 ± 0.02	10.586 ± 0.01	-9.291 ± 0.05
Long chain PS	8.337 ± 0.01	7.103 ± 0.05	-8.229 ± 0.03
Short chain PS	-7.154 ± 0.02	-8.343 ± 0.04	-9.201 ± 0.02

Table A.8.: Computed values of the components of the net torque for the symmetric bilayer containing POPC/PSM/Chol with the relative concentration, $x = 33\%$ having long (short) chain GPI(PS) in the upper (lower) leaflet.

We tabulate the values of the components of the force and torque for the asymmetric bilayer where the upper leaflet is composed of POPC, PSM and Chol with the relative concentration, $x\%$ of PSM (Chol) having long chain GPI, while lower leaflet is composed of the relative concentration, 10% of PS (Chol), with POPC contributing to the rest of the lipid content :

x (in %)	$F_1(\,nN)$	$F_2(\,nN)$	$F_3(\,nN)$
0	-0.689 ± 0.02	0.534 ± 0.02	0.429 ± 0.02
4.5	0.142 ± 0.02	-0.262 ± 0.02	-0.432 ± 0.01
5.9	0.105 ± 0.02	-0.148 ± 0.02	-0.110 ± 0.02
7.1	0.032 ± 0.02	-0.367 ± 0.02	-0.037 ± 0.01
9.1	-0.126 ± 0.02	0.404 ± 0.01	-0.346 ± 0.01
10.0	-0.249 ± 0.02	0.335 ± 0.02	-0.015 ± 0.01
12.5	-0.094 ± 0.01	-0.223 ± 0.01	-0.374 ± 0.02
33.3	0.0431 ± 0.02	-0.416 ± 0.02	-0.265 ± 0.02

Table A.9.: Computed values of the components of the net force for different values of x, the relative concentration of PSM(Chol) in the upper leaflet.

We tabulate the values of the components of the force and torque for the asymmetric bilayer where the upper leaflet is composed of POPC, PSM and Chol with the relative concentration, 4% of PSM (Chol) having long chain GPI, while lower leaflet is composed of the relative concentration, $x\%$ of Chol having few

x (in %)	$M_{12}(\,nN\cdot nm)$	$M_{13}(\,nN\cdot nm)$	$M_{23}(\,nN\cdot nm)$
0	-0.147 ± 0.02	0.245 ± 0.01	0.451 ± 0.02
4.5	-0.474 ± 0.02	7.333 ± 0.02	4.5425 ± 0.01
5.9	2.4626 ± 0.02	-0.577 ± 0.01	0.765 ± 0.02
7.1	2.191 ± 0.02	-1.976 ± 0.01	-2.753 ± 0.02
9.1	-8.628 ± 0.02	0.039 ± 0.01	5.289 ± 0.02
10.0	-8.472 ± 0.02	-4.204 ± 0.02	1.081 ± 0.02
12.5	2.668 ± 0.01	1.273 ± 0.02	-4.326 ± 0.02
33.3	6.954 ± 0.02	3.303 ± 0.02	-5.181 ± 0.02

Table A.10.: Computed values of the components of the net torque at different values of x, the relative concentration of PSM(Chol) in the upper leaflet.

long chain PS, with POPC contributing to the rest of the lipid content :

x (in %)	$F_1(\,nN)$	$F_2(\,nN)$	$F_3(\,nN)$
15	-0.166 ± 0.02	0.336 ± 0.02	-0.213 ± 0.02
20	-0.016 ± 0.02	0.254 ± 0.02	-0.240 ± 0.01
25	0.198 ± 0.02	-0.167 ± 0.02	-0.146 ± 0.02
30	0.512 ± 0.02	-0.917 ± 0.02	-0.181 ± 0.01
35	-0.949 ± 0.02	0.194 ± 0.01	-0.175 ± 0.01
40	0.101 ± 0.02	-0.075 ± 0.02	-0.049 ± 0.01
45	-0.094 ± 0.01	-0.223 ± 0.01	-0.374 ± 0.02
50	-1.961 ± 0.02	0.714 ± 0.02	-0.196 ± 0.01

Table A.11.: Computed values of the components of the net force for different values of x, the relative concentration of Chol in the lower leaflet.

We tabulate the values of the components of the force and torque for the asymmetric bilayer where the upper leaflet is composed of POPC, PSM and Chol with the relative concentration, 33.3% of PSM (Chol) having few long (short), saturated (unsaturated) GPI, while lower leaflet is composed of the relative concentration, 10% of PS(Chol) having few long (short), saturated (unsaturated) PS, with POPC contributing to the rest of the lipid content :

x (in %)	$M_{12}(\,nN \cdot nm)$	$M_{13}(\,nN \cdot nm)$	$M_{23}(\,nN \cdot nm)$
15	-0.558 ± 0.02	3.595 ± 0.02	1.357 ± 0.02
20	-0.357 ± 0.02	2.842 ± 0.02	5.267 ± 0.01
25	1.395 ± 0.02	-1.817 ± 0.02	-2.410 ± 0.02
30	1.916 ± 0.02	-2.240 ± 0.02	-1.701 ± 0.01
35	-1.180 ± 0.02	3.612 ± 0.01	-1.201 ± 0.01
40	1.554 ± 0.02	0.015 ± 0.02	0.0542 ± 0.01
45	-0.094 ± 0.01	-0.223 ± 0.01	-0.374 ± 0.02
50	1.901 ± 0.02	1.491 ± 0.02	-1.964 ± 0.01

Table A.12.: Computed values of the components of the net torque at different values of x, the relative concentration of Chol in the lower leaflet.

x (in %)	$F_1(\,nN)$	$F_2(\,nN)$	$F_3(\,nN)$
GPI-12:0/12:0 PS-18:0/18:0	-0.390 ± 0.02	-0.473 ± 0.02	-0.388 ± 0.02
GPI-16:0/16:0 PS-12:0/12:0	0.142 ± 0.02	-0.152 ± 0.02	-0.226 ± 0.02
GPI-16:0/16:0 PS-18:0/18:0	0.0431 ± 0.02	-0.416 ± 0.02	-0.265 ± 0.02
GPI-18:1/18:1 PS-18:0/18:0	0.0135 ± 0.02	-0.763 ± 0.02	0.316 ± 0.02
GPI-18:0/18:0 PS-18:1/18:1	-0.206 ± 0.02	0.114 ± 0.02	0.085 ± 0.02
GPI-18:1/18:1 PS-18:1/18:1	0.440 ± 0.02	-0.333 ± 0.02	-0.022 ± 0.02

Table A.13.: Computed values of the components of the net force for different chemical stucture of GPI/PS.

x (in %)	$M_{12}(\,nN\cdot\,nm)$	$M_{13}(\,nN\cdot\,nm)$	$M_{23}(\,nN\cdot\,nm)$
GPI-12:0/12:0 PS-18:0/18:0	4.937 ± 0.02	0.357 ± 0.02	5.907 ± 0.02
GPI-16:0/16:0 PS-12:0/12:0	4.680 ± 0.02	3.252 ± 0.02	-2.661 ± 0.02
GPI-16:0/16:0 PS-18:0/18:0	6.954 ± 0.02	3.303 ± 0.02	-5.181 ± 0.02
GPI-18:1/18:1 PS-18:0/18:0	4.726 ± 0.02	-3.490 ± 0.02	-9.463 ± 0.02
GPI-18:0/18:0 PS-18:1/18:1	1.889 ± 0.02	-1.263 ± 0.02	-1.887 ± 0.02
GPI-18:1/18:1 PS-18:1/18:1	9.212 ± 0.02	5.944 ± 0.02	-0.443 ± 0.02

Table A.14.: Computed values of the components of the net torque for different chemical stucture of GPI/PS.

The tabulated values of force and torque components shown above are comparable to the values computed for the mechanically stable single component (POPC) symmetric bilayer [24], where we found that $F_1 = 0.83 \pm 1.66$ *nN,* $F_2 = 0.27 \pm 1.14$ *nN,* $F_3 = -0.16 \pm 1.25$ *nN and* $M_{12} = 8.26 \pm 0.102$ *nN* $\cdot$ *nm,* $M_{13} = 10.74 \pm 0.066$ *nN*$\cdot$ *nm,* $M_{23} = 9.33 \pm 0.094$ *nN*$\cdot$ *nm, at equilibrium. This suggests that the model membranes under study are both force and torque balanced.*

We tabulate the values of the surface tension for the asymmetric bilayer membrane (details in Chapter 3) :

Bilayer Membrane	$\gamma(\, bar \cdot nm)$
POPC-PSM-Chol (asy)	-0.0018 ± 0.0301
POPC-Chol	0.0054 ± 0.0099
POPC	0.0204 ± 0.0357

Table A.15.: shows the values of the surface tension γ of the bilayer membrane.

We tabulate the values of the surface tension for the asymmetric bilayer containing PSM / MSM in the lower leaflet, for different values of its relative concentration x, (details in Chapter 4) :

From Figure A.13 and Figure A.14, we calculate surface tension for the asymmetric bilayer containing PSM / MSM in the lower leaflet, for different values of its relative concentration x.

x (in %)	$\gamma(\, bar \cdot nm)$
33.3	0.0324 ± 0.009
25.0	0.0466 ± 0.0089
19.9	-0.0342 ± 0.0017
14.3	0.0376 ± 0.0017
12.3	0.0169 ± 0.0101
10.0	0.0274 ± 0.0017
9.1	-0.0200 ± 0.0157
7.1	-0.0118 ± 0.0112
5.9	0.0204 ± 0.0189
4.5	0.0361 ± 0.0151

Table A.16.: Computed values of the surface tension γ at different values of x, the relative concentration of PSM in the lower leaflet.

x (in %)	$\gamma(\, bar \cdot nm)$
14.3	-0.0278 ± 0.01
12.5	0.0580 ± 0.0211
10.0	0.0132 ± 0.0019
9.1	-0.0395 ± 0.0121
7.1	-0.0504 ± 0.0292
5.9	0.0286 ± 0.0089
4.5	0.0478 ± 0.0199

Table A.17.: Computed values of the surface tension γ at different values of x, the relative concentration of MSM in the lower leaflet.

We tabulate the values the surface tension for the symmetric bilayer containing POPC/PSM/Chol with the relative concentration, $x = 33\%$ having long (short) chain GPI(PS) in the upper (lower) leaflet, :

x (in %)	$\gamma(\, bar \cdot nm)$
Long chain GPI	-0.0278 ± 0.01
short chain GPI	0.0580 ± 0.0211
Long chain PS	0.0132 ± 0.0019
Short chain PS	-0.0395 ± 0.0121

Table A.18.: Computed values of the surface tension γ for the symmetric bilayer containing POPC/PSM/Chol with the relative concentration, $x = 33\%$ having long (short) chain GPI(PS) in the upper (lower) leaflet.

We tabulate the values of the surface tension for the asymmetric bilayer where the upper leaflet is composed of POPC, PSM and Chol with the relative concentration, $x\%$ of PSM (Chol) having long chain GPI, while lower leaflet is composed of the relative concentration, 10% of PS (Chol), with POPC contributing to the rest of the lipid content :

x (in %)	$\gamma(\, bar \cdot nm)$
0	-0.0691 ± 0.01
4.5	0.1056 ± 0.01
5.9	0.0761 ± 0.01
7.1	-0.0945 ± 0.01
9.1	0.679 ± 0.01
10.0	-0.0987 ± 0.01
12.5	-0.0991 ± 0.01
33.3	0.0810 ± 0.01

Table A.19.: Computed values of the surface tension for different values of x, the relative concentration of PSM(Chol) in the upper leaflet.

We tabulate the values of the surface tension for the asymmetric bilayer where the upper leaflet is composed of POPC, PSM and Chol with the relative concentration, 4% of PSM (Chol) having long chain GPI, while lower leaflet is composed of the relative concentration, $x\%$ of Chol having few long chain PS, with POPC contributing to the rest of the lipid content :

x (in %)	$\gamma(\, bar \cdot nm)$
15	-0.0819 ± 0.01
20	0.0461 ± 0.01
25	-0.911 ± 0.01
30	-0.0679 ± 0.01
35	0.0819 ± 0.01
40	0.1080 ± 0.01
45	0.0919 ± 0.01
50	-0.0391 ± 0.01

Table A.20.: Computed values of the surface tension for different values of x, the relative concentration of Chol in the lower leaflet.

We tabulate the values of the surface tension for the asymmetric bilayer where the upper leaflet is composed of POPC, PSM and Chol with the relative concentration, 33.3% *of PSM (Chol) having few long (short), saturated (unsaturated) GPI, while lower leaflet is composed of the relative concentration,* 10% *of PS(Chol) having few long (short), saturated (unsaturated) PS, with POPC contributing to the rest of the lipid content :*

x (in %)	$\gamma(\, bar \cdot nm)$
GPI-12:0/12:0 PS-18:0/18:0	0.0324 ± 0.01
GPI-16:0/16:0 PS-12:0/12:0	0.0821 ± 0.02
GPI-16:0/16:0 PS-18:0/18:0	0.0992 ± 0.01
GPI-18:1/18:1 PS-18:0/18:0	-0.0293 ± 0.01
GPI-18:0/18:0 PS-18:1/18:1	0.0409 ± 0.01
GPI-18:1/18:1 PS-18:1/18:1	-0.0292 ± 0.01

Table A.21.: Computed values the surface tension for different chemical stucture of GPI/PS.

The tabulated values of the surface tension shown above are comparable to the values computed for the tensionless single component (POPC) symmetric bilayer [24], where we found that $\gamma = 0.0204 \pm 0.0357$ *bar· nm. This suggests that the model membranes under study are tensionless.*